DESIGN AND CHARACTERIZATION OF HIGH PERFORMANCE EXTENDED SHORT-WAVELENGTH INFRARED PHOTODETECTORS WITH BACKSIDE REFLECTOR

A THESIS SUBMITTED TO
THE GRADUATE SCHOOL OF NATURAL AND APPLIED SCIENCES
OF
MIDDLE EAST TECHNICAL UNIVERSITY

BY

MERT SATILMIŞ

IN PARTIAL FULFILLMENT OF THE REQUIREMENTS
FOR
THE DEGREE OF MASTER OF SCIENCE
IN
MICRO AND NANOTECHNOLOGY

JANUARY 2025

Approval of the thesis:

DESIGN AND CHARACTERIZATION OF HIGH PERFORMANCE EXTENDED SHORT-WAVELENGTH INFRARED PHOTODETECTORS WITH BACKSIDE REFLECTOR

submitted by **MERT SATILMIŞ** in partial fulfillment of the requirements for the degree of **Master of Science** in **Micro and Nanotechnology, Middle East Technical University** by,

Prof. Dr. Naci Emre Altun
Dean, **Graduate School of Natural and Applied Sciences** _____

Prof. Dr. Deniz Üner
Head of the Department, **Micro and Nanotechnology** _____

Prof. Dr. Alpan Bek
Supervisor, **Micro and Nanotechnology, METU** _____

Dr. Yetkin Arslan
Co-Supervisor, **Fotonika A.Ş.** _____

Examining Committee Members:

Prof. Dr. Süleyman Özçelik
Photonics, Gazi University _____

Prof. Dr. Alpan Bek
Department of Physics, METU _____

Prof. Dr. Halil Berberoğlu
Department of Physics, AHBV University _____

Assist. Prof. Dr. Yusuf Keleştemur
Metallurgical and Materials Eng., METU _____

Assist. Prof. Dr. Demet Asil Alptekin
Department of Chemistry, METU _____

Date: 07.01.2025

I hereby declare that all information in this document has been obtained and presented in accordance with academic rules and ethical conduct. I also declare that, as required by these rules and conduct, I have fully cited and referenced all material and results that are not original to this work.

Surname, Name: Satılmış, Mert

Signature :

ABSTRACT

DESIGN AND CHARACTERIZATION OF HIGH PERFORMANCE EXTENDED SHORT-WAVELENGTH INFRARED PHOTODETECTORS WITH BACKSIDE REFLECTOR

Satılmış, Mert
Master of Science, Micro and Nanotechnology
Supervisor : Prof. Dr. Alpan BEK
Co-Supervisor: Dr. Yetkin ARSLAN

January 2025, 117 pages

This thesis examines the growth, fabrication, and performance optimization of InAsP/InGaAs E-SWIR photodiodes with a 2.55 μm cut-off wavelength. It consolidates insights from books, articles, and theses, serving as a valuable reference for researchers and engineers in infrared detection. The thesis explores the principles of light and its detection mechanisms before concentrating on the development of a photodetector for the E-SWIR band.

The widely used E-SWIR detector structure is based on InGaAs absorbers due to their well-established growth techniques and ease of fabrication. Extending the wavelength range requires increasing the In mole fraction from 53% to 80%, causing up to 2% lattice mismatch with the InP substrate. This mismatch elevates G-R current and trap levels, increasing dark current and reducing detector performance. Improved fabrication techniques can mitigate these issues.

This thesis begins with the characterization of wet etching fabrication and explores methods to reduce surface-related dark current. It focuses on depositing SiN_x:H via the ICPCVD method, varying NH_3/SiH_4 ratios while maintaining constant pressure, power, and Ar gas flow. FTIR measurements reveal proportional changes in N-H, Si-H, and Si-N bond numbers with H content, showing that K^- trap center density depends

on NH_3/SiH_4 ratios. Additionally, light trapping techniques are implemented to enhance device responsivity. Front-illuminated devices are coated with backside Ti/Au reflectors, improving both responsivity and fabrication yield.

Keywords: Extended SWIR, InAsP/InGaAs, SiN_x:H, Dangling bonds, Light Trapping

ÖZ

YÜKSEK PERFORMANSLI, GENİŞLETİLMİŞ KISA DALGA UZUNLUĞUNDA KIZILÖTESİ , ARKA YÜZEY YANSITICILI FOTODEDEKTÖRLERİN TASARIMI VE KARAKTERİZASYONU

Satılmış, Mert
Yüksek Lisans, Mikro ve Nanoteknoloji
Tez Yöneticisi: Prof. Dr. Alpan BEK
Ortak Tez Yöneticisi: Dr. Yetkin ARSLAN

Ocak 2025, 117 sayfa

Bu tez, 2.55 μm kesim dalga boyuna sahip InAsP/InGaAs E-SWIR fotodiyotlarının büyütülmesi, üretimi ve performans optimizasyonunu incelemektedir. Kitaplar, makaleler ve tezlerden elde edilen bilgileri bir araya getirerek kızılötesi algılama alanında çalışan araştırmacı ve mühendisler için değerli bir kaynak sunmaktadır. Tez, öncelikle ışığın prensiplerini ve algılama mekanizmalarını ele aldıktan sonra, E-SWIR bandı için bir fotodedektör geliştirilmesine odaklanmaktadır.

Yaygın olarak kullanılan E-SWIR dedektör yapısı, iyi oturmuş büyütme teknikleri ve kolay üretilebilirlikleri nedeniyle InGaAs soğurucu malzemelerine dayanmaktadır. Dalga boyu aralığını genişletmek, In molekül fraksiyonunun %53'ten %80'e çıkarılmasını gerektirir ve bu durum InP alt tabakasıyla %2'ye kadar kafes uyumsuzluğuna yol açar. Bu uyumsuzluk, G-R akımı ve tuzak seviyelerini artırarak karanlık akımı yükseltir ve dedektör performansını düşürür. Geliştirilmiş üretim teknikleri bu sorunları hafifleterek önüne geçebilir.

Bu tez, ıslak aşındırma üretiminin karakterizasyonu ile başlayarak yüzey kaynaklı karanlık akımı azaltmaya yönelik yöntemleri araştırmaktadır. Sabit basınç, güç ve Ar gaz akışı altında, NH_3/SiH_4 oranları değiştirilerek ICPCVD yöntemiyle SiN_x:H

biriktirilmesine odaklanılmıştır. FTIR ölçümleri, H içeriği ile orantılı olarak N-H, Si-H ve Si-N bağ sayılarında değişimler olduğunu göstermiş ve K^- tuzak merkezi yoğunluğunun NH_3/SiH_4 oranlarına bağlı olduğunu ortaya koymuştur. Ayrıca, cihazın duyarlılığını artırmak için ışık hapsetme teknikleri uygulanmıştır. Ön yüzey aydınlatmalı aygıtlarla, yalnızca duyarlılığı artırmakla kalmayıp aynı zamanda üretim verimini de iyileştirmek amacıyla arka yüzeyde Ti/Au yansıtıcılarla kaplanmıştır.

Anahtar Kelimeler: Genişletilmiş SWIR, InAsP/InGaAs, SiN_x:H, Sarkan Bağlar, Işık Tuzakları

To my wife Betül and my parents

for their love and support

ACKNOWLEDGMENTS

I am deeply grateful to have worked with **Prof. Dr. Alpan Bek**, whose invaluable advice and guidance were instrumental in shaping my thesis. He welcomed me as a graduate student and consistently encouraged me to strive for excellence. His approachability and generosity with time and knowledge are unmatched. I truly appreciate all his efforts and extend my sincerest thanks to him.

I want to thank my co-advisor, **Dr. Yetkin Arslan**, for his help during the thesis period.

I would also like to express my deepest gratitude to **Dr. Fikri Oğuz** for his unwavering support. His wisdom and friendship have been invaluable, providing everything one could need in life. I am truly grateful for the opportunity to work with him and for his friendship.

I would like to thank **Prof. Dr. Süleyman Özçelik**, **Prof. Dr. Halil Berberoğlu**, **Assist. Prof. Dr. Yusuf Keleştemur** and **Assist. Prof. Dr. Demet Asil Alptekin** for their valuable comments and for being on my thesis committee.

I would also like to thank my fellow lab mates, **M.Sc. İrfan Alp Gezgin**, **M.Sc. Çağrı Tok**, and **Habibe Keleş**, for their constant support and guidance. They were always there to offer advice and valuable suggestions throughout my thesis.

Last but certainly not least, I would like to thank my beloved wife **M.Sc. Betül Satılmış**, for being the source of my happiness. Additionally, I would like to thank my parents **Hanif Satılmış**, **Hülya Satılmış** and **Serenay Satılmış**. Their unwavering care and support have been the cornerstone of every decision I've made.

Table of Contents

LIST OF TABLES

TABLES

LIST OF FIGURES

FIGURES

CHAPTER 1

INTRODUCTION

1.1 A Brief History of the Development of the Infrared Region

One of the most interesting subjects that humanity has been studying for centuries and continues to study is light. Many great minds (Plato, Descartes, Newton, Huygens, Young, Maxwell) have put quite forward-looking theories about light. Plato (428-328 BC) interpreted the definition of light as the "sensation of rays reflected to our eyes from everything observed." In 1957, the International Commission on Illumination (The CIE) defined light in the International Lighting Vocabulary (ILV) publication as "characteristic of all sensations and perceptions that is specific to vision [1].

The rapid progress in the infrared (IR) region over the past 30 years actually began with the foundations laid by a pharmacist and chemist named Carl Wilhelm Scheele (1742-1786). The continuation came with the steps taken by Sir Frederick William Herschel (1738-1822) in February 1800. In Herschel's work, he passed sunlight through a prism to separate it into colors and then measured the heat created by each color using a thermometer placed in front of each color. Through his work, which he referred to as heat rays, he noticed that the temperature increased as he moved from violet to red. Continuing his studies, he observed that, just like in the visible region, light in the infrared region (the prefix infra means below) is also reflected, refracted, absorbed, and transmitted [2].

To understand the properties of light and the effects it creates, we had to wait until 1845 after Plato. The interaction of light with electromagnetic waves was first observed by Michael Faraday. James Clerk Maxwell then analytically proved in 1864, in his book "Dynamical Theory of the Electromagnetic Field," that electromagnetic waves move at the speed of light in empty space. Although Maxwell's book was widely

accepted in the academic world, it had not yet been experimentally proven. At this point, in the fall of 1886, experiments conducted by Heinrich Hertz with the Leyden Jar experiment experimentally confirmed Maxwell's ideas. In the following years, physicists known as the "Maxwell quartet" (George Francis FitzGerald (1851-1901), Oliver Lodge (1854-1940), Oliver Heaviside (1850-1925), and Heinrich Hertz (1857-1894)) explained the relationship between electromagnetic waves and light both analytically and experimentally.

The discovery of the infrared region and the subsequent discovery of thermography (a noncontact procedure to detect infrared range electromagnetic radiation and turn it into an image) cannot be linearly explained around a single milestone. However, the data obtained from each of these events has made the next data more valuable. Below are some of the scientists who have contributed to the current state of infrared detection technology through their work in this field:

- **Thomas Johann Seebeck (1770-1831):** He investigated the connection between temperature and electricity and discovered the thermoelectric effect (Seebeck Effect). By heating two different metals at the soldered joints point within a closed circuit and studying the deviation in a magnetic compass caused by it, he revealed the thermoelectric effect.
- **Leopoldo Nobili (1784-1835) and Macedonio Melloni (1798-1854):** Nobili and Melloni collaborated to discover a thermoelectric battery.
- **Jean Charles Peltier (1785-1845):** They discovered that when a voltage difference is created across two different metal wires connected in series, a temperature increase occurs at the junction depending on the direction of the current flow.
- **Andre-Marie Ampere (1775-1836):** In 1835, he postulated that light and electromagnetic radiation share the same properties.
- **Samuel Pierpont Langley (1834-1906):** As a result of his studies, in 1878, he invented the bolometer, which had a very high sensitivity to temperature differences, using a system consisting of two thin metal strips, a Wheatstone

bridge, a galvanometer, and a battery. With this invention, he was able to measure the intensity of solar radiation from the sun at different wavelengths.

- **Josef Stefan (1835-1893), Ludwig Boltzmann (1844-1906):** Gustav Kirchhoff's theoretical analysis, combined with an empirical deduction by Josef Stefan relating to T^4, led to the Stefan-Boltzmann law. Boltzmann further derived the radiation pressure concept thermodynamically from Stefan's law.
- **Wilhelm Wien (1864–1928):** He discovered Wien's displacement law, which made it possible to calculate the emission of a blackbody at any reference temperature.

In 1913, the studies conducted in the infrared region were used for the first time for a discovery purpose. The inventor, Leonhard Bellingham, found an idea for determining the location of objects buried under glaciers using infrared waves as illustrated Figure 1.1 [3]. This situation opens the way for infrared technology to become a crucial technology during World War I (for communication, distance detection, and guiding flying objects).

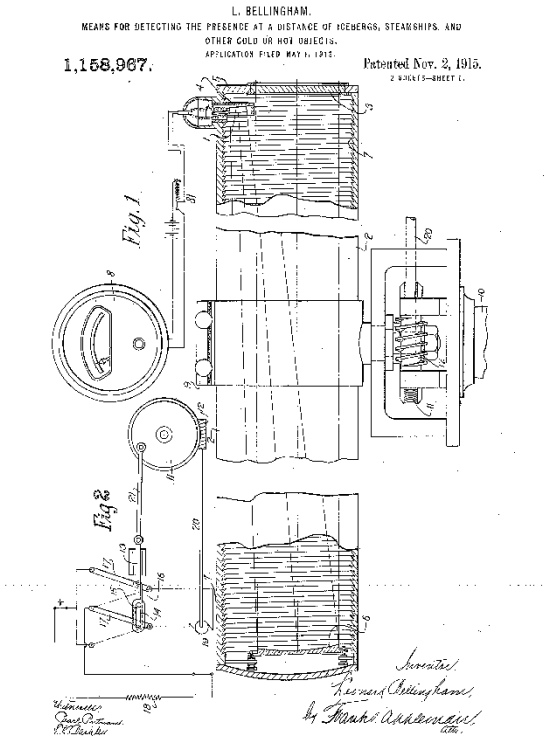

Figure 1.1. The patent illustration of the infrared device designed by Leonard Bellingham for detecting objects buried under glaciers.

The interest in the infrared region, which began with World War I, continued to increase in the following years, opening up various applications for different wavelength ranges.

However, the pioneer worked for the development of infrared detectors was established in the time of World War II. Selenium based photoconductive applications was already recognized at 1900s, on the other hand light induced materials was living in at the blind spot. Dedicative studies to classify the photo sensitive materials in infrared region is start at 1920s by T.W. Case [4], [5]. After that infrared detector materials were discovered one by one which they were PbS, PbTe and HgCdTe in lates 1950s.

Today the primary approach for infrared detectors is the detection of each region with one detector where all materials stacked together. However, there are some drawbacks that need to be addressed such as effective radiation absorbance and also electron interaction with radiation in material. Thereby, further investigation is needed to extend the selective wavelength range with optimized fabrications to increase the absorption of radiation.

1.2 Scope of Thesis

Technological progress in every field of science creates urgent needs, pushing the limits for the application of the infrared region. The ability to detect electromagnetic radiation in harsh weather conditions, night vision, target acquisition, VOC gas sensing, space exploration, and medical applications, making infrared detectors worth mentioning in daily life [4], [6], [7]. Basically, to overcome each application's unique problem the infrared region was customized to find an answer. Thereby, the spectrum is divided into sub-regions according to different infrared medium applications, and as listed below:

- Near Infrared Region (NIR - 0.7 μm – 1.1 μm),
- Short Wave Infrared Region (SWIR - 1.1 μm – 2.0 μm),
- Extended Short Wave Infrared Region (e-SWIR 1.0 μm - 3.0 μm)
- Mid-Wave Infrared Region (MWIR - 3.0 μm – 8.0 μm),
- Long Wave Infrared Region (LWIR - 8.0 μm – 12 μm),
- Very-Long Wave Infrared Region (VLIR - 12 μm – 20 μm),
- Far Infrared Region (FIR - 20 μm – 1000 μm).

Specifically, semiconductors are only materials for the infrared region because of their natural properties such as electrical conductivity, tunable band gap, sensitivity to this region. Their electrical conductivity is intermediate between metals and insulators. It is significant that the conductivity of these materials can be shifted according to growth techniques and environmental changes such as temperature and optical excitation.

These properties make semiconductor materials superior elements for the infrared region. Additionally, the increased knowledge in semiconductor materials and growth techniques has led to the rapid development of infrared regions over the last half-century. Manufacturing methods to growth the III-V semiconductor materials began with Czochralski technique and have advanced to produce monolayer controllable devices such as Metal Organic Chemical Vapour deposition (MOCVD) and Molecular Beam Epitaxy (MBE). These developments in device technology have dragged us towards the growth of high-quality lattice-matched epitaxy structures. As a result, detection of each infrared region with specified materials has become possible.

Furthermore, one of the bands in the infrared region has been subdivided into narrower band through extensive studies to fulfill various applications. The detection of long-range electromagnetic radiation and absorption lines over the 1.7 μm SWIR region is extended to the 3 μm which this region called as e-SWIR region. However, to highly fabricate photo sensitive detectors that work in this region needs alignment of several novel process design and characterization techniques. In this thesis, it is aimed to fabricate and characterize a high-performance e-SWIR photodetector, by using mesa designs. To achieve higher performance values with e-SWIR photodetectors, the first step involves characterizing the passivation. Passivation is one of the factors that can contribute to an increase in leakage current in detector structures. Therefore, the passivation of InAsP material is investigated and optimized using several different recipes with an ICPCVD device, along with FTIR measurements.

Subsequently, the thesis focuses on increasing photon detection and enhancing the responsivity of the detector. To achieve this goal, several different methods are employed and compared, including backside thinning, designing a backside reflector with dielectric materials, implementing a backside reflector with a thin metallic film layer, and hybridizing InGaAs-based e-SWIR detectors with a silicon black silicon surface.

Chapter 1 provides an overview of the history of the infrared region, tracing its evolution from the early stages to our current situation. Chapter 2 delves into the

fundamentals of photon detection, covering parameters such as reflectance, transmission, and absorption, along with relevant formulas. It explores the concept of photon detection for semiconductor materials, elucidating how photons affect detector structures from PN junctions to blackbody radiation. Additionally, the chapter discusses blackbody radiation and introduces figures of merit pertinent to the detector subject. It investigates the influence of dark current and dark current modeling parameters, including generation-recombination current, diffusion current, tunneling current, surface leakage, and quantum efficiency. The chapter concludes by highlighting the significance of E-SWIR technology for photon detection and explaining its pros and cons.

In Chapter 3, a summary of the experimental procedures used in the thesis fabrication steps is provided, along with the reasons behind each step's execution. It explains why and how each step is carried out, from material selection to the importance of dry and wet etching, and passivation to e-SWIR device architecture.

Chapter 4 presents detailed fabrication steps, starting with epi-layer properties that provide information about the device epi-layer growth parameters. Each layer is then explained in detail, along with the layout design used in fabrication for each step.

Chapter 5 delves into the characterization of fabrication and the effects of each experiment. It begins by exploring mesa etch trials and the impact of wet etching and dry etching experiments on reliability. Subsequently, it delves into passivation fabrication, which aims to reduce dark current related to surface issues. Following that, it focuses on enhancing the response to incoming light through the design of a backside reflector, incorporating grinding and lapping applications.

The final chapter explains the significance of increasing photodetector performance through various fabrication techniques.

CHAPTER 2

THEORITICAL BASIS

2.1 Process of the Photon Detection

In general, infrared detectors are devices for transforming incoming light that is sensitive to wavelength into electrical signals. Controlling the transformation of light into measurable physical quantities requires consideration of light and matter interaction [8]. An infrared radiation falls to the material three major physics phenomena has occurred: reflection, transmission and absorption of the incoming radiation. While it's not feasible to delve into every detail of electromagnetic waves and properties in this thesis, it's necessary to introduce some key concepts for clarification. Electromagnetic radiation when passes through from a medium and interacts with the second medium, part of the radiation is *reflected* at the interface and the rest passes into the third medium. Whole light can be *absorbed* or part of it absorbed, any light that is not absorbed in the third medium is referred to as *transmitted* radiation [9]. Absorption of photon energy by the materials causes the excitation of electrons from occupied low-energy state to the higher-energy state. The valance band so called fully occupied state and electrons in valance band tend to largely unoccupied states in the conduction band. Absorption specifically happens when the energy of the incoming photons higher the forbidden band gap (E_g) of the material.

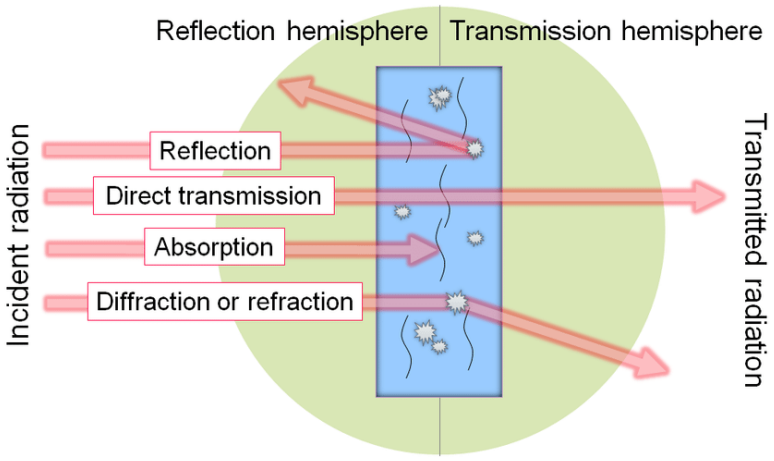

Figure 2.1. The interaction of light involves various phenomena, including transmission, absorption, reflection, and scattering

According to that the ratio of the light that reflected (Θ_R) from the second medium to the incident photon flux (Θ_I) defined as a *reflection* (R):

$$\mathrm{R} = \frac{\Theta_R}{\Theta_I} \tag{2.1}$$

The *absorption* (A) is absorbed flux (Θ_A) divided by incident photon flux (Θ_I) given as:

$$\mathrm{A} = \frac{\Theta_A}{\Theta_I} \tag{2.2}$$

The *transmission* (T) is the ratio of transmitted flux (Θ_T) to the incident photon flux (Θ_I) and given as:

$$\mathrm{T} = \frac{\Theta_T}{\Theta_I} \tag{2.3}$$

The total of the reflection, absorption and transmission are together equal to incident flux and with that:

$$A = \Theta_I - R - T \tag{2.4}$$

The materials that are sensitive to incoming photon wavelength are the important parameters, however, before coming to that point losses need to be considered. Optical

losses occur even in ideal detector because of the surface [10]. Surface is and dangling bonds are defect points in detector structures and a lot of research is still going on to reduce the effect [11]. Absorption material has unique index of refraction which is complex expression and given as $n_a = n - ik$, where k is defined as an extinction coefficient. The Figure 2.2 shows the function of the photon energy versus refractive index n for InGaAs material. Thicker semiconductor materials have higher refractive index values which are approximately higher than 3 and colors tend to be gray [12].

$$n_a = \frac{(n-1)^2 + k^2}{(n+1)^2 + k^2} \tag{2.5}$$

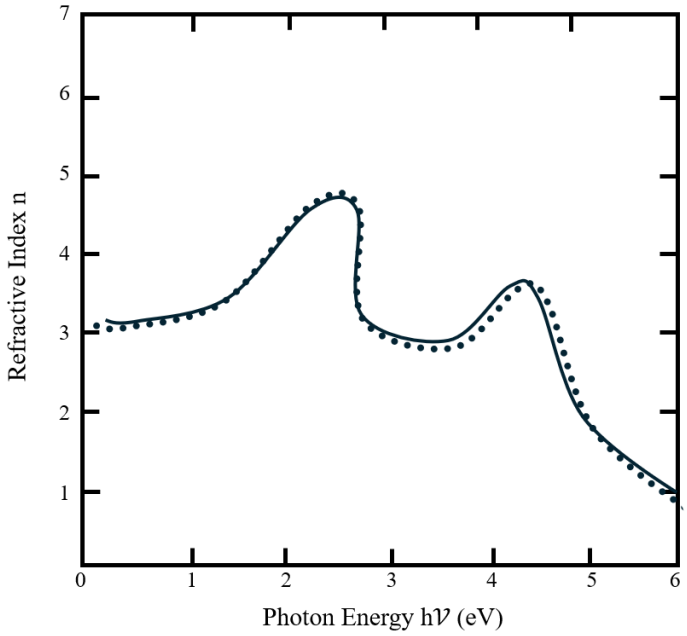

Figure 2.2. Real part of the refractive index for InGaAs

The index of refraction includes the imaginary part of the extinction coefficient, which is zero for undoped semiconductor materials. According to the equation (2.1) the reflection coefficient depends on refractive index of material (n_s) wavelength can be described as below.

$$R(\lambda) = \left(\frac{n_{air} - n_s(\lambda)}{n_{air} - n_s(\lambda)}\right)^2 \tag{2.6}$$

For any semiconductor materials that have the refractive index above $n_s > 3$ the photons are reflected over 30%. This is for sure one of the optical losses that needs to be considered.

One of the oldest problems in infrared detectors (IR detectors) is reflection and decreasing the reflection from the surface. Preventing reflection can be done with several ways such as antireflection coatings (AR) or custom lenses. However, the easiest way to do this is with AR coatings for specific applications. The purpose is to use destructive interference or diffraction to maximize the amount of flux penetrating to material [12]. IR detectors that work in lower energy photons spectral range is crucial because materials used for IR region as mentioned above have higher real part of refractive index (typically over 3).

These coatings operate on the principle of interference of waves. According to this principle the thickness and refractive index of the antireflection film are determined as follows:

$$t_{film} = \frac{\lambda}{4n_{film}} \tag{2.7}$$

The key point is that the electromagnetic wave reflected from the top of the film will be 180^o out of phase and allowing it to pass through the inside of the film.

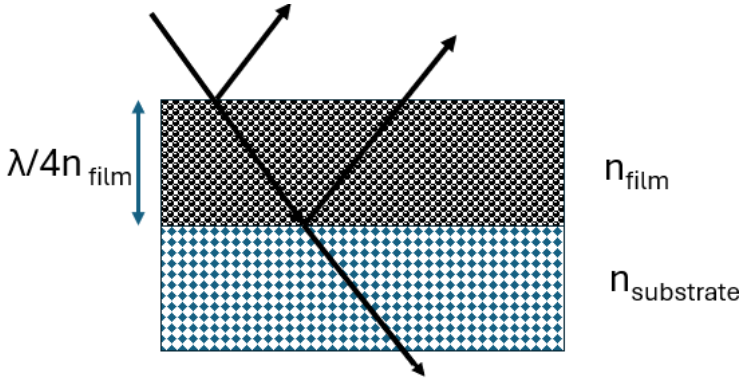

Figure 2.3. One layer of antireflection over surface

For single-layer antireflection film, the condition of reflection minimum can be calculated as follows:

$$n = \sqrt{n_a . n_s} \tag{2.8}$$

Where n is homogeneous single-layer AR film refractive index. Multilayer structures have better performance outcomes than single layer structures. Single layer structures generally offer a narrow spectral range of low reflection. However, with stack structure the spectral range can extend further wavelengths which reduces the detection limitation.

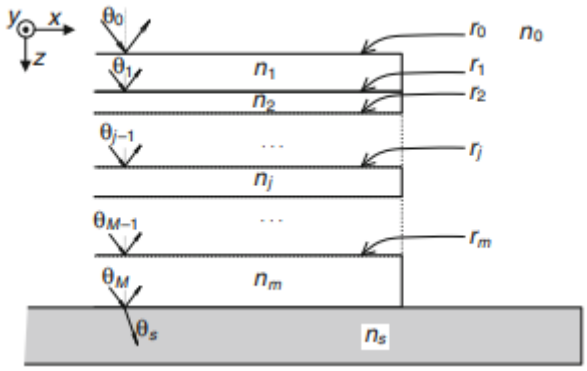

Figure 2.4. Multilayer stack formation AR coating on material surface

As can be seen Figure 2.4 the for constant refractive index for each j-th layer thickness can vary. For calculation of j-th layer Fresnel equation is used and below Equation (2.9) is determined.

$$d_j = \frac{d}{\sum_{\substack{k=0 \\ j \neq k}}^{m} (\frac{n_j}{n_k} + 1)} \tag{2.9}$$

The part of the photon flux that has not been reflected attenuated depending on the length of the optical path of light, which has been passed through the material.

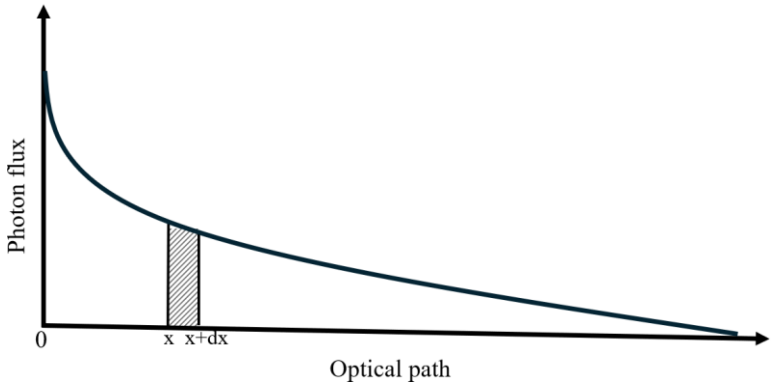

Figure 2.5. Absorption of photons depending on the thickness of material

$$\Theta_I = \Theta_I(x_0) e^{-\alpha(x-x_0)} \tag{2.10}$$

Where α is a function of wavelength and is known as the absorption coefficient. The longer wavelength light difficult to absorb as can be understood from the Equation (2.10). The absorption unlike the opaque metals, semiconductors display unique behavior.

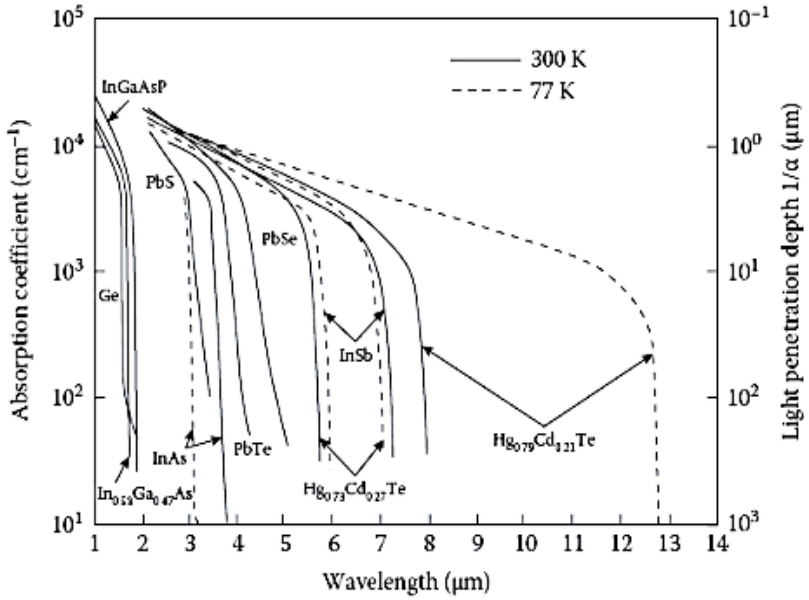

Figure 2.6. Absorption coefficients for various semiconductor materials vs. wavelength

As can be seen from Figure 2.6 the absorption coefficient of the $In_{0.53}Ga_{0.47}As$ start from the 1.7 μm and shows direct bandgap behavior [10]. The penetration depth is decreases with increasing the absorption coefficient which is the photons are quickly absorbed despite the longer wavelength of 1.7 μm.

In general lattice absorption refers to the annihilation or absorption of photons which is excitation of electron out of the valance band into the conduction band and leaving a hole in the valence band. Incoming photon energy is quite higher despite the crystal momentum and the initial and final state of energy of the crystal given below.

$$E_f - E_i = hf \tag{2.11}$$

The absorption transition for direct-bandgap in semiconductors is shown as the energy-momentum graph in Figure 2.7.

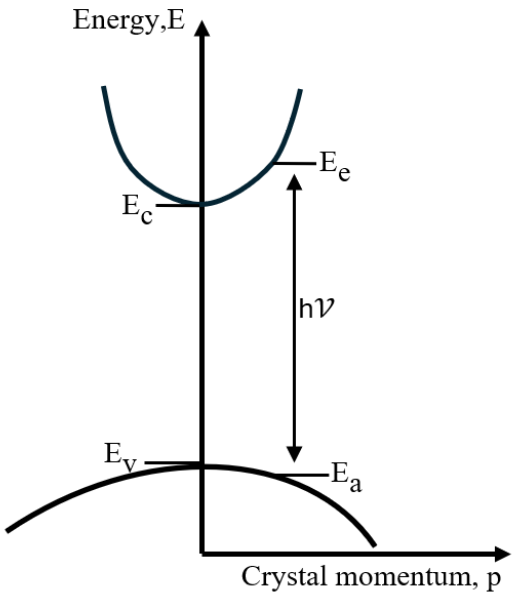

Figure 2.7. Crystal momentum-energy graph of direct-bandgap semiconductor

According to given Equation (2.11) energy of the charge carrier is defined as:

$$E_f - E_C = \frac{p^2}{2m_e^*} \qquad E_i - E_v = \frac{p^2}{2m_h^*} \tag{2.12}$$

If we consider Equation (2.11) and (2.12) into account

$$hv - E_g = \frac{p^2}{2}\left(\frac{1}{m_e^*} + \frac{1}{m_h^*}\right) \tag{2.13}$$

It can be seen from the Equation (2.11) that the energy of the photon increases in parallel with the crystal momentum increases. This process is dependent on the density of electrons and holes. According to that, if we increase the photon energy clearly the absorption probability increases which means that higher energy photons have higher chance of being absorbed. Regarding explanations the theoretical treatment gives the numerical approximation:

$$\alpha(hf) \approx C\,(hf - E_g)^{1/2} \tag{2.14}$$

Where C is numerical constant $2x10^4$ for direct bandgap semiconductors.

Additionally, there is a second type of transition in semiconductors, the latter absorption of photon which is an indirect bandgap transition. In this situation valance band maximum point and conduction band minimum point lie at different crystal momentum. Absorption of photon to generate electron-hole pair need also momentum.

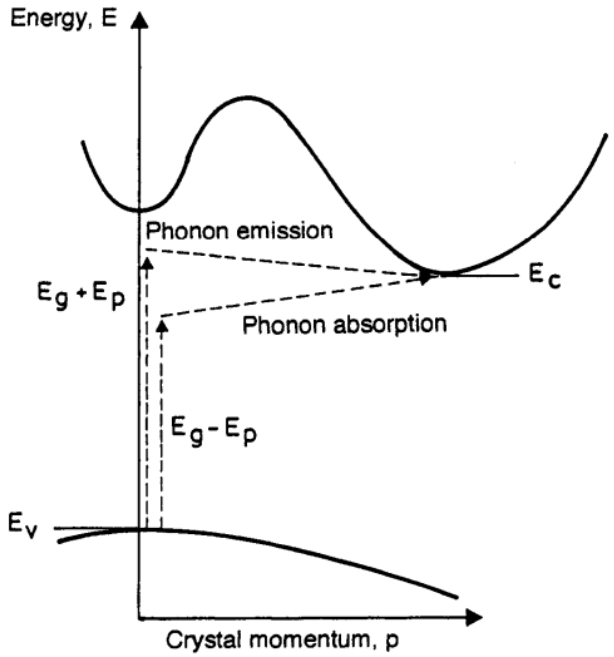

Figure 2.8. conduction band energy transition in indirect bandgap

As indicated in Figure 2.8 the absorption involves two different particle energy one of its band gap energies and the other one is phonon. Phonons are lattice source particles and generated by vibration of a lattice. Generally, photon energy higher than bandgap generates electron-hole pair and this electron jumps over the minimum position of conduction band and quickly returns to the lower energy level. This return creates thermal energy or phonon in crystal and this phonon energy helps the electron pass through the conduction band. Because this absorption process requires one more extra particle "phonons" be involved, the probability of photon being absorbed is much

lesser than direct bandgap formation. The theoretical analysis of the absorption coefficient gives the results.

$$\alpha_a\,(hf) = \frac{C\,(hf - E_g + E_p)^2}{\exp\left(\frac{E_p}{kT}\right) - 1} \tag{2.15}$$

For transition of phonon absorption given as,

$$\alpha_e\,(hf) = \frac{C\,(hf - E_g - E_p)^2}{1 - \exp\left(\frac{E_p}{kT}\right)} \tag{2.16}$$

After that absorption coefficient can be given as,

$$\alpha(hf) = \alpha_e\,(hf) + \alpha_a\,(hf) \tag{2.17}$$

Absorption probability for gets higher if the photon energy $hf > E_g + E_p$.

2.2 P-N Junction

The definition of the p-n junction in semiconductor and understanding how junction operates begin with considering the properties of p- and n- type material. N-type materials have electrons as the majority carriers, on the other side p-type materials have holes as majority carriers. The affinity of electron represents as a e_χ and defined as the following:

$$e_\chi = E_v - E_c \tag{2.18}$$

Where E_v is energy of vacuum level and E_c is minimum energy point of conduction level. The work function is also presented in Figure 2.9(a). Work function is described as follows:

$$\begin{aligned} \Phi_{sp} &= E_v - E_{Fp} \\ \Phi_{sn} &= E_v - E_{Fn} \end{aligned} \tag{2.19}$$

Where Φ_{sp} and Φ_{sn} are work function of p-type material and n-type material. Additionally, E_{Fp} and E_{Fn} are fermi level of p-type material and n-type material. Negatively charged acceptors in the p-region and positively charged donors in n-region are left behind by a field that sweeps the mobile carriers through a depletion region where the band is bent. In the p- region, the depletion region stretches to distance W_p for p region and distance for n region is W_n.

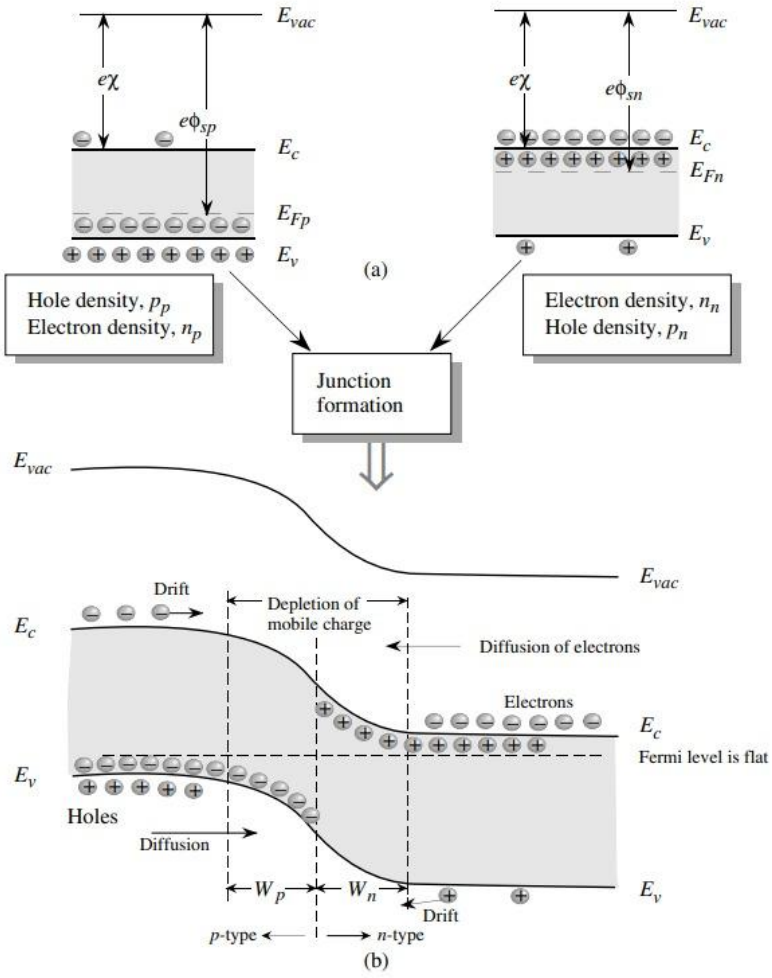

Figure 2.9. (a) p and n type material structure before junction formation (b) Unbiased junction schematic of band profile in p-n junction

Electrons and holes that enter the depletion region are diffused to opposite sites due to electrical field. However, the counter-field drift current works to established

equilibrium. When no bias is applied these currents are cancel each other (see Figure 2.10).

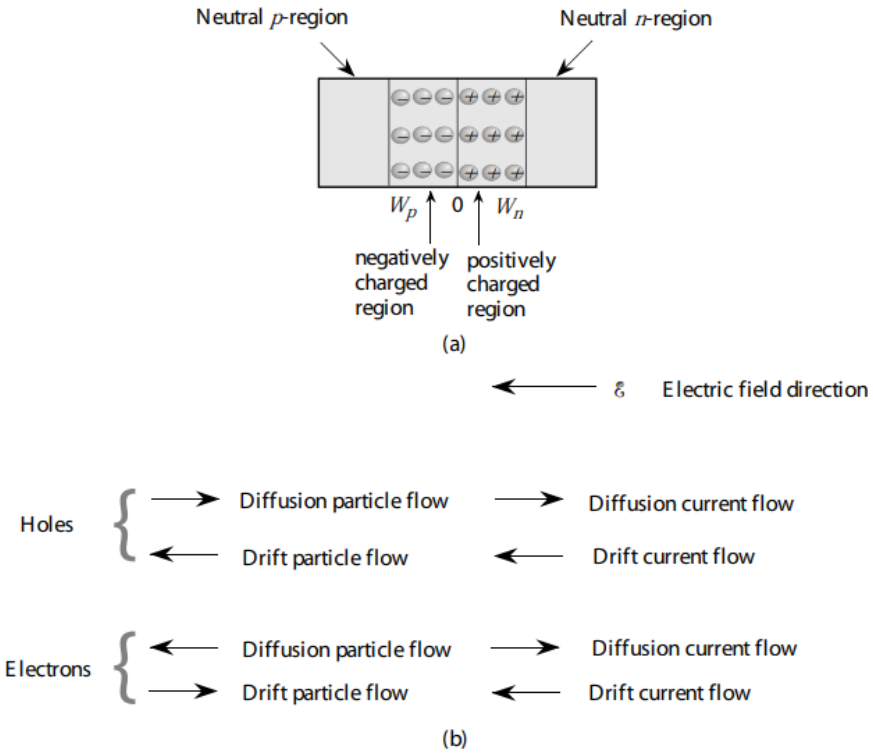

Figure 2.10. No biased situation in depletion region and showing the various current and particle flow components

When pn structure brings together free electron from n-side and free holes from p-side, they are recombined. The depletion region contains fixed charges as donor and acceptor ions. Due to these fixed charges in the depletion region, a potential is generated, known as built-in potential.

$$\frac{\mu_p}{D_p} = \frac{e}{K_B T} \tag{2.20}$$

$$eV_{bi} = E_g - (E_c - E_F)_n - (E_F - E_v)_p \tag{2.21}$$

$$(E_c - E_F)_n = -K_B T ln(\frac{n_{n0}}{N_c}) \tag{2.22}$$

Where μ_p is mobility of holes and D_p is diffusion coefficients of hole, n_{n0} is the electron density on the n-side of the device. Let's assume that all of the donors are ionized,

$$n_{n0} = N_d \tag{2.23}$$

Similar to Equation (2.22) it can be written for p_{p0} the density of holes on the p-side of the device.

$$(E_F - E_v)_p = -K_B T ln(\frac{p_{p0}}{N_v}) \tag{2.24}$$

$$p_{p0} = N_a \tag{2.25}$$

This equation series calculates the potential generated in depletion region:

$$eV_{bi} = E_g + K_B T ln(\frac{p_{p0} n_{n0}}{N_v N_c}) \tag{2.26}$$

From the relation of intrinsic carrier density

$$n_i^2 = N_v N_c \exp(-\frac{E_g}{K_B T}) \tag{2.27}$$

$$V_{bi} = \frac{K_B T}{e} \ln(\frac{p_{p0} n_{n0}}{n_i^2}) \tag{2.28}$$

Now we can estimate the built-in potential in no biased condition and from that we can calculate the density of holes and electron either side of p or n.

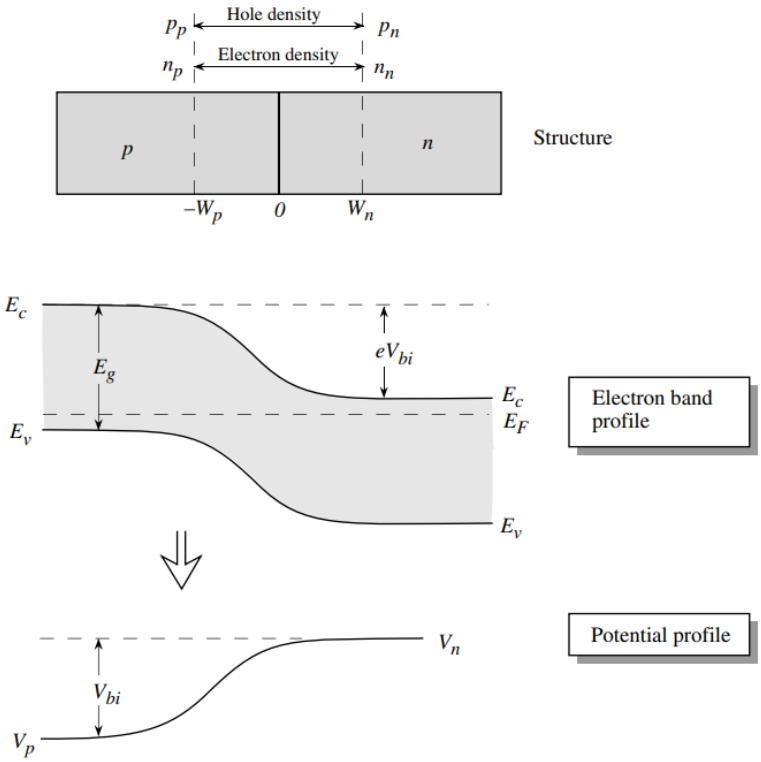

Figure 2.11. P-N junction structure and the electron band and potential profile are given under no bias conditions

As discussed above, the concentration of electron and width, as well as the concentration of holes and width, need to be equal to each other. The calculation of the width of the depletion region also can be calculated.

$$AW_pN_a = AW_nN_d \tag{2.29}$$

Where A is the cross-section of the p-n structure is given in Figure 2.11. Approximation of Poisson equation in the various areas of the depletion region.

$$W_p(V_{bi}) = \left\{\frac{2\varepsilon V_{bi}}{e}\left[\frac{N_d}{N_a(N_a+N_d)}\right]\right\}^{1/2} \tag{2.30}$$

$$W_n(V_{bi}) = \left\{\frac{2\varepsilon V_{bi}}{e}\left[\frac{N_a}{N_d(N_a+N_d)}\right]\right\}^{1/2} \tag{2.31}$$

$$W(V_{bi}) = \left[\frac{2\varepsilon V_{bi}}{e}\left(\frac{N_a + N_d}{N_a N_d}\right]^{1/2}\right. \tag{2.32}$$

According to the expressions given above, it can be stretched to find the electric field, potential, and as we mentioned depletion region width. Extended version for the electric field as follows:

$$\varepsilon_m = -\frac{eN_d W_n}{\varepsilon} = -\frac{eN_a W_p}{\varepsilon} \tag{2.33}$$

Negative signs represent the negative x-axis. As can be understood from the Figure 2.12 electric field reach peak point when $x = 0$ and field is not uniform.

Depletion region thickness can be estimated as follows:

$$W = \sqrt{\frac{2\varepsilon(N_a + N_d)(V_{bi} - V_R)}{eN_d N_a}} \tag{2.34}$$

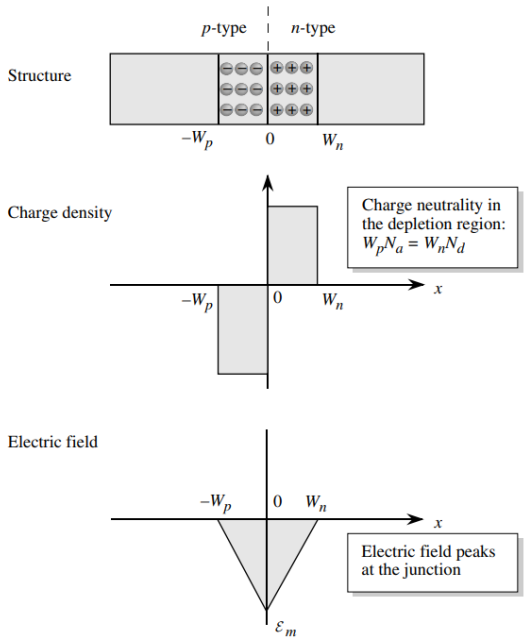

Figure 2.12. Charge and electric field profile of pn junction in depletion region

For now, the absence of applied bias is being investigated for depletion region. Despite no current flowing through the system both diffusion and drift currents still exist and

cancel each other out. However, when the bias is applied, the current flow, which depends on the diffusion and drift will be disturbed, resulting in a change in net current flow. Specifically, the change in current flow is due to the change in the potential barrier in pn junction. When bias is applied to material (either forward or reverse) the p-side or n-side will change, creating an imaginary potential barrier that prevents the electrons and holes passing through easily to the opposite regions (see Figure 2.13).

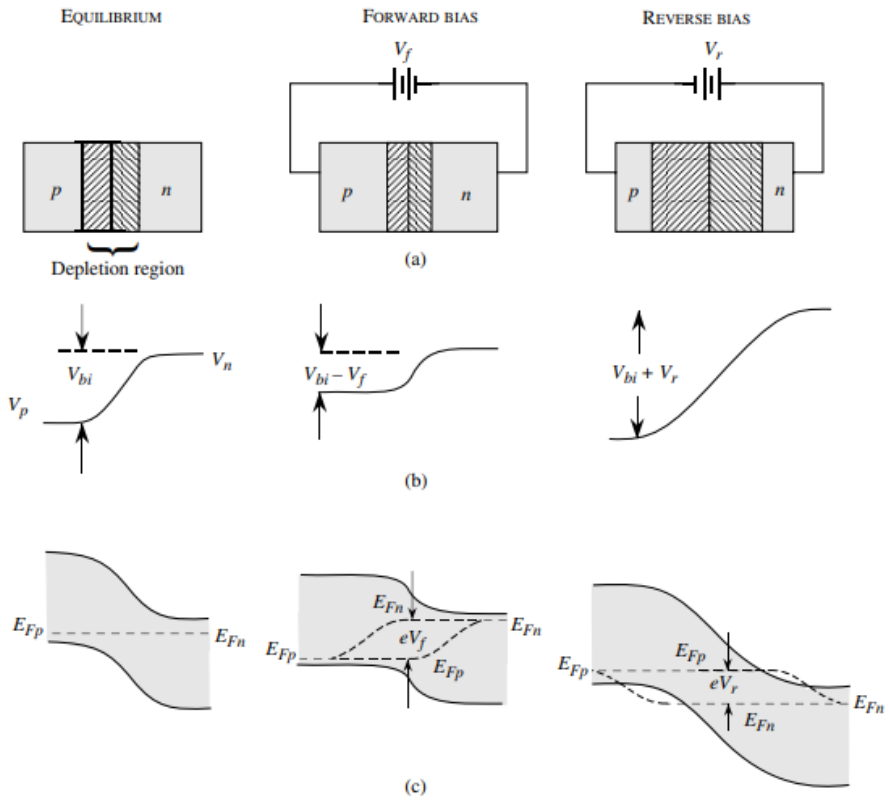

Figure 2.13. Illustration of pn junction and potential changes at equilibrium, forward and reverse bias conditions

Generally, the pn structure characteristic is defined by the minority carriers flow, electrons diffused to the p-side and holes diffused to the n-side. When reverse bias is applied domination of minority carrier flows is decreases as can be seen in Figure 2.14.

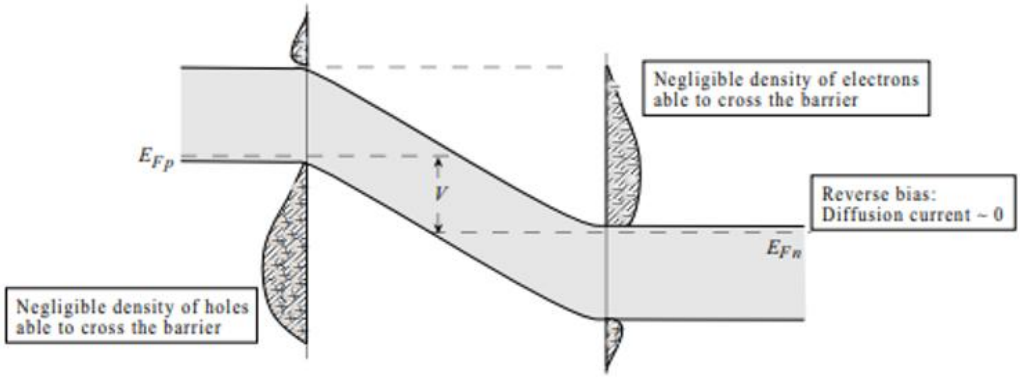

Figure 2.14. A schematic of pn structure under reverse bias condition

Additionally, the electric field in depletion region is reduced, resulting in an increase in diffusion current. However, this does not affect the drift current and due to change in bias condition diffusion current begins to dominate the system. Regarding this, the diffusion length of the material can be established.

$$W = X_n + X_p \tag{2.35}$$

$$V_{total} = V_{bi} - V = V_{bi} + V_R \tag{2.36}$$

Considering reverse bias case, the V is negative, $V = -V_R$.

$$p_n = p_p e^{\frac{-qV_{bi}}{kT}} \tag{2.37}$$

Under reverse bias conditions:

$$p(X_n) = p(-X_p) e^{\frac{-q(V_{bi}+V_R)}{kT}} \tag{2.38}$$

$$n(-X_p) = n_p e^{\frac{qV_R}{kT}} \tag{2.39}$$

To calculate the diffusion length of electrons and holes we need to derive the diffusion equation.

$$\frac{\partial(\delta n)}{\partial t} = D_n \frac{\partial^2(\delta n)}{\partial x^2} - \frac{\delta n}{\tau_n} \tag{2.40}$$

$$\frac{\partial(\delta p)}{\partial t} = D_p \frac{\partial^2(\delta p)}{\partial x^2} - \frac{\delta p}{\tau_p} \tag{2.41}$$

The final form of the equation 41 and 42 together is given below.

$$\delta p(x) = C_1 e^{\frac{X_n}{L_p}} + C_2 e^{-\frac{X_n}{L_p}} \tag{2.42}$$

$$\delta p(x) = C_3 e^{\frac{X_p}{L_n}} + C_4 e^{-\frac{X_p}{L_n}} \tag{2.43}$$

Where L_n and L_p are length of the electron and holes. According to the above equations the diffusion length of can be given as follows:

$$L_p = \sqrt{D_p \tau_p} \tag{2.44}$$

$$L_n = \sqrt{D_n \tau_n} \tag{2.45}$$

So far, we have investigated the pn junction diodes, on the other hand, the pn-type of materials have very limited depletion region. This situation results in the lower performance outcomes for the diodes. This can be improved by adding an intrinsic region between the p and n regions. Generally, the depletion region in pn type photodiodes is quite thin, resulting in incomplete absorption of incoming light. Instead of that in pin diodes the "i" region is growth as undoped or slightly doped n or p. Therefore, the electric field in depletion region without doping situation is constant while with doped situation slowly change to the edges. This creates the change in the generation of electron-hole pair per unit area and can be calculated by using Beer-Lambert law as follows:

$$G(x) = G_0 \exp(-\alpha x) \tag{2.46}$$

Where G_0 is the initial generation of electron and hole rate and x is the position of the generation rate occurs. The generation of electron-hole pair in system is increased with

thicker intrinsic layer, on the other hand growing too thick layer cause of higher noise and decreases the creation of electron hole pair in system.

2.3 Blackbody Radiation

Gustav Kirchhoff defined theoretically that blackbody radiation should follow the principle that what is absorbed should be emitted. Significantly, emitted radiation mostly concentrated in the infrared spectrum [13]. According to Kirchhoff's law the emissivity of blackbody is 100% and radiate all flux density and covers spectrum as can be seen in Figure 2.15. Blackbody radiation can be characterized if the temperature is known and mathematically defined as by Planck's equation as follows:

$$M_{e,\lambda} = \frac{2\pi hc^2}{\lambda^5} \frac{1}{\exp\left(\frac{hc}{\lambda kT}\right) - 1} = \frac{A_1}{\lambda^5} \frac{1}{\exp\left(A_2/\lambda T\right) - 1} \left[\frac{W}{cm^2} . \mu m\right] \quad (2.47)$$

Where $A_1 = 2\pi hc^2 = 3.74x10^4\ W/cm^2$ is first radiation constant and $A_2 = hc = 1.44\ cm.K$ h is Planck's constant, k is Boltzmann's constant, c is the speed of light in vacuum. The correlation between spectral radiant exitance $M_{e,\lambda}$ in longer wavelengths the formula shaped as follows:

$$hc/\lambda kT \ll 2 \rightarrow M_{e,\lambda} = \frac{2\pi ckT}{\lambda^4} \quad (2.48)$$

Otherwise:

$$hc/\lambda kT \gg 2 \rightarrow M_{e,\lambda} = \frac{A_1}{\lambda^5} \exp\left(-\frac{A_2}{\lambda kT}\right) \quad (2.49)$$

The mathematical formula originally derived by Planck is summarized for longer and shorter wavelength by Wien's and Rayleigh's laws. Essentially, these law state that as the temperature increases, the integration of the area under the curve increases at high rate and the peak wavelength decreases.

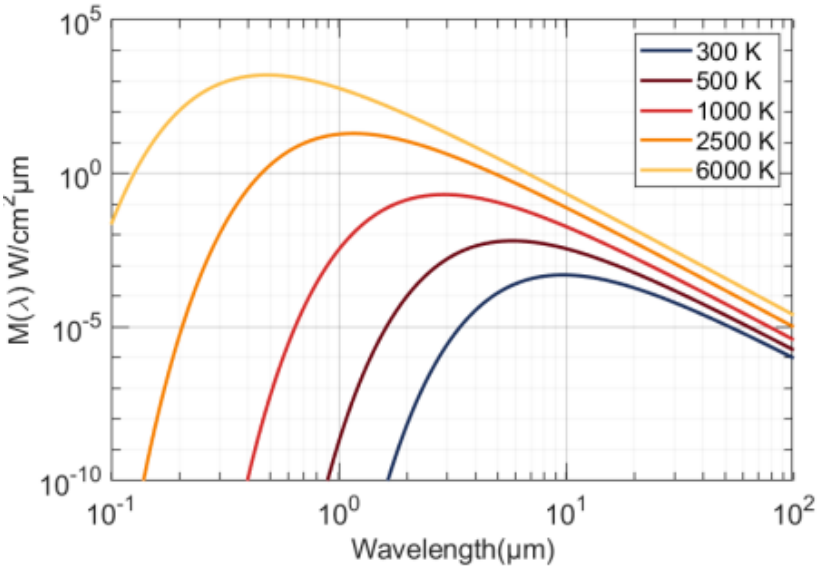

Figure 2.15. Spectral intensity to wavelength of solar radiation

The source of this radiation is the sun and the radiation power from very near to earth is 1.370 kW/m^2 [14]. However, this radiation does not reach the ground of the earth, due to atmospheric absorption and scattering. The atmosphere is composed of various gases and some of which, water and carbon dioxide, weakened or make opaque the infrared region while oxygen weakens mainly the visible range. Additionally, Rayleigh scattering occurs in short wavelength (< 2μm) of incoming radiation, due to dependence of λ^{-4}. Despite these factors, there are unique translucent parts that allow the certain wavelength to pass through known as 'atmospheric window' given in Figure 2.16 [15].

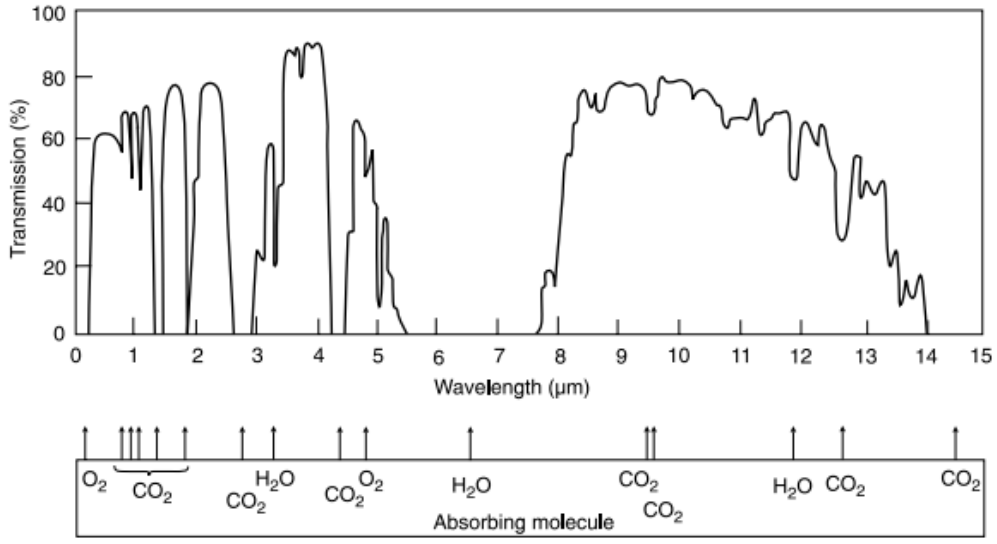

Figure 2.16. Transmission and absorption of radiation depend on molecules or gases in the atmosphere, from sea level to 6000 ft

Based on atmospheric window in infrared region is divided sub regions as mentioned in Chapter 1. Visible, NIR, SWIR and Extended SWIR regions use the reflected light from objects for detection. However, at room temperature and above, radiation happens over the 3 μm wavelength, which is where the detection of this range begins with MWIR, LWIR, VLIR and FIR.

Nightglow refers to the irradiation primarily originating from sources such as starlight or zodiacal light at night. This phenomenon occurs on moonless nights. Starlight originates from the Milky Way, while zodiacal light is produced by sunlight scattered or reflected off interplanetary dust. Detection and imaging using sub-infrared ranges, such as NIR, SWIR, and Extended SWIR, can be employed during nighttime (see Figure 2.17). Despite that, detectors or imaging systems operating over the 3 μm wavelength range do not require an illumination source. Their working principle is based on detection temperature differences between the target and background.

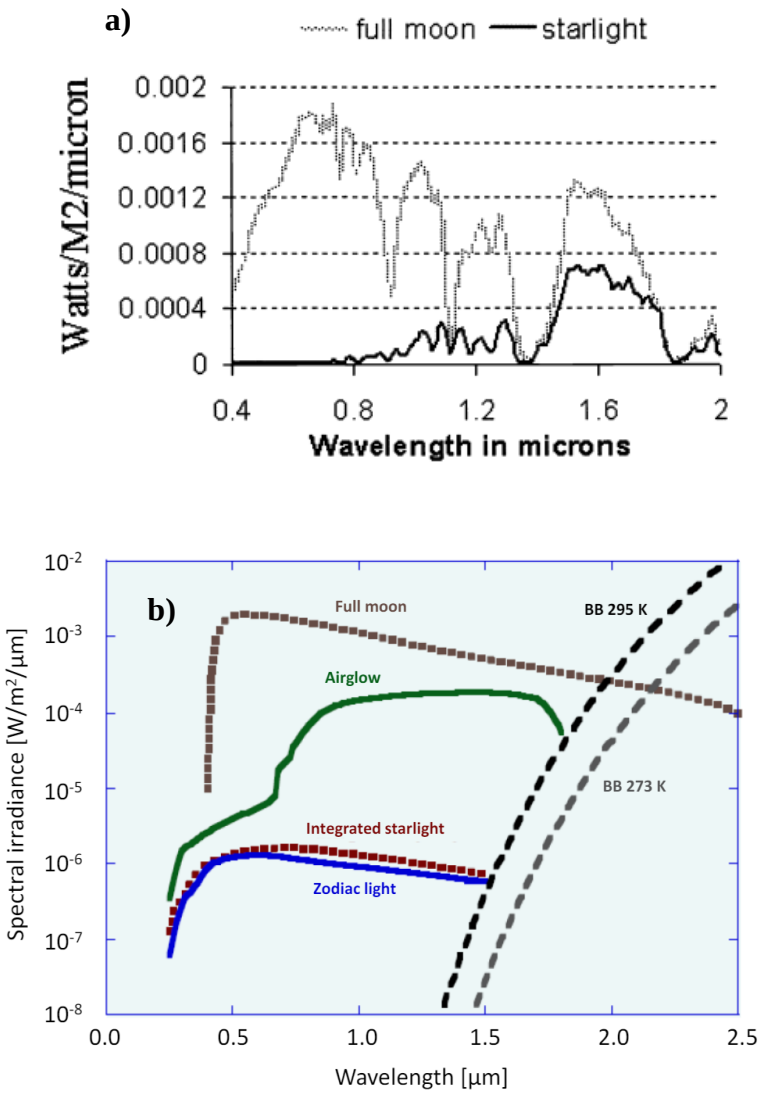

Figure 2.17. (a) The comparison of the full moon and (b) starlight days spectral irradiance

2.4 Figure of Merits

One of the most important evaluation criteria for the detectors is the detection of targeted light sources with minimum losses, which is defined in literature as the signal-to-noise ratio (SNR). The rest of the structure and the detector system should be designed for this purpose. The SNR concept encompasses various components, including photocurrent, quantum efficiency, dark current, and Johnson noise. Each of

these components consists of several parameters that require individual investigation. At the beginning, the focus will be on examining the dark current component, specifically its diffusion, generation and recombination, and tunneling parameters. Additionally, the experimental perspective will address parameters such as process control and layer thickness. Based on the results obtained from the analysis of dark current, the investigation will extend to responsivity, quantum efficiency, and determining the optimum size of the detector. Following this, the investigation shifts its focus to responsivity. Measurement of these parameters and comparing them in literature is determination of the performance outcome of the fabricated detector. In this thesis, these parameters are investigated from both theoretical background and experimental perspectives.

2.4.1 Dark Current

Dark current is a specific term used instead of "leakage current" in other electronic devices and it originates from thermally generated carriers. In photodetector system, it refers to measurement the detector's response without any light source. The measurement of dark current is one of the performance evaluation parameters, particularly detectors operating in nightglow region, as it affects the responsivity of the device. It can be measured under reverse bias condition, and when reverse bias is increased, the dark current increases in parallel.

$$I_d = I_s \left[exp\left(\frac{qV}{kT}\right)\right] - 1 \tag{2.50}$$

Where q is charge of the electron, I_s is the reverse saturation current, V is the applied reverse bias, k is the Boltzmann constant, and T is the temperature [16]. Additionally, the saturation current I_s is expressed as:

$$I_s = n_i^2 A (qkT)^{1/2} \left[\frac{1}{N_D} \left(\frac{\mu_p}{\tau_p}\right)^{1/2} + \frac{1}{N_A} \left(\frac{\mu_n}{\tau_n}\right)^{1/2} \right] \tag{2.51}$$

Except for the ideal photodiode, there are few components which affect the dark current such as defects and traps. Defects can be summarized as shallow-level defect and deep-level defect. Shallow level defects occur due to dopant atoms in system, likewise the deep-level defects dopants takes place substitutional atoms locations and cause a vacancy or any other defects. Deep-level defects are types of disordered lattices, and every disordered line and point generates unwanted acceptor or donor regions. Traps are unoccupied locations in detector systems that create the energy transformation states which cause a decrease in performance of detector. Dark current originated from these problems and resulted in several mechanisms such as generation-recombination current (G-R current), tunneling current, diffusion current, surface leakage and ohmic leakage. Every one of them is required to optimization in fabrication of detectors and choose coherent growth materials and design.

2.4.1.1 Generation-Recombination (G-R) Current

Generation of electron-hole pair happens when light falls into the absorber layer and one of the electrons jumps to the higher energy level and leaves behind a hole. This process ends up in thermal equilibrium, where an electron transition from high energy level to the lower energy level, emitting light. The energy of the emitted light almost corresponds to the energy difference between the two energy levels involved in the transition. This process is known as radiative recombination. Radiative recombination is more likely to happen in direct band gaps compared to indirect band gaps due to phonon effect. In addition to radiative recombination, there is another recombination mechanism that results in non-radiative recombination which is known as Shockley-Read-Hall (SRH) recombination.

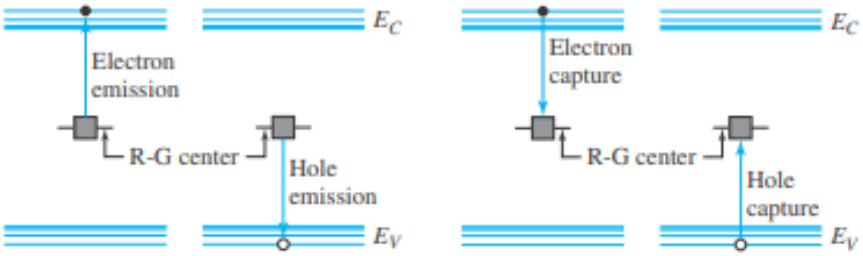

Figure 2.18. Left-side illustration represent the electron and hole emission from R-G center and right-side illustration represent the electron and hole capture center

SRH happens due to the nature of the growth with defects or doping with impurities [17]. Generally, there are four different recombination method exist as shown in Figure 2.18. Two of them are related to electrons (emitting or capturing) and the other two to holes (emitting or capturing). In summary there is a correlation between electron density in conduction band and the density of empty states in trap centers. The excitation of electrons with thermally increases the recombination rate as well as the empty states. Accordingly, the recombination rate (R_c) and emitting centers (G_c) can be expressed as:

$$R_c = V_{th}\sigma_n n N_T(1-f) \tag{2.52}$$

$$G_c = e_n N_T f \tag{2.53}$$

Where V_{th} is thermal velocity of charge particle, $\sigma_n n$ term is electron density in cross section and $N_T(1-f)$ empty states in trap centers. The same equation series can be applied to the holes. In conclusion, the recombination lifetimes of the electron and hole can be expressed as:

$$\tau_{po} = \frac{1}{V_{th}\sigma_p N_T} \tag{2.54}$$

$$\tau_{no} = \frac{1}{V_{th}\sigma_n N_T} \tag{2.55}$$

Let's assume that τ_{no} and τ_{po} are equal, and from this can be derived the total recombination lifetime as τ_{GR}. The depletion region where the recombination happens and the increase in width correspond to an increase in current and it affects the recombination lifetime. Regarding that, density of charge particles gives us the total G-R current from that the I_{GR} can be defined as:

$$I_{GR} = \frac{qn_i WA}{2\tau_{GR}} \tag{2.56}$$

SRH is a fundamental parameter in the characterization of dark current mechanism, and it provides key insight into crystal purity. In an ideal photodiode, the increase in built-in potential leads to with exponential increase in the GR current in forward bias. Regarding that the diffusion current should also increase exponentially. Because of this, in an ideal photodiode the ideality factor (n) which is explained as the ratio between GR and diffusion current, is equal to 1. However, in the real world the ideality factor never reaches 1 due to growth techniques. Researchers assess the quality of their crystals by calculating how close the ideality factor is to 1.

2.4.1.2 Diffusion Current

An increase in dark current resulting in a decrease in SNR and a decrease in photodiode performance. In the previous part of the thesis, the diffusion current was expressed and shown to be related to the saturation current (Equation (2.50) and (2.51)). Controlling the dark current can be achieved by controlling the doping level and density of the p or n side in pin type photodiodes. Increasing the doping level of intrinsic layer can cause a decrease in saturation current. However, decreasing too many leads to decrease in depletion region and as result, tunnelling current can dominate the system. This situation leads to an increased dark current.

2.4.1.3 Tunneling Current

The third dark current mechanism is tunneling current which is responsible for leakage in depletion region shown in Figure 2.19. Essentially, the leakage current can occur in two different ways: band-to-band tunneling current (BTB), and trap assisted tunneling current (TAT). BTB tunneling current occurs when electrons jump from valance band to conduction band, whereas TAT tunneling current involves electrons transitioning from the valance band to trap levels in the depletion region and then to the conduction band.

BTB current is most likely to happen in very low band gap type infrared detectors, particularly for detection longer wavelength. Even slight thermal changes are capable of generating significant BTB current due to low bandgap energy difference between valance to conduction. However, in higher bandgap materials the BTB starts to dominate the dark current with higher bias voltages.

Despite of the BTB, TAT is more possible due to electrons have a shorter distance to tunnel. Because of that, the TAT current start to dominate slightly lower bias voltages than BTB. The source of the TAT current is related to growth parameters and doping concentration. Mismatched lattice or lower doping levels can create trap centers and act as acceptor and increase dark current.

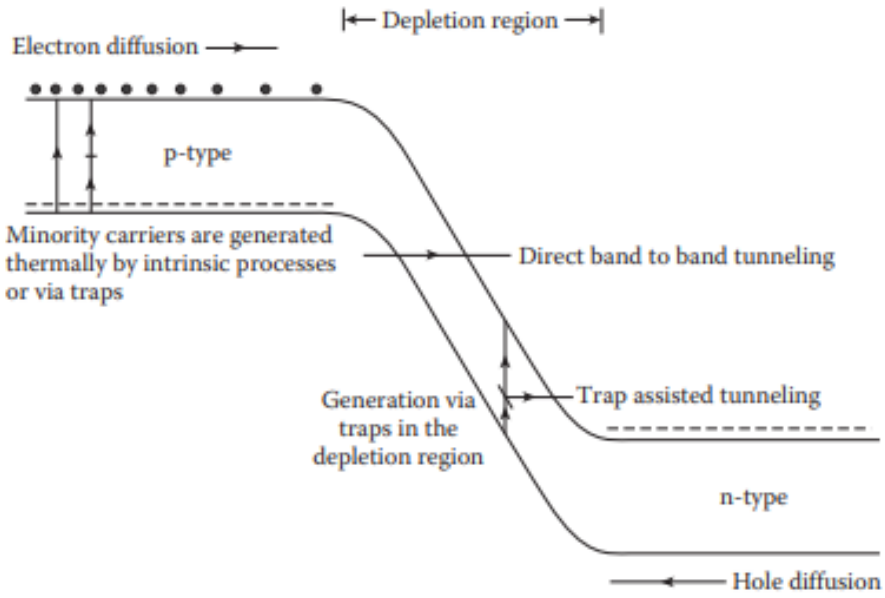

Figure 2.19. Illustration of tunneling current mechanism for direct band-to-band and trap assisted tunneling currents

2.4.1.4 Surface Leakage Current

Until now dark current mechanism is investigated according to epitaxial based components. Besides with the epitaxial growth quality and doping concentration, the maturity of detector fabrication has a severe effect on the performance of photodiodes. In particular, the application of efficient surface passivation can reduce the negative performance effects brought by surface. The discontinuity occurs at the surface creates highly concentrated interface states which are one of the G-R current sources.

The surface of photodiodes generally passivated with different dielectric materials to decrease the surface interface related leakage current and also protect the surface. Passivation of surface creates fixed charge with dielectric thin films which electrical properties is determined. The dangling bonds between the surface and the dielectric film are reduced with neutralized fixed charges. The effect of surface based dark current will be deeply investigated in this thesis with different passivation recipes.

2.4.2 Responsivity (R)

A photodetector's performance is evaluated based on its efficiency in converting photon signals into electrical output. As discussed theoretically in the dark current section above, dark current defines as the baseline electrical output of a detector. Photo current represents the electrical output of the detector corresponding to the amount of photon converted into an electrical signal, wheatear voltage or current. Responsivity, therefore, is defined as the ratio between photo current and the incident power of photons. This can be expressed as follows:

$$R = \frac{Electrical\ Output\ Signal}{Incident\ Power} = \frac{I_{photo}}{\Phi_e} \tag{2.57}$$

Where Φ_e represents the power of incident photon, measured in Watts. Incident photon is expressed as follows:

$$\Phi_e = \Phi_p \frac{hc}{\lambda} \tag{2.58}$$

In equation (2.58 the Φ_p represents the amount of incident photons, and according to that photocurrent is written as follows:

$$I_{photo} = nqg \tag{2.59}$$

$$\eta = \frac{n}{\Phi_p} \tag{2.60}$$

Where g is photoelectric current gain, n represents the amount of generated electron-hole pairs and q is the elementary charge. And the η represents the quantum efficiency of a detector, indicating the ratio of incoming photons that results in the generation electron-hole pairs.

Responsivity measures the degree of photogeneration is occurring in diode which correlated with quantum efficiency as given in below equation:

$$R = \frac{\lambda\eta}{hc} qg \tag{2.61}$$

Where q is the electron charge. Responsivity is increased with the absorption length and decrease in dark current. Decrease in dark current corresponds to increased gain, resulting in higher responsivity.

2.4.3 Quantum Efficiency (η)

According to theoretical explanation (see equation (2.60), every photon that contacts with material sensitive to the wavelength of the incoming photon should create an electron hole pair in structure. However, in the real-life case this scenario diverges from theoretical prediction. There is a probability that needs to be considered.

The spectral responsivity of diode demonstrates a tendency for maximum electron-hole pair generation to occur at the peak wavelength, with diminishing efficiency for other wavelengths. The cause of the power absorbed is decay as function of penetration depth of the light inside the material.

$$P_a = P_i(1-r)(1-e^{-\alpha x}) \tag{2.62}$$

Where P_a is power absorbed, P_i initial power α absorption length and r are the reflectivity (see Figure 2.20). The quantum efficiency is defined as:

$$\eta(x) = (1-r)(1-e^{-\alpha x}) \tag{2.63}$$

The above equation demonstrated that the quantum efficiency of diode depends on the absorption length of the material. If wavelength varies, this results in change in photon energy, thereby directly impacting responsivity.

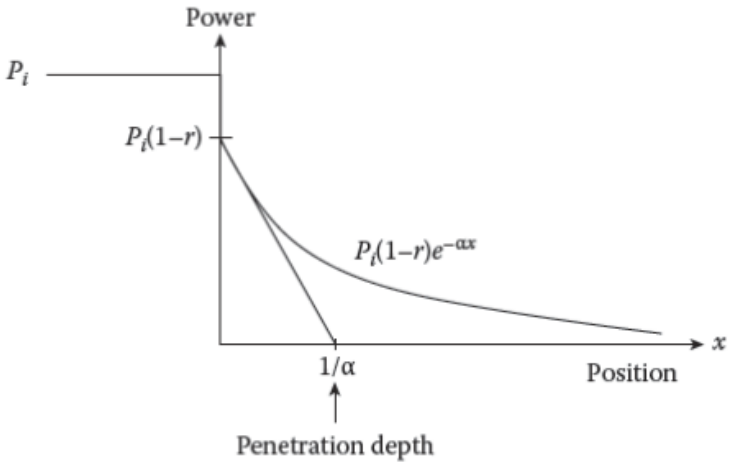

Figure 2.20. Absorption length of photon in semiconductor

2.5 Scope and Objective of Extended SWIR Technology

The spectral range of the "classical" InGaAs SWIR detection extends to ~1.7 μm and the peak responsivity at 1.55 μm. This range has been covered by InGaAs SWIR technology for over three decades due to high quantum efficiency, repeatability and low dark current cost. In years, the SWIR technology spread and gain high usage area in industrial telecommunication and military. Even though, SWIR has been acceptable all these years and make all the communication point in infrared region at 1.55 μm, there is a lack of performance parameters. SWIR technology requires higher illumination for imaging or detection purposes. Additionally, SWIR cannot detect through cloud, haze or rain due to larger water particles and the detection limits decay with longer range as can be seen from Figure 2.21 [18].

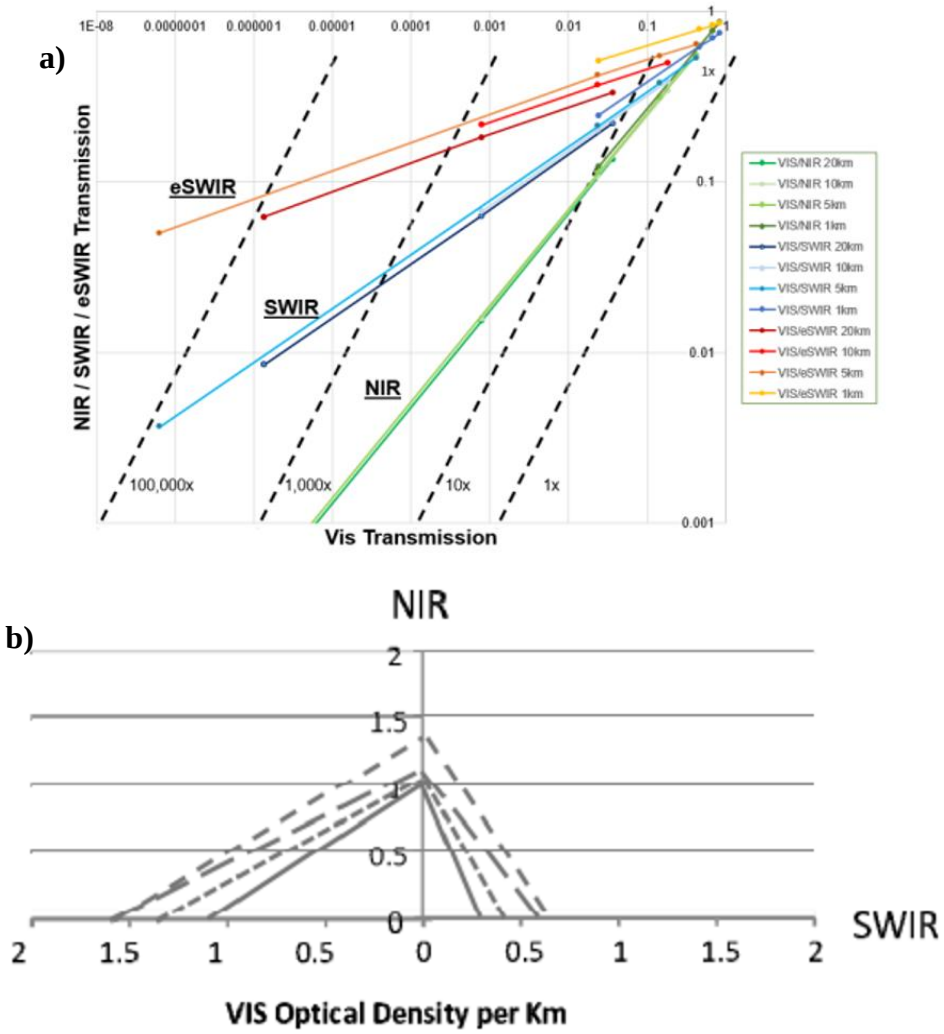

Figure 2.21. (a) Different region of atmospheric window and transmission limits for e-SWIR, SWIR,NIR and Visible, (b) Detectivity limit per kilometer

On the other hand, extended SWIR (e-SWIR) technology offers higher opportunity for over >2 µm wavelengths, particularly under lower illumination conditions. E-SWIR technology slightly captures information from the thermal region of the infrared spectrum, giving it an edge over traditional SWIR [19]. Furthermore, e-SWIR, ranging from 2 µm to 2.6 µm, exhibits higher transmission and resulting in longer detection range graph can be seen in Figure 2.22. This capability provides a significant advantage for hyperspectral and fusion and military imaging applications.

The development of e-SWIR based detection and imaging research has been rapidly increasing since the late 1990s, starting with the SCIAMACHY atmospheric observation experiment [20]. This progress was necessitated by the interference of water vapor in the atmosphere, which absorbs wavelengths ranging from 1.3 to 2 μm, prevent detection and imaging applications.

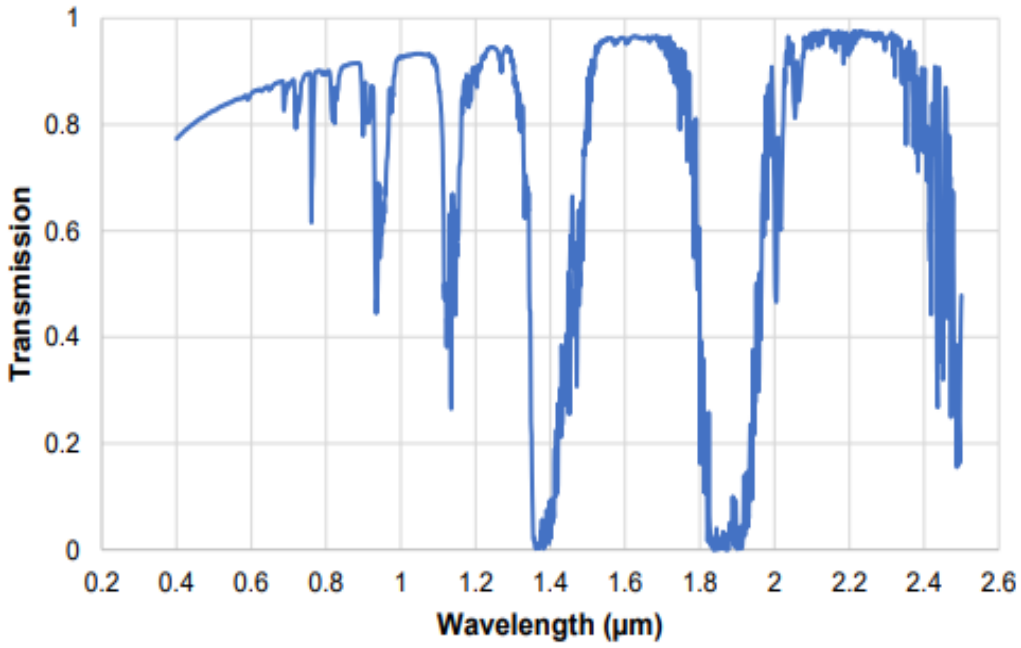

Figure 2.22. Transmission spectrum of visible to e-SWIR

Since then, over the past 20 years, there has been a significant amount of research and experimentation aimed at enhancing the detection performance of e-SWIR photodiodes. Nowadays, the application areas of e-SWIR have expanded to include a variety of applications such as gas detection [21], [22], as well as medical or industrial uses [23].

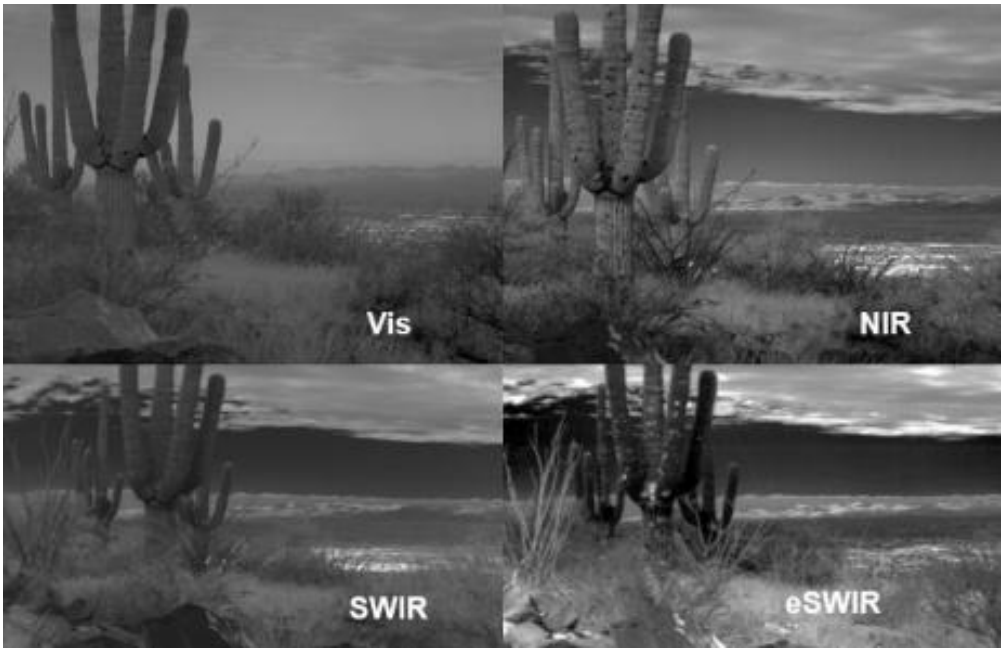

Figure 2.23 Different light spectrum images captured with variety of visible and infrared range cameras

Chapter 3 will provide a comprehensive discussion on the scope of this technology and the current status of devices, delving into intricate details to offer a thorough understanding of the subject matter.

CHAPTER 3

EXPERIMENTAL BASIS

In this chapter of this work, suitable materials and growth methods will be investigated. The discussion will begin with virtual buffer layers and threading dislocations issues and will conclude with common usage. Additionally, the importance of dry and wet etching fabrication procedures will be covered, along with their advantages and disadvantages. Following that, the optimization of passivation for infrared detector will be explained. Finally, the use of backside reflector for infrared detectors and their impact on detector performance will be explored.

3.1 InGaAs/InAsP Material Concept

There are various methods for developing high-performance PDs in e-SWIR, including p-i-n, nBn [24], nBp [25], type-II superlattices (T2SL) [26], using materials such as InGaAs, InAsP, Mercury Cadmium Telluride (MCT) and GaSb/AlSb as illustrated in Figure 3.1. However, for current technology reducing the detector size and weight, power consumption and cost is necessary. Except the InGaAs, all other technologies suffer from high cost, reproducibility and fabrication issues. Due to its maturity of InGaAs technology remains highly desirable for e-SWIR PDs.

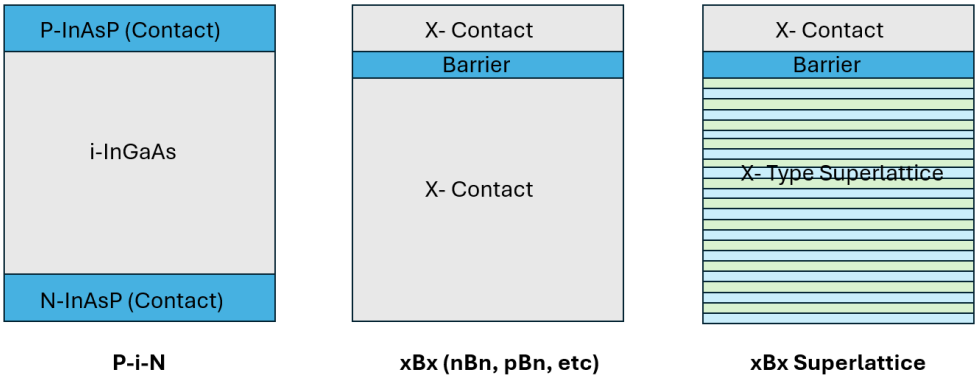

Figure 3.1. Diagram of various PD structures

InGaAs for SWIR contains 53% In and is nearly perfect lattice matched with InP material. Consequently, there is no need for further material development and research in terms of product-level perspective with current technology. On the other hand, to detect the e-SWIR with an InGaAs absorber layer, the In mole fraction needs to be increased to 83%. As depicted in Figure 3.2. The increase in In mole fraction induces compressive strain in epitaxial structure, resulting in lattice mismatch of around 2% [27]. This mismatch causes, the SRH as mentioned above, recombination in the system, leading to a decrease in the SNR with high dark current density and low quantum efficiency of detectors. Despite the traditional SWIR InGaAs, extended InGaAs has narrower band gap, resulting in higher dark current and lower responsivity due to SRH and Auger recombination processes. The nature of these material limitations necessitates solutions.

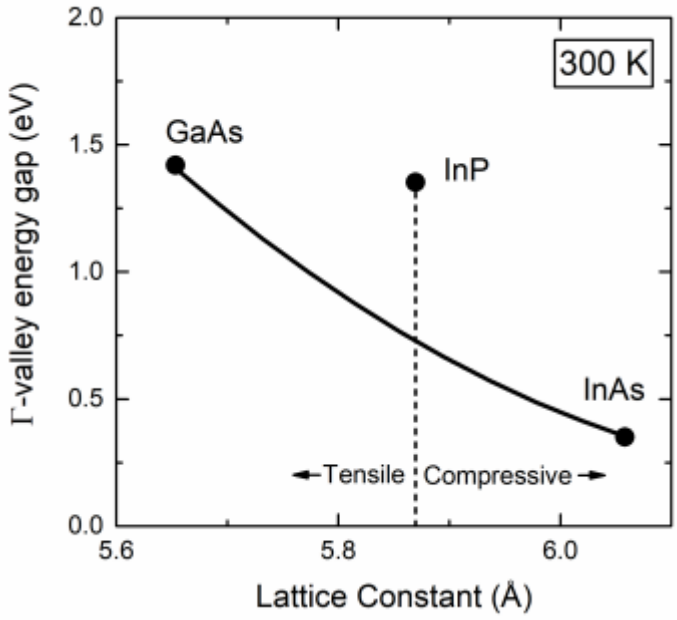

Figure 3.2. Relationship between mole fraction and lattice constant

Over time, methods have been developed to reduce the effect of these dislocations with different materials [28]. Currently, the most effective method for reducing the impact of dislocations due to the mismatch is through metamorphic buffer layers. There are numerous kinds of buffer layers have been tested between increased In with InGaAs and InP, including thick buffer layer [29], linear-graded [30], [31], step-graded [32], [33], [34], [35], superlattice type buffer layer [36]. Each method has unique pros and cons; deciding which to proceed with depends on the application.

Deciding the imaginary substrate (buffer layer) for the InGaAs with increased In first need to decide the material due to changing material has impact on the properties of the buffer layer. Various types of buffer layer are tested for between active layer InGaAs and the substrate InP, including InAlGaAs [37], [38], InGaAsP [39], AlGaAsSb [40]. Growth of the quaternary materials requires highly controllable growth conditions and increased the cost of the device. On the other hand, $In_xAl_{1-x}As$ and $InAs_yP_{1-y}$ materials already exhibit ideal characteristics with $In_{0.83}Ga_{0.17}As$ [21]. $InAs_yP_{1-y}$ demonstrate better performance characteristic despite of the $In_xAl_{1-x}As$ for both infrared detectors and imaginary device applications due to tunable band

gap energies [41]. The difference between AsP to AlAs arises again the growth rate and controllability. While $InAs_yP_{1-y}$ has double-anion (group-V), $In_xAl_{1-x}As$ has double-cation (group-III) elements. When growing InGaAs, a phase separation problem occurs between In, Ga and Al as all three are in group-III elements. Conversely, with $InAs_yP_{1-y}$ the problem does not occur and this makes the growth conditions and controllability higher [42]. When growing the InAsP over InP the main purpose is to reduce defects, so the virtual buffer layer must ensure the minimization of threading dislocation. Step-graded InAsP has been shown to provide strain relieved alloy composition with InP [27].

In this thesis work, an n-type step graded virtual buffer layer was grown on traditional InP substrate with a sufficient thickness to eliminate the effect of lattice mismatch besides dislocation formation followed by thick $InAs_{0.6}P_{0.4}$ layer as n contact. Besides the n-contact also p contact and cap layers are designed to be InAsP ternary alloy format. Due to higher tunable band gap energy of InAsP (0.36 eV to 1.35 eV) and band off set leads to better performance values with InGaAs active layer [43]. Even this band gap tunability gives the opportunity to homojunction InAsP structures to detection of e-SWIR [44]. However, the complexity of epitaxy growth with Ga free structure is quite challenging and this makes InGaAs still favorable device active layer.

3.2 Etching Characteristic of Optoelectronic Devices

The uniformity of etching across the device substrate, controllability, reproducibility and reduced cost are crucial factors in nano fabrication processes. However, the nature of certain materials does not permit working with different chemical etchants such as plasma or wet formations. On the other hand, InGaAs and InAsP materials stand out as unique options that offer higher yield and reproducibility compared to other III-V semiconductor materials. Typically, wet etch is more suitable for optoelectronic devices due to plasma system suffering from surface roughness concerns. The device surface is already considered as defect center and plasma

etching can exacerbate this issue by causing damage and increased surface roughness. This can lead to reduced device performance due to dangling bonds which are source of the surface related dark current. Transforming these dangling bonds into fixed charges on the surface or device etching sidewalls is necessary to mitigate this issue.

3.2.1 Dry Etching

The initial need for plasma etching arises from the requirement to achieve precise feature sizes in semiconductor manufacturing. While wet etching is isotropic and provides high selectivity, it is limited in terms of feature size. This limitation hinders the technological progress of optical devices. In contrast, dry etching offers a higher surface-to-volume ratio across the wafer scale. Despite this advantage over wet etching, dry etching also has its drawbacks. Crystal damage and diffusion of various components to the epitaxial surface are major issues associated with dry etching.

Since the optimization of the etching process of InP, various compounds have been used as reactive gases. In the early stage of the plasma etching, InP material were etched with Cl-based chemistries, including Cl_2, BCl_3, $SiCl_4$, CCl_2F_2 [45]. However, the etch rates are considerable low and process temperatures around >130^oC due to low volatility of $InCl_x$ materials. On the other hand, over time CH-based gases have gained more attention over time due to their favorable specification, such as being nontoxic to environment and non-corrosive features. High volatility of CH-based chemistries, such as C_2H_6 and CH_4 allow processing around 100 ^oC.

The primary challenge is the interaction of reactant gases with In, especially in our cases where InAsP-InGaAs materials have relatively high In mole fraction. Removing the In content in the epitaxy, substrate temperature needs to be elevated for Cl_2 based gases. On the other hand, using CH_4/Cl_2 gases for removal allows for low temperatures compared to using Cl_3 based alone. As briefly mentioned above, the properties of BCl_3/Ar and $CH_4/Cl_2/H_2$ gases given in Table 3.1.

Table 3.1 Comparison of Cl2/Ar and CH4/Cl2/H2 gases according to various parameters

BCl_3/Ar	$CH_4/Cl_2/H_2$
• High temperature process >**190ºC**	• Moderate temperature process >**60ºC**
• **Hydrogen/Polymer** free	• Etch rate >0.4 μm/min
• Etch rate >0.8 μm/min	• Smooth **sidewall** and **surface**
• Smooth **sidewall** and **surface**	• **Highly controllable** profiles
• **Waveguide** or **photodiode**	• **Wide process** window
• **InP, InGaAs, InAsP**	• **InP, InGaAs, InAsP**

Dry etching differs from wet etching primarily in masking fabrication owing to the anisotropic features of dry etching. Dry etching begins with the application of suitable dielectric coatings that can withstand over the process duration. This necessitates the optimization of dielectric films to avoid creating additional dangling bonds on the surface or preventing transformation of fixed charge. In this chapter, the properties of dielectric materials will not be explored in detail; instead, it is assumed that the dielectric material poses no issues. Typically, the chemistry of InGaAs and InAsP materials involves Cl_2, which is very reactive with the III-V semiconductors, including Ga, As, Al, In and P. The etch rate with Cl_2 gas is more controllable, offering smooth sidewalls and surfaces. Ar is used in this chemistry to sweep out the residual gases from the etched area. However, the presence of Ar can cause a microtrenching at the bottom of the etched area and can damage the sidewalls, as can be seen illustrated Figure 3.3.

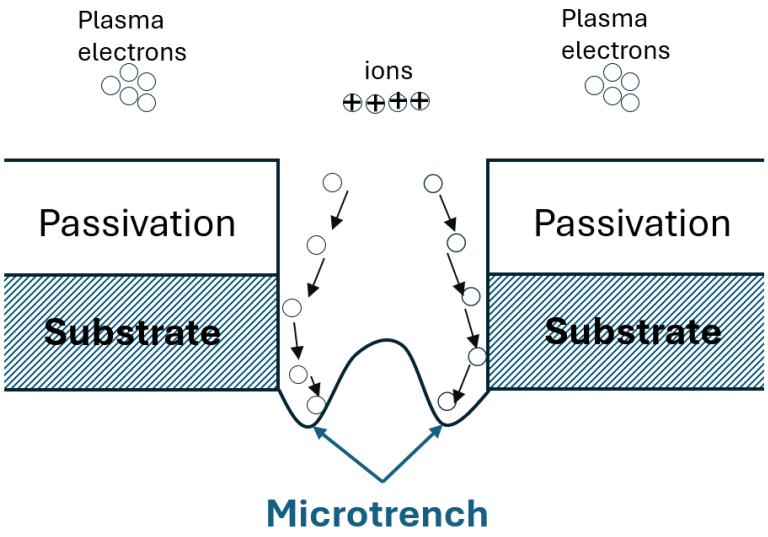

Figure 3.3. Illustration of microtrench

Low temperature is relatively important for e-SWIR detectors as higher temperature can lead to an increase in crystallographic defects in the epitaxy. These defects act as trap centers and can reduce the performance of the device. Therefore, removing the Ar and reducing the temperature can give better process windows for e-SWIR PDs. However, the existence of H_2 can create another problem, which is diffusion. Increasing the H content in plasma system with the help of the bombardment can cause a diffusion of H into epitaxy. These diffused H can be able to act as donor or acceptor complexes [46], [47].

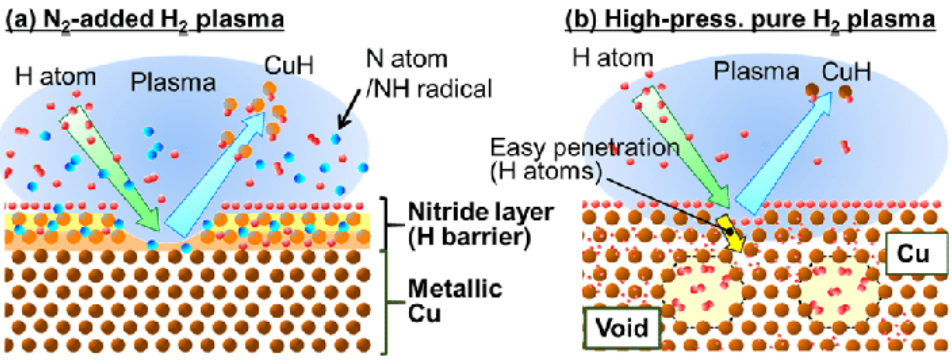

Figure 3.4. Illustration of Hydrogen diffusion to metallic surfaces[48]

The second thing that needs to be considered is the pressure of the process chamber which affects the flow of gases into the chamber. Higher pressure results in more gas

molecules present in the discharge, attacking the substrate. In this etching condition, the radicals and ions produced by reactive gases react with substrate, forming a polymer. This polymer cannot escape from surfaces due to higher gas concentration over the substrate. Conversely, lower pressure provides more control over the etching condition which is resulting in higher anisotropic as can be seen in Figure 3.5.

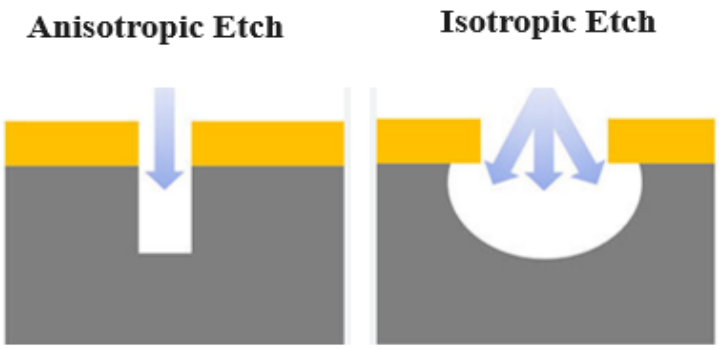

Figure 3.5. Illustration of anisotropic and isotropic etching

The decrease in pressure also results in a change in the critical dimensions (CD) feature size. In optoelectronic devices sidewalls are relatively important as they contribute to an increase in electrical conductivity and alter the properties of device. Isotropic etching results in particles having a lower mean free path which causes them to attack the sidewalls of the etched area. On the other hand, low pressure can create higher energetic particles with a longer mean free path. Therefore, the sidewalls of the area are more vertical. However, an excessive increase in energetic particles can cause microtrenching due to collision between particles. The Table 3.2 below provides a detailed comparison of pressures.

Table 3.2. Comparison of pressure differences effect on etch surfaces.

Low Pressure	High Pressure
• **High anisotropic** (vertical) o **Mean free path** is **long**	• **High isotropic** (undercut)
• Easy **CD control**	• Hard to control CD
• Lower **rate** and **selectivity** o Due to **higher energetic** particles	• Higher **rate** and **selectivity**

3.2.2 Wet Etching

Even though technological advancement creates wide perspective control over the dry etch process, the nature of the wet etching still exists and works relatively well. Etching process mainly depends on the whether the etchant isotropic or anisotropic. Materials show almost the same behaviors to the etchant and related materials generally used with related etchants. Because of that people are still using the wet etchant process. Even though, dry etched process ends with wet etch processes as treatment for neutralization of dangling bonds or pre-treatment.

InGaAs and InAsP materials are selective for H_3PO_4 (ortho-phosphoric acid) and H_2O_2 (hydrogen peroxide) chemical mixture, additionally, they are sensitive to $C_6H_8O_7$ (citric acid) , HNO_3 (nitric acid) and CrO_3 (chromium trioxide) based mixtures [49], [50]. All these chemicals the composition consist of three parts: the agent that oxidizes, the agent that removes the oxidized molecules and dilution. In these chemicals mixtures the dilution and the oxidizing agent is generally DI water and H_2O_2. Controlling the ratio will determine the etch rate and sidewall angle with photoresist component.

3.3 Passivation of InAsP

Besides with the epitaxial growth quality of InGaAs-based e-SWIRs, the maturity of detector fabrications has a severe effect on the performance of PDs. In particular, the application of efficient surface passivation can reduce the negative performance effects brought by surface. So far, several types of passivation materials, such as SiO_2 , ALD-Al_2O_3 [17], HfO_2 [18] and surface treatments like HCl solution based [19], N_2 [20], and $(NH_4)_2S$ [21] have been effectively used to improve the long-term performance of PDs by minimizing dangling bonds and interface states in literature. Unfortunately, III-V semiconductors are highly susceptible to oxide formation due to their tendency to have defect-rich surfaces. Although the performance of each of these passivation materials varies based on coating parameters and methods, defects still tend to degrade PD performance significantly if not properly optimized [22], [23]. SiO_2 has been one of the major passivation materials used and investigated for III-V semiconductor materials over the last 50 years. However, the performance of this material has revealed that the amorphous oxidation of III-V materials is challenging. SiO_2 is an oxygen-rich material and can readily form bonds with semiconductor materials [24]. Qin et al. demonstrated that using oxygen-rich passivation, including SiO_2 and HfO_2, is a challenging research area [25]. In addition to SiO_2 and HfO2, the ALD method has shown more stable coatings with Al_2O_3. However, the ALD method demonstrates better performance with pre-treatment to remove native oxide from the surface. Tuominen et al. demonstrated that Ar-ion sputtering combined with vacuum heating before coating Al_2O_3 reduces the leakage current by a factor of 10 compared to samples containing native oxide [17]. Besides the aforementioned passivation materials, amorphous silicon nitride (SiNx:H) is widely used for masking and passivation due to its high dielectric constant, high density, and anti-oxidation properties, which offer superior electrical and optical performance. So far, there has been limited research published that investigates the broad impact of Hydrogen (H) content in SiN_x:H passivation for InGaAs in e-SWIR range. Because of that the thesis focuses solely on SiN_x:H based passivation method.

One of the passivation materials used for this purpose is the low Hydrogen (H) content amorphous silicon nitride (SiN_x:H) deposited by PECVD (200 ºC<T<400 ºC) method [51], [52]. Contrary to the higher temperature requirement for better film quality in PECVD, the ICPCVD method provides high-quality thin films at lower temperatures (T<200ºC) [53]. Xing Huang and his colleagues used an ICPCVD method for passivation of diodes of 50 µm x 50 µm and were able to attain noise current spectral density (A^2/Hz) values that were around 100 times lower than diodes passivated by PECVD-deposited films [54]. Likewise, Ming Shi et al. showed that passivation tests performed with the ICPCVD method produced noticeably improved dark current density, approximately 5-6 times better than PECVD, in their investigations involving 30 µm x 30 µm and 200 µm x 200 µm devices [55]. These results indicate that the ICPCVD when compared to other methods like PECVD, is a very efficient method for particularly passivating III-V semiconductor materials.

The amount of H and the type of bonds within the structure play a crucial role in determining its electrical and optical properties, particularly in controlling leakage current. To minimize leakage currents caused by surface effects, SiNx:H films with the highest possible dielectric constant (high-k) are required [56]. In this context, changes in the amount of Si-H bonds significantly influence the material's electrical properties. Conversely, N-H bonds within the film can be utilized to control optical absorption properties [57]. However, an increase in H content can make the film thermally unstable, as it is strongly correlated with hydrogen blistering in thin films caused by temperature changes (see Figure 3.6), a well-known fabrication challenge. The SiH_4 gases play a significant role in the coatings of SiN_x:H, being the main source of the hydrogen content. Increasing the SiH_4 content in the mixture of chamber gases significantly exacerbates the blistering effect and alters the properties of the dielectric films.

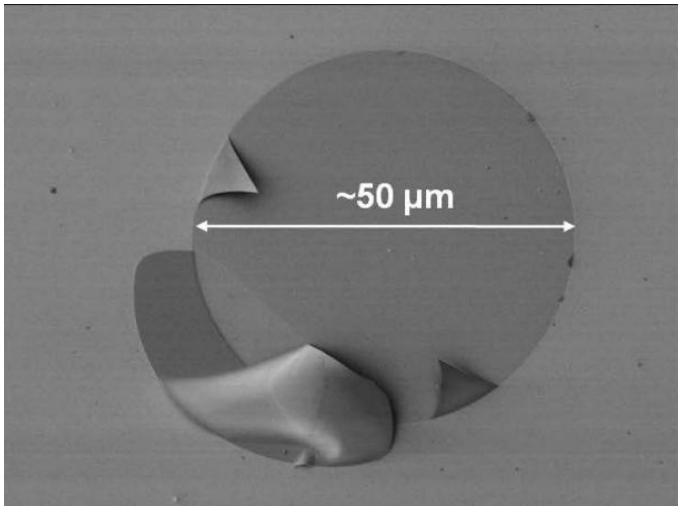

Figure 3.6. Blistering effect on SiN_x:H thin film

3.4 Recent Breakthroughs in Device Technology

The SWIR detectors and FPAs have been established technologies for over half a decade, with significant research and fabrication conducted in the infrared region during this time. However, both SWIR and e-SWIR technologies require illumination and are used for photon detection within the same wavelength range. The need for e-SWIR developments arises from the requirement for extended range detection, particularly for military purposes. Atmospheric scattering or absorption can limit the detection of SWIR in long range applications. In contrast, e-SWIR diodes offer enhanced range detection and targeting capabilities, especially in challenging visual conditions such as heavy rain, fog, dust, and smoke. Wiley et al. conducted a comparison of SWIR and e-SWIR detection capabilities in various environmental conditions, as shown in Table 3.3, demonstrating that e-SWIR devices exhibit superior detection performance under different environmental scenarios.

Table 3.3. Range performance comparison of SWIR and e-SWIR [18]**.**

Degraded Visual Environment	SWIR (km)	e-SWIR (km)
23 km visibility	9.48	14.7
5 km visibility	6.22	11.0
Smoke (23 km)	9.69	14.02
Smoke (5 km)	6.44	10.7
Haze	4.98	7.45
Light Rain	1.78	2.21
Heavy Rain	1.27	1.57
Dust	0.48	0.69
Fog	0.22	0.25

Target recognition and discrimination in the field of battle is crucial. Therefore, Breiter et al. conducted a comparison of target detection performance using VIS, NIR, SWIR, and e-SWIR devices in a simulated battle scenario. As illustrated in Figure 3.7, laser spots are highly detectable in e-SWIR, and target recognition yields better results compared to thermal imaging techniques.

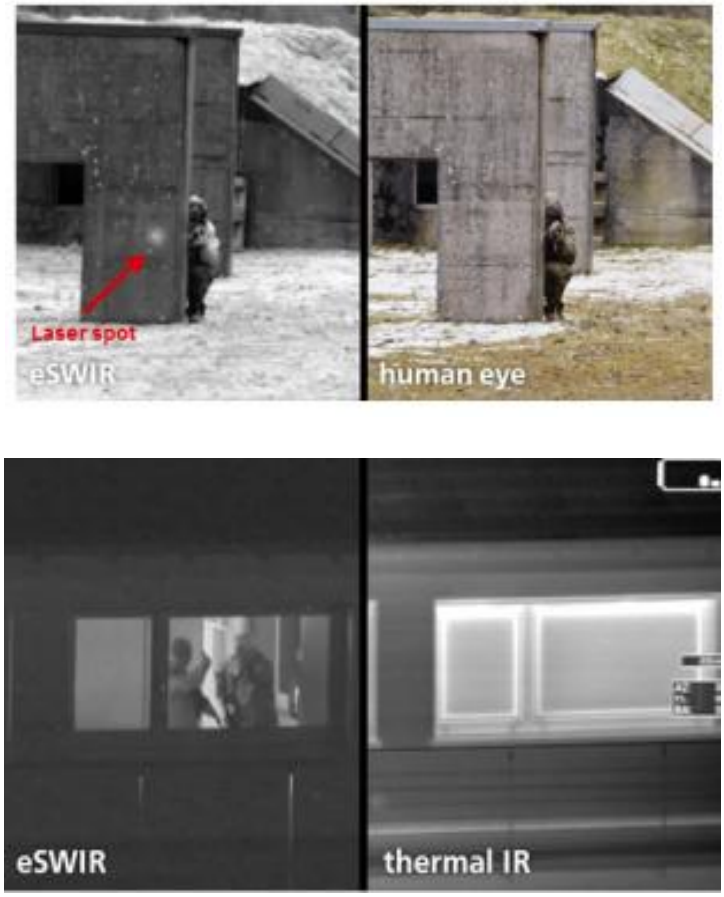

Figure 3.7 e-SWIR target designation performance [58]

The fabrication of e-SWIR technology is still under investigation due to technological drawbacks. Despite InGaAs being a mature technology and easy to manufacture, the performance of the devices is subject to debate. To address this, Razeghi et al. fabricated a type-II superlattice-based photodetector with a 12 μm pitch and 1280x1024 format for NASA. They presented the results of dark current modeling, showing a quantum efficiency of 62% at a wavelength of 1.9 μm. Additionally, they observed a change in the 100% cut-off wavelength depending on temperature, ranging from 150 K to 300 K, as illustrated in Figure 3.8.

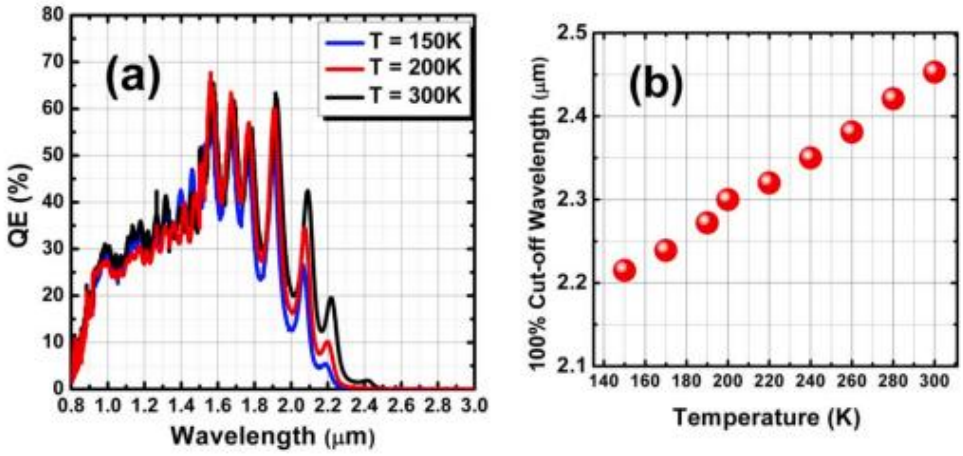

Figure 3.8. (a) Q.E. spectra of the text pixels in back-side illuminated device (b) The variation of the cut-off wavelength depended on temperature [59]

Additionally, Yong Ko et al. present the comparison of InGaAs and type-II superlattice based e-SWIR detectors. Their results indicate that, from a quantum efficiency perspective, InGaAs performs similarly to type-II superlattice detectors. However, the spectral range is broader in InGaAs-based detectors (see Figure 3.9). Another aspect requiring investigation in detector comparison is the dark current density, where InGaAs demonstrates superior results with $6.8x10^{-9}$ A/cm^2 under -0.1 V bias. Nevertheless, the peak detectivity is also higher for InGaAs based material. Also, the peak detectivity is also higher for InGaAs-based materials.

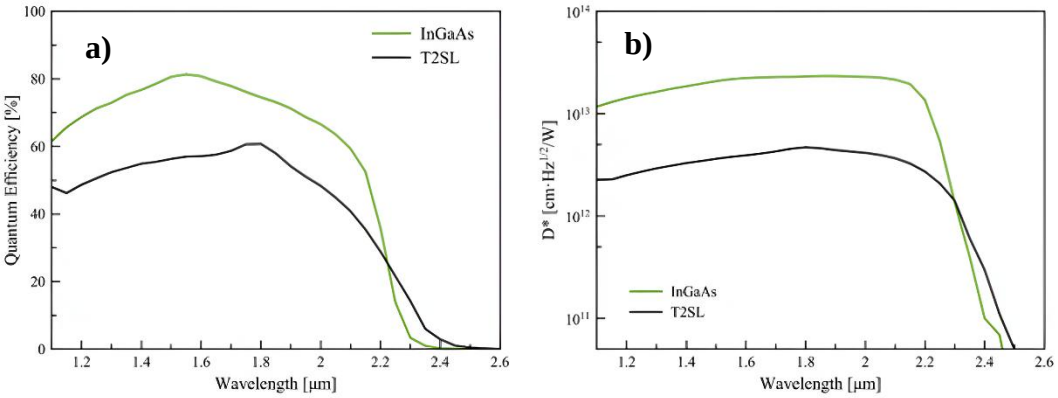

Figure 3.9. (a) Q.E. for InGaAs and superlattice based detectors at 200 K with -0.1 V (b) Specific detectivity of detectors [60]

According to Yong Ko et al., in the comparison of 10 μm pitch 1280x1024 format FPAs, InGaAs exhibits better detector performance. However, from the perspective of operability, the superlattice outperforms InGaAs due to its cross-hatch patterns.

The recent advancements indicate that InGaAs offers better performance in e-SWIR, primarily due to the absence of metamorphic epitaxial growth techniques. Therefore, in this thesis, the focus is solely on enhancing the efficiency of e-SWIR detectors through fabrication techniques. Until the development of epitaxial growth techniques, InGaAs remains the preferred choice for detectors, offering superior efficiency.

CHAPTER 4

FABRICATION OF EXTENDED SWIR PHOTODETECTOR

This chapter focuses on the fabrication process of mesa type e-SWIR PDs, starting with the design parameters of each layer. The properties of each layer are explained, along with the reasons behind them. The chapter provides clear information on each layer, including growth parameters, and ends with the layout mask design for the fabrication steps. After discussing passivation coating parameters, detailed tables are provided that list the coating specifications for different dielectric materials.

Subsequently, the chapter delves into the investigation of fabrication parameter results. To summarize, the fabrications that were investigated are listed as:

- Wet etch chemistry / stability / reproducibility,
- Dry etch chemistry / temperature / pressure,
- Metallization / annealing,
- Passivation chemistry / temperature / gas ratio,
- Anti-reflection gas ratio / refractive index,
- Silicon graded layer / metallization / hybridization / hybridization thickness,

The above comparison parameters are fabricated and investigated with mesa type manufactured devices. This chapter covers the process step application processes as well as the morphologic analysis of these techniques. The standard flow of the fabrication process, specifics of each phase, and a brief description of epilayer design will all be covered separately. The outcomes of the various ways that have been used and how they affect device performance will be discussed in the upcoming chapter.

4.1 Mesa Type Detector Fabrication

The fabrication of mesa-type photodetectors was carried out in a cleanroom environment using equipment available at NANOTAM, excluding the growth of epitaxial layer. Patterning of all structures was achieved using the mask aligner Suss MA6 system. Coatings were applied using the Sentech ICPCVD SI 500D system, while the dry etching process utilized the Samco ICP-RIE system. Metal coatings were deposited using the Leybold e-beam evaporator. The detector fabrication steps are visually represented in the schematic illustration provided in Figure 4.1.

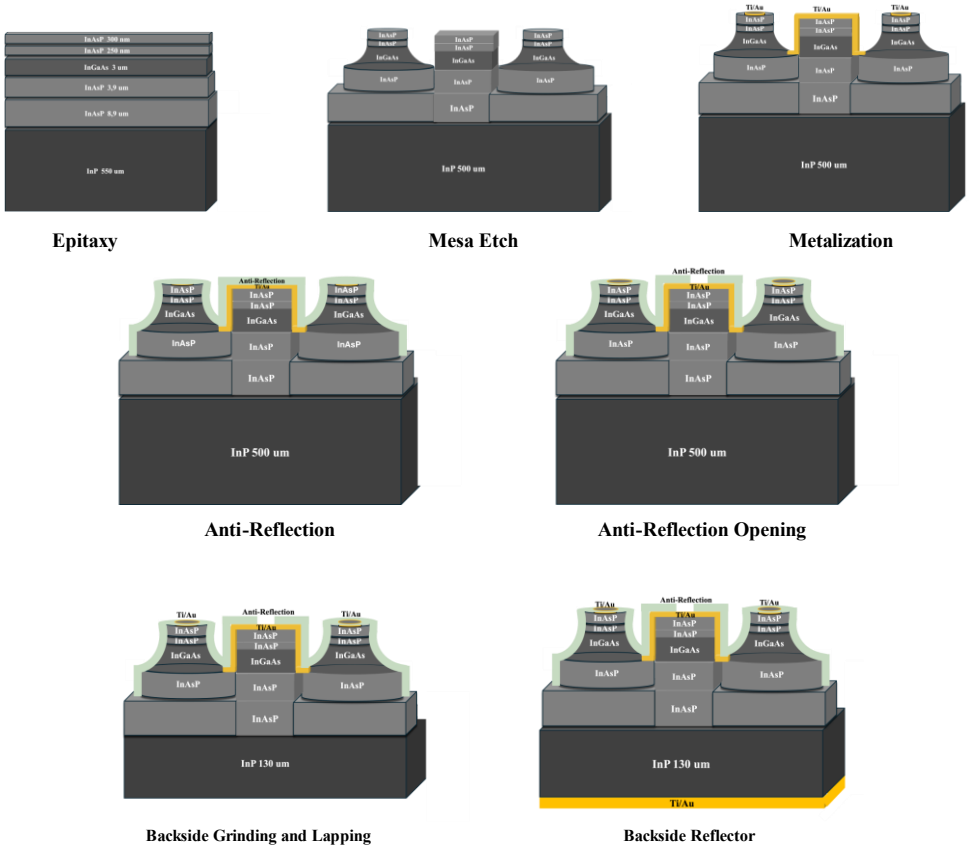

Figure 4.1. Schematic illustration of detector fabrication steps

4.1.1 Epi-Layer Design Properties

Conventional p-i-n epi-layers structure is based on absorber layer sandwiched in between p-type and n-type materials as illustrated in Figure 4.2. In e-SWIR PDs designed according to that and as an absorber layer $In_{0.8}Ga_{0.2}As$ placed and under its n-type InAsP and over its p-type InAsP is placed. Substrate is selected with traditional InP layer due to band gap energy. In mesa type production layers are doped with desired ratios in-situ of growth.

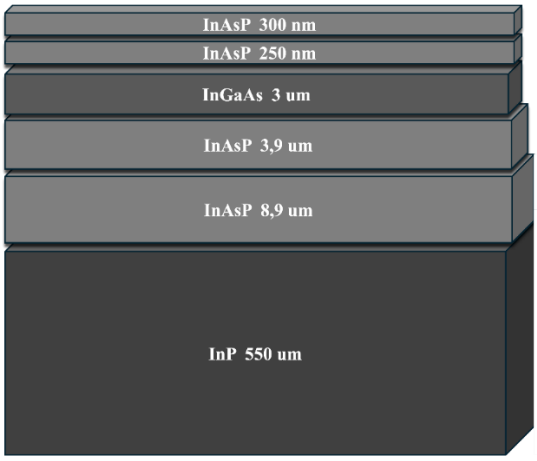

Figure 4.2. Design of e-SWIR epitaxy

The p-i-n design InAsP/InGaAs/InAsP heterostructure was grown on 3" InP substrate using AIXTRON 2800G4 MOCVD horizontal laminar flow reactor. As the precursors of III group elements, Trimethylgallium (TMGa), Trimethylindium (TMIn), Trimethylaluminum (TMAl) metalorganics were used. Group V elements (As and P) were delivered as arsine (AsH_3) and phosphine (PH_3). Silane (SiH_4) and dimethylzinc (DMZn) in-situ mixtures are the source of n-type and p-type dopant, respectively. Laytec's in-situ monitoring tool enabling reflectance measurement of surface quality, thickness, real surface temperature and wafer bowing. In the experiments the reactor pressure was kept at $5x10^3$ Pa and the growth temperature at the 600-650ºC level. 3" InP substrates with orientation (100) were applied. The grown InP-based epi-structures were characterized by several methods including microscopy (an optical microscope with Nomarsky contrast, transmission electron

microscope (TEM, S/TEM TITAN 80-300 by FEI), atomic force microscope (AFM, Bruker Dimension XR), X-Ray Diffraction (XRD, Panalytical X'Pert3 MRD), X-Ray topography (Rigaku XRT-100), High-Resolution Secondary Ion Mass Spectrometry (HR SIMS, Cameca 5). The n-type step-graded buffer layer was grown on InP substrate with a sufficient thickness to eliminate the effect of lattice mismatch besides dislocation formations followed by $InAs_{0.6}P_{0.4}$ layer n contact layer. The slightly n doped InGaAs absorber was designed to be 3 µm thick. The last two layers were composed of $InAs_{0.56}P_{0.44}$ on an absorber as both a barrier and a p^+ cap layer.

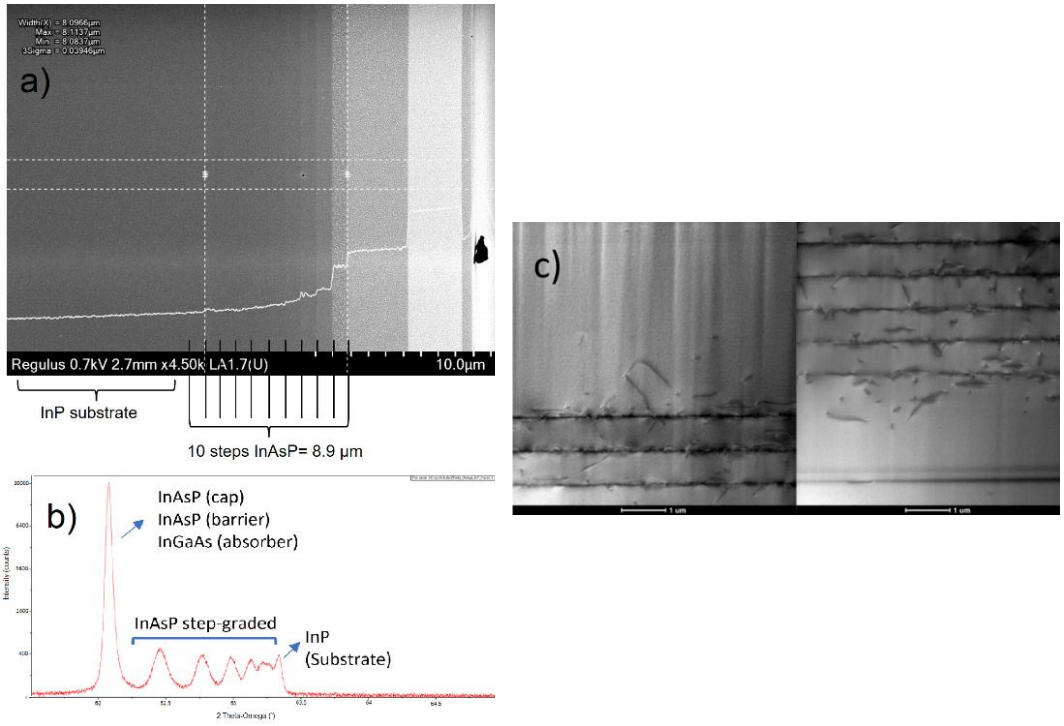

Figure 4.3. (a) SEM image of step-graded buffer layer (b) The XRD graph of e-SWIR epi-structure grown with MOCVD (c) TEM image of step-graded buffer layer

Figure 4.3 (a) shows the SEM image of the step-graded InAsP layer, the XRD peaks of epitaxial layers are shown also Figure 4.3 (b) with a narrow central peak demonstrating the lattice match condition for absorber, barrier and cap layers and step-graded bugger layer. The TEM images of step-graded buffer layer are also shown in Figure 4.3 (c) in two step images due to relatively thicker buffer layer to others. Additionally, the complete structure is provided in Table 4.1.

Table 4.1. Mesa epi-structure design

$InAs_{0.56}P_{0.44}$	**P-type Cap**	0.3 μm	Zn doped 3E18
$InAs_{0.56}P_{0.44}$	**Barrier**	0.25 μm	Si doped 1E16
$In_{0.8}Ga_{0.2}As$	**Absorber Layer**	3 μm	Si doped 1E16
$InAs_{0.6}P_{0.4}$	**N-type Constant**	3.9 μm	Si doped 2E18
$InAs_{0.6}P_{0.4}$	**Graded Virtual Subs.**	8.9 μm	Si doped 7E18
InP	**Substrate**		SI substrate

Despite the thick graded virtual layer and N-type layer, defects are unavoidable due to the high In mole fraction inherent in the material. This mole fraction leads to changes in the lattice constant, resulting in the presence of defects. An image showing the defects on the surface of the detectors is presented in Figure 4.4.

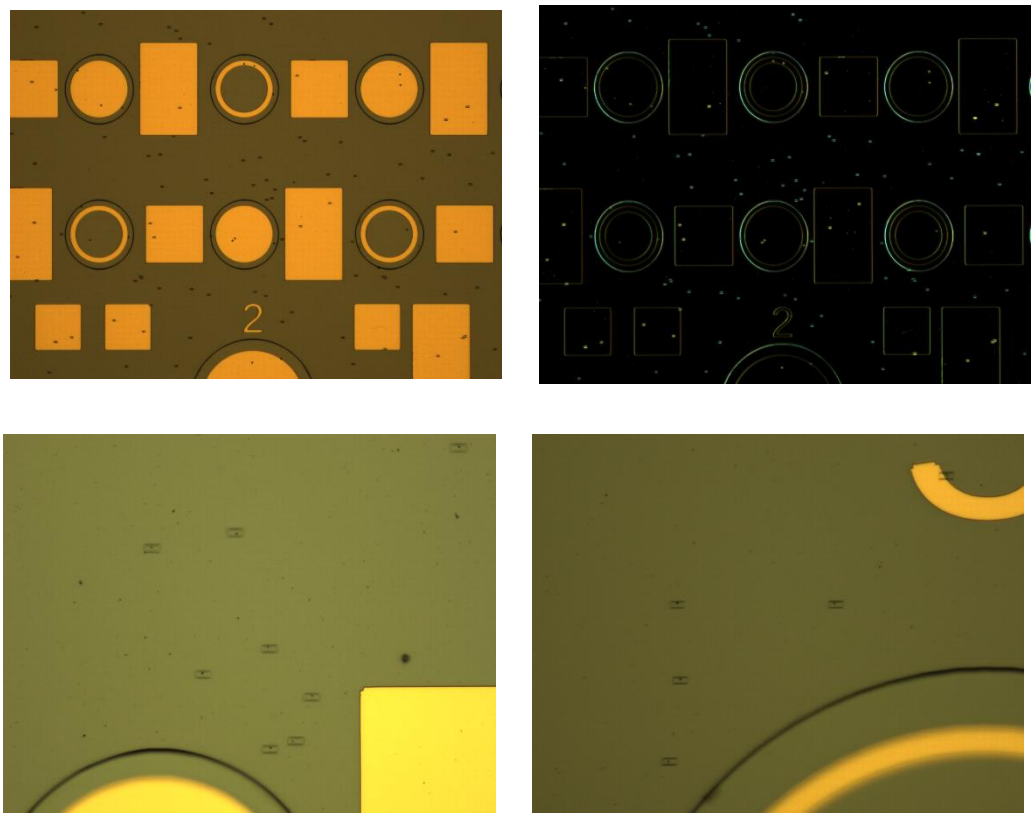

Figure 4.4 Frontside image of surface defects

4.1.2 N Contact Layer Design

The n contact layer, $InAs_{0.6}P_{0.4}$, is designed to serve as an n-type electrical contact layer, and thickness is determined to ensure the decreasing of dislocations effect in epitaxy. This layer is dedicated to exhibiting ohmic properties and is doped with Si atoms at a doping concentration of $2x10^{18}$ cm^{-3}. The thick thickness of n contact layer provides a wide processing window for both dry and wet etching. Additionally, higher thickness values are chosen to the reduce the mismatched-based problem. Therefore, thickness is determined in the final design to be 3.9 μm.

4.1.3 Absorber Layer $In_{0.8}Ga_{0.2}As$ Design

Increasing the thickness of absorber layer too many causes an increase in dark current related to both growth and lattice mismatch. Therefore, the thickness is determined as to be high achieve effective absorption to generate electron-hole pair while also ensuring it is not too thin to cause a transmission loss. Accordingly, absorber layer is grown to a thickness of 3 µm with unintentionally doping. The Electrochemical Capacitance Voltage (ECV) results are given in Figure 4.5 to demonstrate the doping concentrations for each layer.

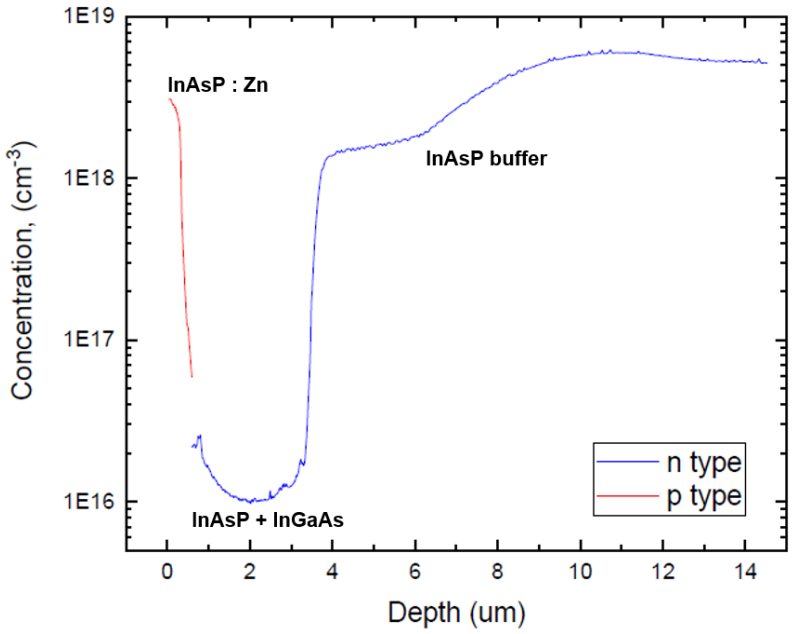

Figure 4.5. Stable and repeatable doping profile

4.1.4 Barrier Layer Design

There are two distinguished reasons to add a barrier layer, the first one is related to local dopant issues. Mesa type manufacturing requires doping during the growth conditions. Even though there is a change in dopant concentration or type in every layer transition, non-uniform dopant diffusion occurs. These types of local effects generate defect centers in the epitaxial layer.

Another purpose of the barrier layer is to serve as an electron confinement. Significantly, there is a large band gap offset exhibited between InAsP and InGaAs ($\Delta Ec=0.4\Delta Eg$), which leads to electron traps in the depleted region from p to absorber layer. Therefore, electron transitions, especially at room temperature conditions, occur with lower dark current reduction. Therefore, the barrier layer is added to prevent defects in the p-type layer and also reduce dark current.

4.1.5 P Contact Layer Design

The p contact layer, InAsP, is designed to serve as a p-type electrical contact layer, and InAsP selected for its ability to provide easy ohmic contact and reduce lattice mismatch. Typically, in SWIR photodiodes, the p contact layer is designed as InGaAs or InP, however, in our case, InP presents issues related to the ohmic situation due to higher band gap. InGaAs is not chosen due to the potential for reduction of absorption. Therefore, InAsP is designed to have a thickness of 0.3 μm and is doped with Zn atoms at a doping concentration of $3x10^{18}$ cm^{-3}.

4.1.6 Front Side Illuminated Photodiode Process Steps & Photomask Layout Desings

In this section of the thesis, the design and fabrication steps will be thoroughly explained and demonstrated. The investigation aims to evaluate the design parameters and potential options to enhance detector performance. Each fabrication step is tested under various conditions and with different chemicals to achieve better performance values.

The mesa fabrication is carried out with both front and backside illumination. In this regard, the front-illumination diodes are prepared for comparison with the backside-illuminated ones. Typically, backside-illuminated devices can detect wavelengths near 900 nm due to the InP layer. On the other hand, front-illuminated devices are

primarily geared towards extended-range detection. Additionally, comparing the performance of backside and front illumination provides valuable insights.

4.1.7 Mesa Layout Desing

The mesas are designed with active area sizes of 100, 200, 300, 500, and 1000 μm. The diode sizes are increased to accommodate the n-contact process steps, which may decrease the response due to reflections from metal surfaces. Lithography parameters are executed using Micro Chemicals AZ1505 photoresist with direct lithography. The corresponding lithography layout format is provided in Figure 4.6.

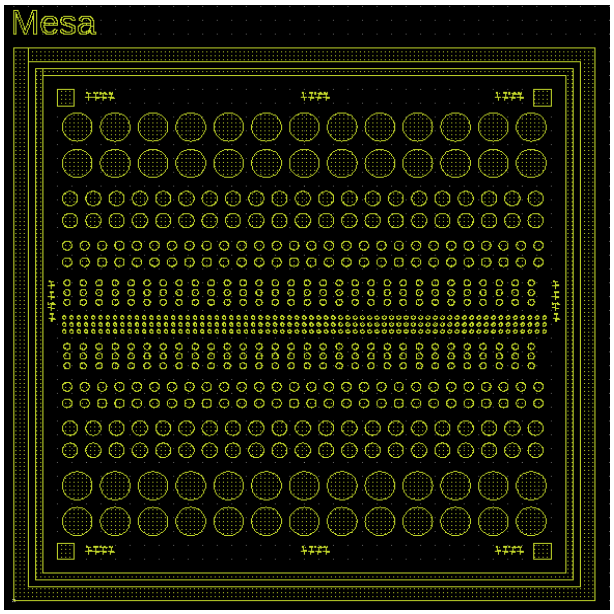

Figure 4.6. Mesa etches photolithography mask design

For etch test, various chemicals are employed, including H_3PO_4:HCl (3:1), $C_6H_8O_7$:DI Water (1:1), CrO_3:HCl:HF (1:1:0.5), HCl:HNO_3 (1:2). These chemicals are used to compare repeatability and depth to achieve better performance values. The thicknesses and chemical performances are investigated in the characterization chapter 5.1.

4.1.8 Ohmic Layout Design

The ohmic layout design incorporates the p and n contacts in the same coating chamber with one photolithography step. For the corresponding lithography, the selected photoresist is Micro Chemicals AZ5214, enhanced with an indirect lithography process. The n contact design is circular, with sizes of constant 20 μm for each different mesa area, while the p contact design is square-shaped and located on four sides of the n contact, with dimensions of 100x100 μm². The corresponding lithography layout format is provided in Figure 4.7.

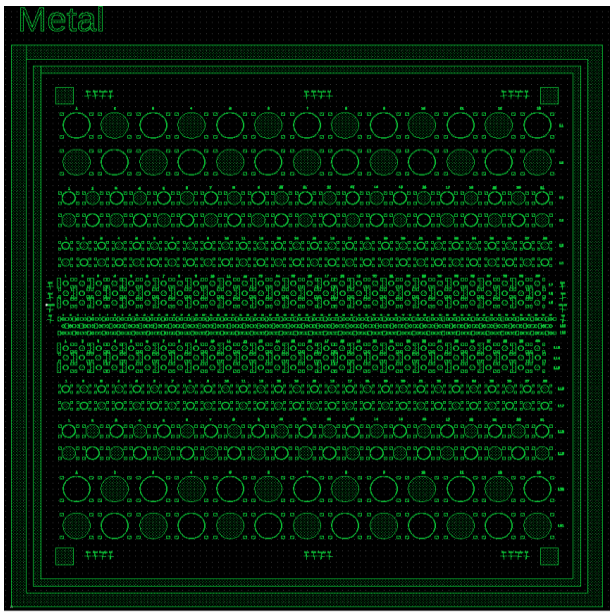

Figure 4.7. Ohmic metal photolithography mask design

Coating is carried out in an electron beam evaporation (e-beam) system using a Titanium/Gold (Ti/Au) combination. Various thicknesses are tested, such as 50/50 nm, 50/100 nm, and 25/150 nm, and annealed at various temperatures and times, such as 500°C/30 sec, 425°C/15 sec, and 350°C/5 sec. The performance of temperature/time and thicknesses are evaluated in the characterization chapter 5.2.

4.1.9 Passivation Parameters

The various SiN_x:H thin films deposition on photodiodes were carried out using NH_3, 5% SiH_4 diluted in He, and Ar gases. These various SiN_x:H recipes were deposited at constant ICP power, temperature and pressure after the samples cleaned with a diluted H_3PO_4:H_2O_2:DI Water and HCl:DI Water mixtures. The six different SiN_x:H recipes were deposited onto 4" crystallographic-oriented Silicon (Si) substrates (See Table 4.2). Subsequently, a spectroscopic ellipsometer was utilized to measure film thickness and refractive index, while the stress of various films was measured with a profilometer. To investigate the impact of different SiN_x:H characteristics on the PD dark current surface component, Fourier Transform Infrared (FTIR) spectroscopy was employed to analyze their bonding properties. Measurements were conducted in the range of 400 cm^{-1} to 4000 cm^{-1} with a resolution of 1 cm^{-1}.

Table 4.2. Deposition parameters of experimented SiN_x:H recipes

Film#	NH_3/SiH_4	T(ºC)	Refractive index (n)	Stress (MPa)	Thickness (nm)
1	1.3	75	1.911	1957	216
2	7	75	1.8	413	186
3	10	75	1.777	157	197
4	15	75	1.742	142	182
5	20	75	1.75	68	182
6	25	75	1.736	139	182

4.1.10 Passivation Opening Layout Design

Passivation open is designed to remove the dielectric layer over incoming pad metal region. The corresponding photolithography was carried out using Micro Chemicals AZ4533, enhanced with a direct lithography process. For etching process dry etch

method is used and the pad metal region was etched using Fluorine (F) based dry-etching chemistry in a Samco ICP-RIE system. The corresponding lithography layout format is provided in Figure 4.8.

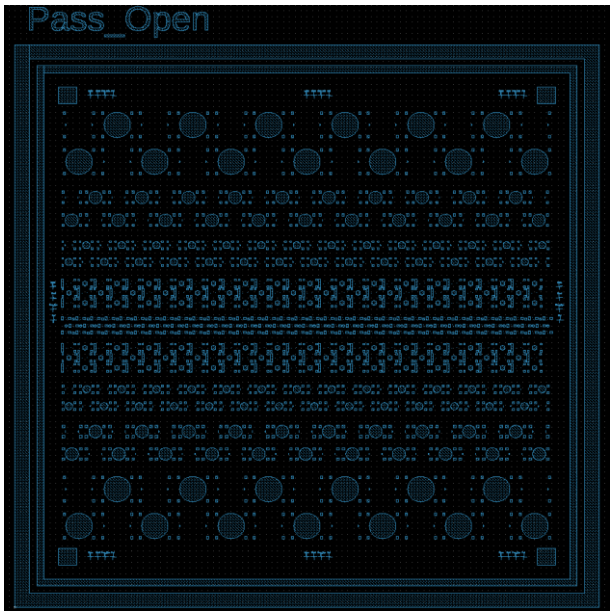

Figure 4.8. Passivation open photolithography mask design

Dry etching is performed using SF_6, Ar and O_2 gases without over etching and avoiding an increase in temperature. To achieve this, a precise etch time is employed with the loop etching technique. The etching period consists of 10 seconds of ICP, followed by 30 seconds of RF, and 40 seconds of cooling, repeated as necessary. The etch rate and chemical composition are evaluated in the characterization chapter 5.4.

4.1.11 Pad Metal Layout Design

The pad metal layout is designed to take contact from the p and n contacts without damaging the real contacts. For the corresponding lithography, the selected photoresist is Micro Chemicals AZ5214, enhanced with an indirect lithography process. The pad metal for n contact design is large “T”, with different sizes and located on two sides of n contact for each different mesa area, while the pad metal for p contact design is square shape and located on four sides of the n contact, with

dimensions of 90x90 μm². The corresponding lithography layout format is provided in Figure 4.9. Coating is carried out in an e-beam system using a Ti/Au combination.

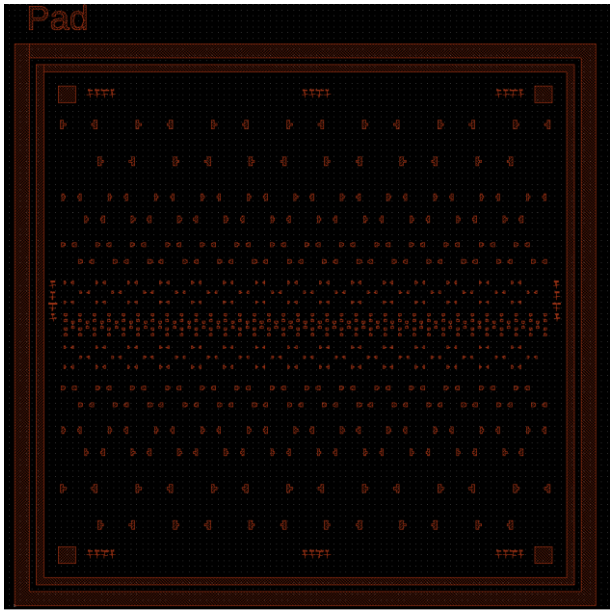

Figure 4.9. Ohmic metal photolithography mask design

Once all the frontside fabrication processes are completed, the detector is finalized. A fabricated image of the detectors is shown in Figure 4.10.

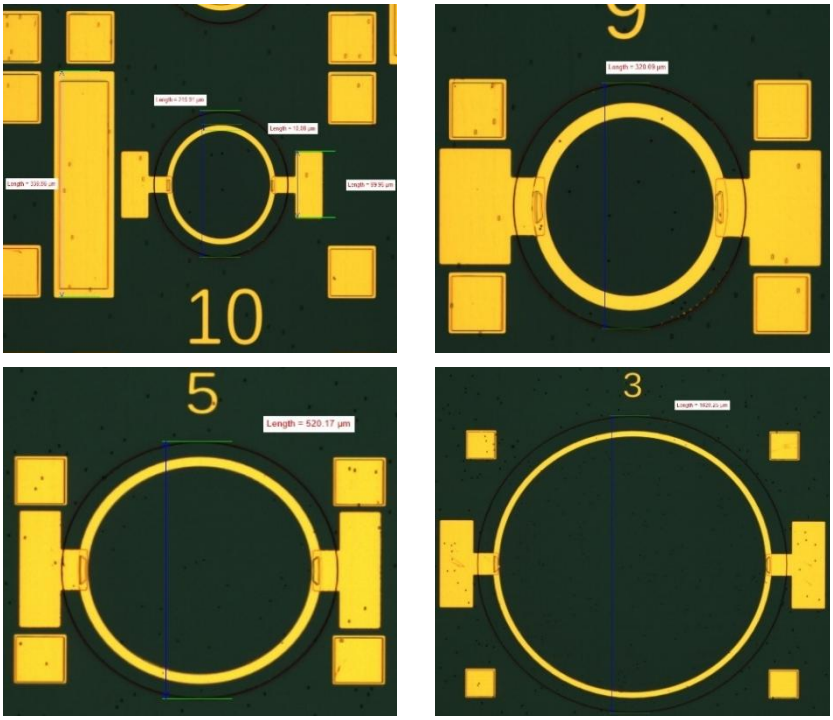

Figure 4.10 Photodetectors Fabricated with varying sizes

4.1.12 Backside Reflector Design

The primary objective of grinding and lapping is to reduce the thickness of the substrate. Additionally, with the aid of the backside reflector layer, it serves to reflect incoming photons to the absorber layer. Consequently, the detector substrate is thinned from 660 µm to 134 µm. The dressing recipe is provided in Table 4.3.

Table 4.3. Recipe for dressing for left (SD4000) and second rows for right (SD6000)

Dresser Board Thickness (µm)	Dressing Amount (µm)	Spindle RPM (rpm)	Chuck Table RPM (rpm)	Feed Rate (µm/s)	Air Cut (µm)
1980	150	2000	40	0.4	40
2070	50	2000	40	0.4	40

After the dressing process, the thinning process of the detector substrate begins. The recipe for thinning process is provided in Table 4.4.

Table 4.4. Thinning process recipe

Spindle (rpm)	Holder Spindle (rpm)	Air Cut (µm)	P1 Cut (µm)	P2 Cut (µm)	P3 Cut (µm)	Escape Cut	Spark Out
4000	300	50	0.07	0.07	0.07	4 µm, 0.5 µm/s 3000 rpm	100 rev. 300 rpm

Following the substrate thinning, the backside reflector process begins. The backside reflection layer is intended to reflect the light that is not absorbed back to the absorber layer. Therefore, the reflector layer must possess highly reflective properties. To achieve this, gold (Au) is selected, as it exhibits nearly 100% reflectance properties over wavelengths exceeding 500 nm. Before applying these metals to the backside of the detector, the front and active areas are protected with a special photoresist called AZ P4K-AP. This photoresist is made for protection only, leaving no residue behind because it does not react with light or bond with the semiconductor surface. After applying the photoresist, it is baked at 100°C for 4 minutes. Once the front side

is protected, the backside is coated using an e-beam system. To improve the adhesion of the 400 nm Au to the surface, a relatively thin 20 nm Ti layer is coated underneath the Au layer.

CHAPTER 5

CHARACTERIZATION

5.1 Mesa Etch Characterization

Traditional mesa fabrication begins with the etching process, which is characterized and optimized for each epitaxial structure. Etch depth and the choice of the chemicals are relatively have a significant impact on the device's performance. The chemicals used can interact with the epitaxial layer, altering its crystallographic structure or creating densely packed, unneutralized bonds along the etch sidewalls. These bonds can contribute to surface leakage and decrease performance. In this thesis, investigation of various etchants is conducted to minimize the effects of etched sidewalls and enhance the repeatability of process.

There are well-known chemicals for selective etching of III-V semiconductor materials, the performance of these chemicals with e-SWIR InAsP/InGaAs structure is tested. However, it's important to note that growth parameters and also etchants have varying effects on different epitaxies. Literature provides specific guidelines for the usage of these etchants and characterization methods [61],[62]. In this thesis, first investigate the H_3PO_4:HCl (3:1) chemicals for the InAsP/InGaAs materials.

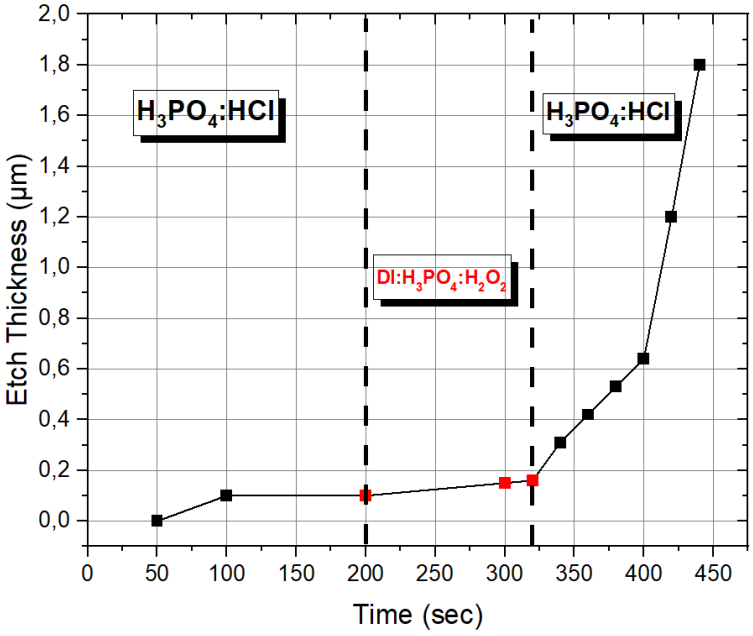

Figure 5.1. H_3PO_4:HCl etchant experiment and etching result

For this reason, the InAsP material was etched for 200 seconds with H_3PO_4:HCl (3:1) etchant and measure with profilometer system; however, as shown in Figure 5.1, the etchant was ineffective. Subsequently, a new etchant mixture, DI Water:H_3PO_4:H_2O_2 (3:1:1) was prepared and tested again with same sample for 100 seconds, but no noticeable changes were observed. However, upon reverting to the H_3PO_4:HCl (3:1) etchant again with same sample, the etching started with high rate.

For wet etching, the etchant must commence reliability and repeatability. However, in this case, the etchant exhibits contradictory behavior with epitaxy. This inconsistency could be related to the bond structure of the surface or its interaction with the atmosphere. To confirm this, different approaches are tested. Initially, the etchant DI Water:H_3PO_4:H_2O_2 (3:1:1) was to observe the results. If no changes occur within the same time frame, then the H_3PO_4:HCl (3:1) chemicals should have yielded similar results.

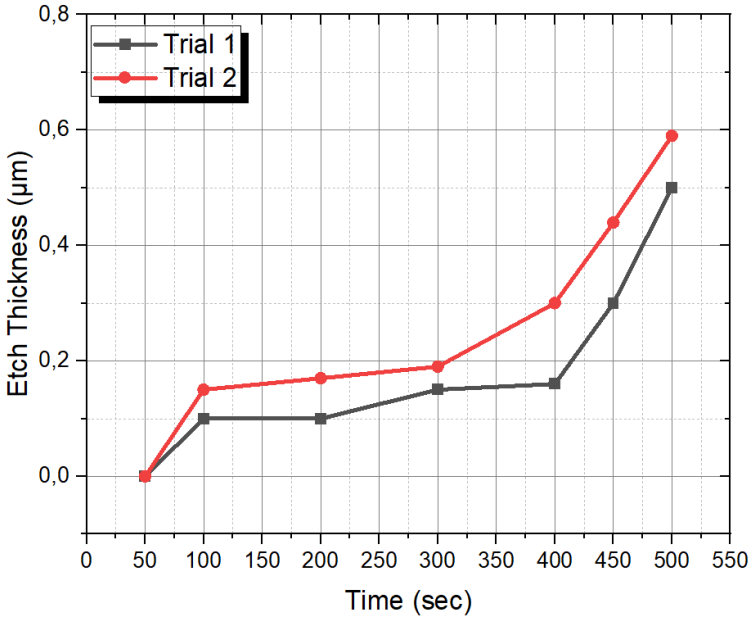

Figure 5.2. DI:H_3PO_4:H_2O_2 etchant trials

Figure 5.2 depicts two different trials using the DI Water:H_3PO_4:H_2O_2 (3:1:1) etchant. In the first trial, the mixture etched the same sample at variable rates, while in the second trial, the mixture showed no difference previous trial. Subsequently, it resumed with high-rate etching. These inconsistent etching rates are unacceptable and these changes with different trials showed the unreliable process parameters.

The other most used and tested etchant for InAs-based III-V semiconductor materials is the $C_6H_8O_7$:DI Water (1:1) chemical mixture. Two different trials were conducted with $C_6H_8O_7$:DI (1:1) chemicals using pieces diced from same wafer, and the results are inconsistent as demonstrated in Figure 5.3.

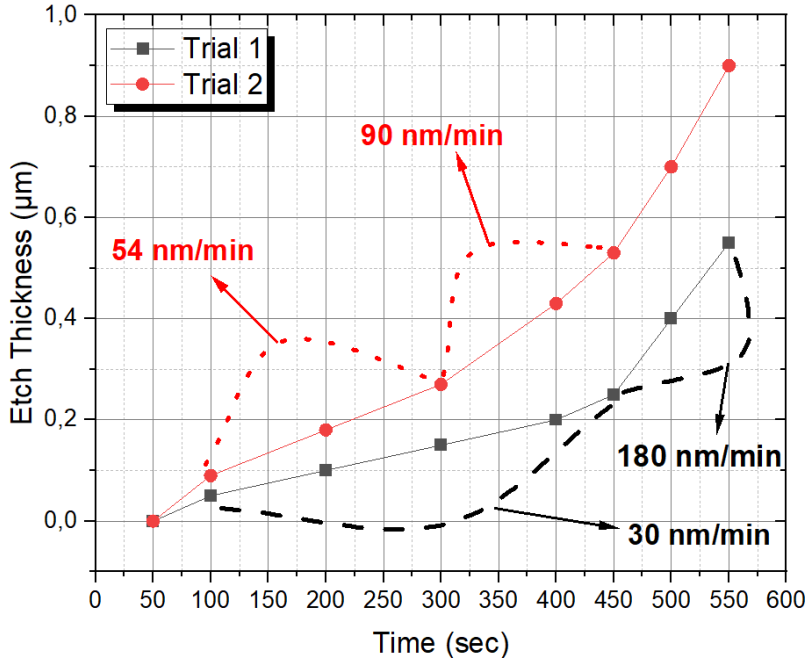

Figure 5.3. $C_6H_8O_7$:DI Water etchant trials

In the first trial, the etchant worked properly until reaching a thickness of 0.3 µm, after which the rate changed unexpectedly within the same epitaxy layer without any apparent reason. Conversely, in trial 2 the etch rate changed after 0.2 µm and then the exhibit increased rate within 150 seconds. Due to these unreliable results, the trials with the $C_6H_8O_7$:DI Water (1:1) chemicals were concluded.

The following etchants utilized for this experiment were the CrO_3:HCl:HF (1:1:0.5) and HCl:HNO_3 (1:2) chemical mixtures. However, the CrO_3:HCl:HF (1:1:0.5) etchant showed unsuitable interaction with InAsP epitaxy layer. After 400 seconds, the etched thickness was only 200 nm. Additionally, the HCl:HNO_3 (1:2) solution displayed an enormous etch rate and also striped the photoresist from the surface, even with different dilution mixtures as can be seen in Figure 5.4.

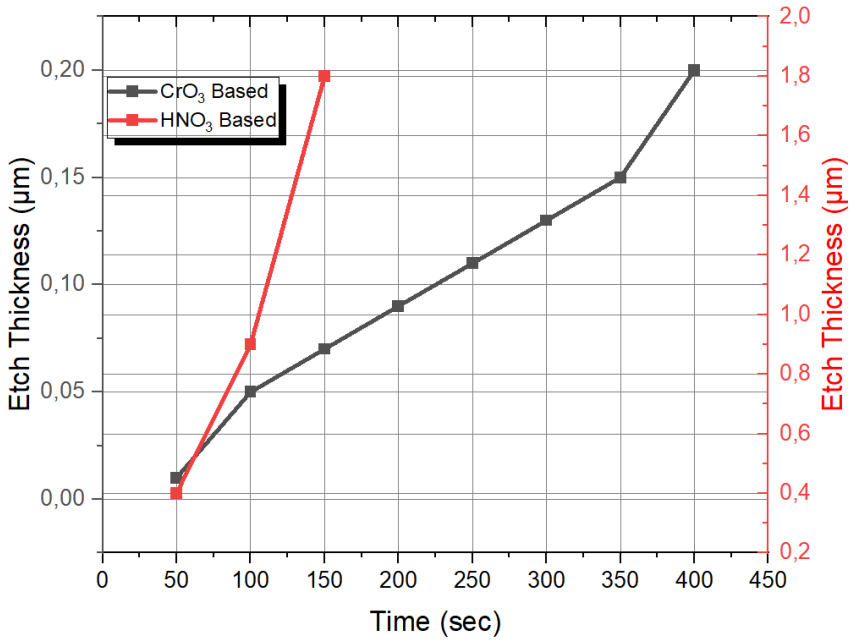

Figure 5.4. CrO_3 and HNO_3 based etchant solution trials

Inconsistency of wet etching even with different solutions has led to newer ways to create a mesa etching process. For that dry etching is tried to increase the reliability and repeatability of the process. BCl_3/Ar is selected for the dry etching process and the etching rate consistency is observed with deeper etching processes in Figure 5.5.

The result remained consistent in 325 second etching trials with the following parameters given in Table 5.1:

Table 5.1 ICP-RIE etching recipe for E-SWIR epitaxial structure

RF Power (W)	ICP Power (W)	Pressure (Pa)	BCl_3 Flow (sscm)	Ar Flow (sscm)	Time (sec)
160	260	0.18	16.2	15.5	325

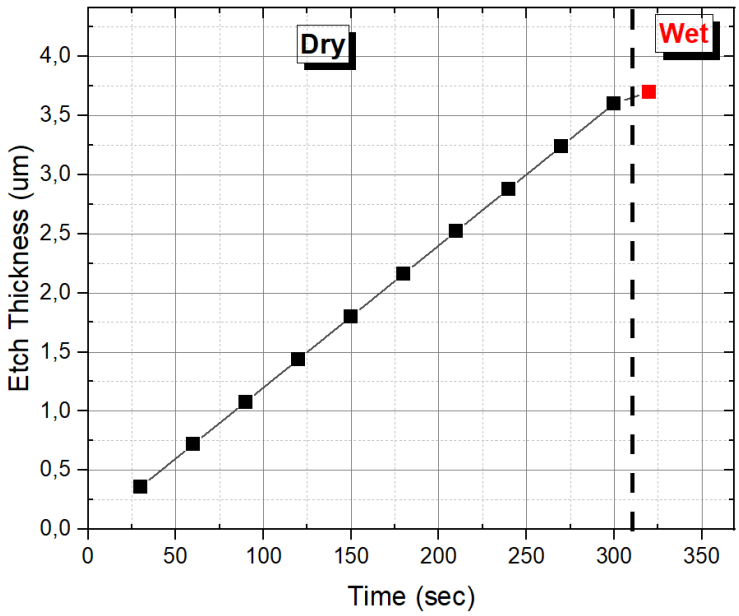

Figure 5.5. Dry and wet etching for mesa process

Even with high etching rates, the sidewalls remained relatively smooth and vertical. However, dry etching led to an increase in unnaturalized bonds at the sidewalls due to chemical etching properties. As a result, the samples were overetched within the frame of 15-20 seconds using the DI:H_3PO_4:HCl (3:1:1) solution, which is suitable chemical mixture for InGaAs epitaxy layer. Figure 5.5 demonstrated the etching time in seconds for both dry and wet processes.

Characterizing the etch depth also requires careful consideration. To evaluate its impact on dark current, diodes of the same size were tested with varying etch depths. To accomplish this, the dry etch time was varied to correspond with different etch depths across 3 samples, allowing for a detailed analysis of the etched area's impact on device performance. Following each adjustment, dark current measurements were carefully recorded to assess the relationship between etch depth and dark current behavior.

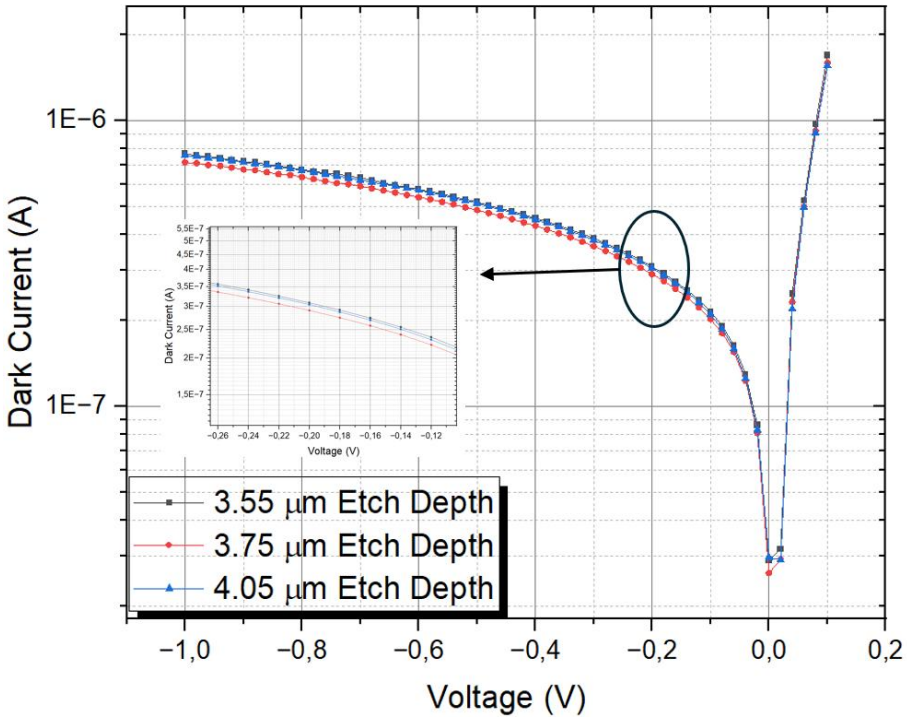

Figure 5.6. Impact of etch depth on dark current in same sized diodes

As shown in Figure 5.6, the etch depth does not impact the dark current, even with a 500 nm difference between two etch thicknesses.

Table 5.2 Comparison of dark current based on etch depth

Active Area (µm)	Etch Depth (µm)	Dark Current (A) (-100 mV)
300	3.55	2.02E-9
300	3.75	2.1E-9
300	4.05	2.15E-9

Although unneutralized etch side surfaces are typically expected to raise dark current, the experiment indicates that even with increased etch depths, the sidewalls have no measurable effect on dark current (Table 5.2). Currently, the etching process is functioning properly. However, if the fabrication continues as is, the dark current is expected to increase over time.

5.2 Ohmic Contact Fabrication

Ohmic contact is largely dependent on the surface work function and can pose significant challenges. However, creating ohmic contact from the InAsP surface is a relatively straightforward process because InAsP has a low work function. Conversely, to increase the forward current, annealing becomes necessary to achieve higher current levels. For this purpose, Ti/Au metals are chosen for ohmic contact in this process. During the annealing process, various temperatures are tested to prevent damage to the epitaxy layer. It's worth noting that temperature can create more defect centers within the epitaxy layer, hence the annealing is kept short to mitigate the risk. In this study, annealing trials were conducted at temperatures of 500 ^{o}C/30sec, 425 ^{o}C/15sec, 350 ^{o}C/5sec, 300 ^{o}C/5sec. According to that, the best outcome was obtained with the 350 ^{o}C/5sec trials as demonstrated in Figure 5.7.

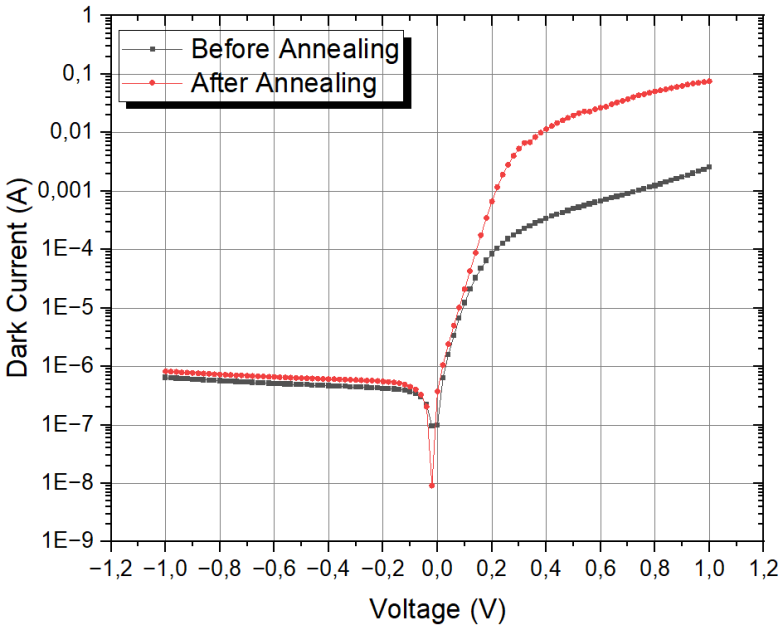

Figure 5.7. Annealing result after 350 ^{o}C/5sec trial

5.3 Passivation Fabrication

E-SWIR PDs commonly experience higher surface-related dark currents. Investigation passivation is crucial to overcome this issue. The aim of this study is to investigate the impact of H content in SiN_x:H thin film and elucidate its effects on the dark current of PDs. Therefore, various passivation recipes are prepared and applied to observe their effects on PDs. Subsequently, the impact of passivation is investigated in terms of stress, refractive index, and dangling bonds. The outcomes of each concept are tested through PD fabrication, and dark current modelling reveals the conclusion drawn from the results. To achieve this objective, experiments maintain constant temperature, power, pressure, and Ar flow.

In this thesis, varying passivation recipes by adjusting the NH_3/SiH_4 (R_H) ratio from 1.3 to 25 are explored, while maintaining constant conditions of 300 W ICP power, 75 ^oC temperature and 10 Pa pressure. Altering the gas ratio triggers chain reacting that impact stress and also refractive index. Generally, SiN_x:H films exhibit a refractive index within the range of 1.8 to 2.1 [63]. However, the ICPCVD system enables manipulation of this refractive index beyond the common range. Changes in refractive index and stress influence the optical, electrical and mechanical properties of thin films, due to atomic alignment [64].

Thin films produced by ICPCVD are often referred to as hydrogenated amorphous film, hence the acceptance of the expression $Si_xN_yH_z$. The electrical, optical and physical properties of films can be directly controlled by adjusting the content of x,y, and z in the film. In this study, the aim is to minimize surface leakage current. To achieve this, thin films with high dielectric constant (high-k) are sought to be produced as much as possible [65]. The amount of hydrogen and the type of bonds within the structure determine its electrical and optical properties. The change in the amount of Si-H bonds affects the electrical properties of the material. However, an increase in hydrogen content will make the film thermally unstable (as discussed in chapter 3.3 regarding the blistering effect). Conversely, N-H bonds within the film can be utilized to control optical absorption properties.

The variety of stoichiometry within R_H (given in Table 4.2) is correlated with the refractive index and stress as demonstrated in Figure 5.8.

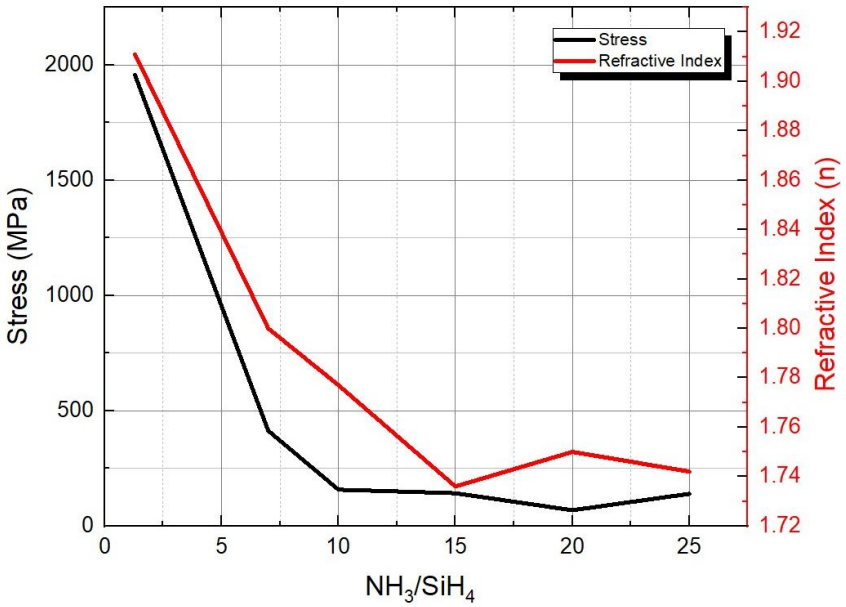

Figure 5.8. NH_3/SiH_4 dependent stress and refractive index

The amount of H depends on the function of temperature and in our case the change in R_H determines the content. As the R_H increases, it indicates an increase in the number of N-H bonds within the thin film that leads to drastic changes in the optical and mechanical properties of the film and results in a decrease in the refractive index and stress [66].

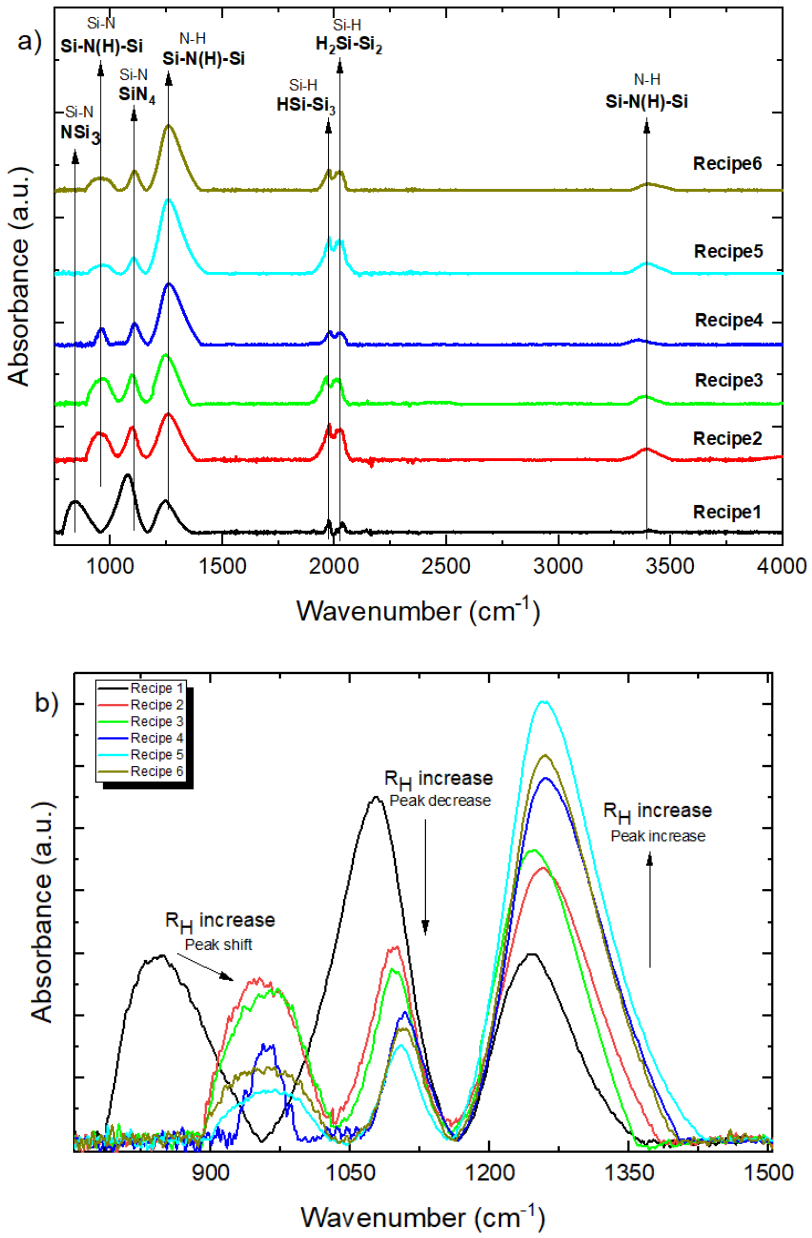

Figure 5.9. (a) The absorption spectra of SiN_x:H (b) The absorption spectra of SiN_x:H (from 750 to 1500 cm^{-1})

As seen in Figure 5.9 (a) absorption peaks caused by the vibrational modes of Si-N, N-H, and Si-H bonds were observed. On the other hand, the NSi_3 bond type is only observed in recipe 1, which has the lowest H content compared to other recipes. As the H content in the films increases, the NSi_3 bond disappears and is replaced by Si-N(H)-Si bonds. The emergence of Si-N(H)-Si bonds is attributed to Si-N type

vibrations, and the number of Si-N vibrations modes increases with the increased H content.

FTIR measurements provide information about vibration modes and absorption peaks related to these modes. However, to determine bond numbers, various calculation methods are necessary. Calculations of bond types within SiN_x:H involves utilizing formulas established by Lanford and Rand [67]:

$$N(X-Y) = \frac{1}{2.303xK(X-Y)} \int \sigma(v)dv \qquad (5.1)$$

Where $N(X-Y)$, provides the density of the $(X-Y)$ bonds and yields the peak value of absorption cross-section for the $K(X-Y)$ bonds. The expression $\int \sigma(v)dv$ represents the normalized absorption area for the band. The term $\sigma = \frac{2.303}{t} A$ defines the absorption coefficient where A is the absorbance and t are the film thickness. The absorbance spectra for each ratio are provided in Figure 5.9 (b) and Table 5.3 presents the vibration frequency, configuration, and bond counts for each bond type. In this study, K(Si-H) = $5.9x10^{16}$, K(N-H) = $8.2x10^{16}$, and K(Si-N) = $2.1x10^{16}$ were calculated.

Table 5.3. The bond types and calculated densities in SiN_x:H films.

	Si-N	Si - N	Si - N	N - H	Si - H	Si - H	N - H
1	889	-	53	25.3	1.36	1.52	0.73
2	-	8.50	33.7	54.6	9.66	8.49	10
3	-	6.84	26.6	61.8	6.66	7.22	56.9
4	-	2.06	14	105	2.64	2.85	3.91
5	-	2.00	97.8	127	9.29	10.4	9.58
6	-	3.59	13	107	4.1	5.61	6.36

*bond numbers x 10^{21} cm^{-3}

Owing to differences in R_H, the absorbance peaks are shifted towards to shorter wavelength and the amount of bonds (Si-N, N-H or Si-H) change. Also, change with

the R_H N-H bond numbers at 1175 cm^{-1} increase from 25.3x10^{21} cm^{-3} to 127x10^{21} cm^{-3}. However, to ensure the precise determination of bond sources, it is required to calculate the concentration of N and H atoms according to the calculation method of the atom concentration in SiN_x:H films, given as [68]:

$$N(Si) = \frac{[N(Si-N) + N(Si-H)]}{4} + \frac{N(Si-Si)}{2} \tag{5.2}$$

$$N(N) = \frac{[N(N-H) + N(Si-N)]}{3} \tag{5.3}$$

$$N(H) = [N(N-H) + N(Si-H)] \tag{5.4}$$

In this calculation, Si-Si and N-N bonds were not calculated due to their tendency to introduce defects in SiN_x:H films [69]. Furthermore, an increase in H content and a decrease in Si content are observed, as shown in Figure 5.10. Significantly, according to the given graphs, the H content reaches a saturation point at the corresponding value of the lowest Si content and decreases from that ratio. The decrease in H content, following recipe 5, hydrogen desorption becomes the dominant process within the thin film.

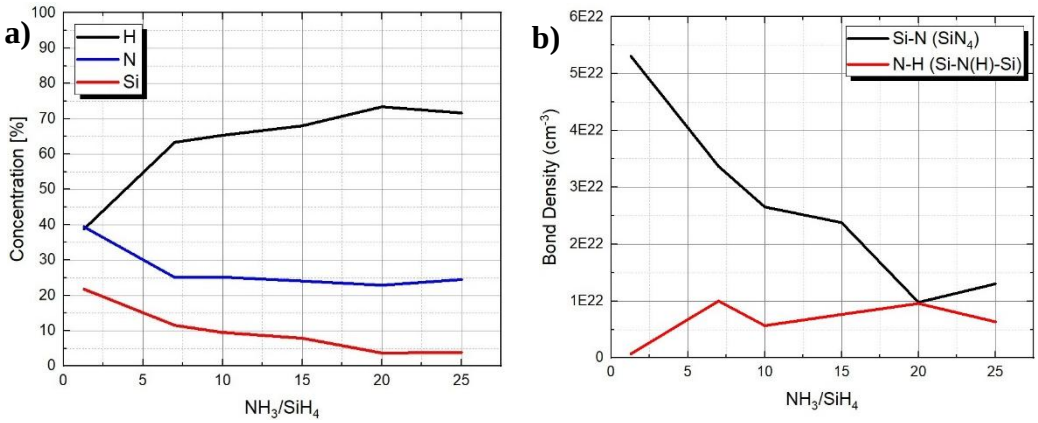

Figure 5.10. (a) Concentration of atoms in SiN_x:H depending on gas flow ratio, (b) Change in bond number due to gas flow change

Si inherently forms 4 bonds, and when the SiN_x:H film is formed, one of these bonds is left unoccupied, resulting in a dangling bond. Si dangling bonds are called K^- and K^+ trap centers [70], [71]. Dangling bonds tend to accumulate at the sidewalls of mesa-type PDs, forming a current channel along these walls. To effectively passivate the dangling bonds at the interface of InAsP/SiN_x:H, fixed charges must be considered, as they determine the electrical properties of the surface.

Coating conditions involve low temperature and high hydrogen concentration, H makes bonds with both Si and N atoms. Dangling bonds in Si atoms are commonly referred to as K^- center points, and if chamber has high H content these H atoms lie on the K^- center and passivate the Si atoms. This bonding acts as donor levels and has impact on reduction of surface related dark current. Figure 5.11 illustrates the passivation of Si atoms K^- center points with H atoms.

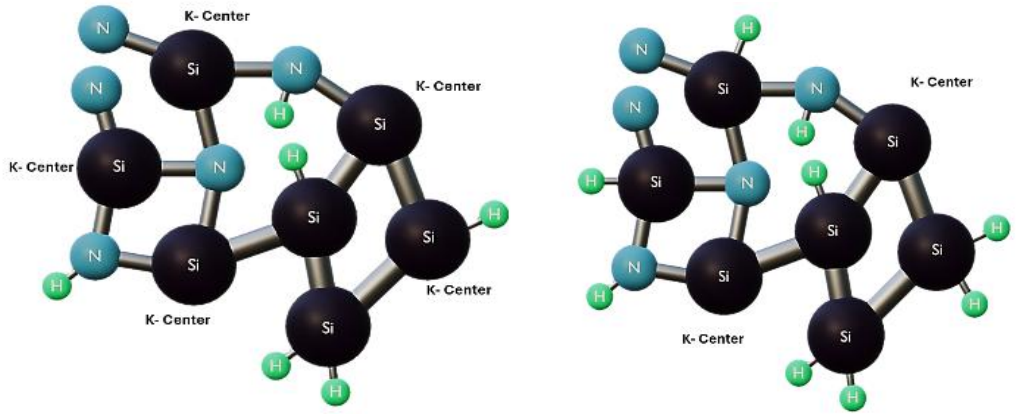

Figure 5.11. SiN_x:H film dangling bond passivation with H atoms from left to right

Although theoretically, passivation occurs and bond number increases with increased H content, it is essential to conduct dark current measurement to demonstrate the reduction of dark current depending on the bond numbers. For this reason, diodes with varying active diameters of 1000, 500, 300, 200 and 100 μm were fabricated on the same piece (detailed layout design is given in Chapter 4). The only difference between these diodes lies in the deposition parameters, and each passivation exhibits a significant difference in leakage current. As can be seen in Figure 5.12 the passivation with R_H 20 demonstrated the best performance outcomes compared to other passivation.

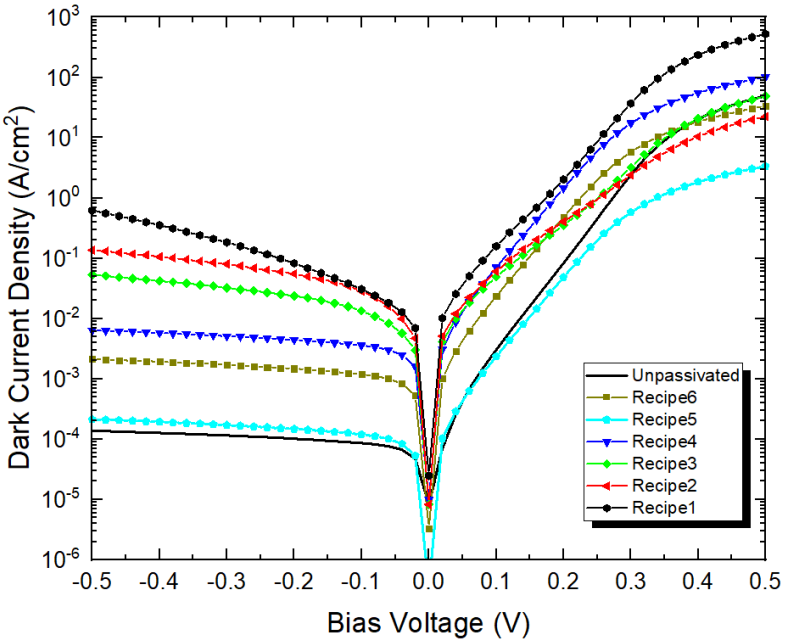

Figure 5.12. Dark current density results according to different passivation recipes

In the forward bias regime, all the recipes exhibit intricate forward characteristics, as can be seen between 0 V to 0.5 V bias voltage, while not observable in the reverse biases. This behavior in the forward bias regime is possibly caused by dangling bonds via K^- centers, which are dramatically suppressed in the passivated samples. Passivation recipes R_H 20 and 1.3 have a distinct impact on the forward bias, whereas the other recipes result in behavior similar to that of the un-passivated diode. To explain the mechanism behind the forward bias region, the relation of Si-H, N-H, and Si-N bonding configurations needs to be studied concerning the thermal effects they are exposed to. Relatively short times and small temperature differences can particularly affect Si-H bonds and alter the trap centers. These unpredictable effects contribute to the complexity of the forward bias regime [72].

The reduction of dark current density can result from several factors that impact the performance of PDs. To understand the sources of this reduction, dark current

modelling needs to be differentiated between various factors. The total dark current of the PDs depends on two components, bulk and surface.

$$I_{dark,total}(A) = A\ x\ J_{bulk}\left({}^{A}/_{cm^2}\right) + P\ x\ J_{surface}\left({}^{A}/_{cm}\right) \quad (5.5)$$

The details of the dark current mechanism are provided in Chapter 2. According to this:

$$I_{total} = I_{Diff} + I_{GR} + I_{BTB} + I_{TAT} + I_{Shunt} \quad (5.6)$$

Even though each component is differentiated from the other, they are all affected by the bias voltage (V) and temperature of the PDs. Depending on the changes starting point, we can distinguish the dominating region of each component.

Understanding the contribution of different dark current components to device performance across various temperatures, voltages, and size tests is crucial for elucidating the mechanisms underlying dark current, particularly ohmic conduction current (J_{ohm}) and generation-recombination current (J_{GR}). Analysis of the surface-bulk characteristics of un-passivated PDs indicates that the surface component outweighs the bulk component for all active area sizes under consistent conditions (refer to Figure 5.13). However, passivation with an optimized recipe (R_H 20) reveals a nearly equal distribution of surface and bulk components at around 120 μm. Beyond this size threshold, the emergence of bulk components in dark current indicates their dominance. This finding suggests that passivated devices with stabilized-charge-passivation exhibit mitigated surface effects.

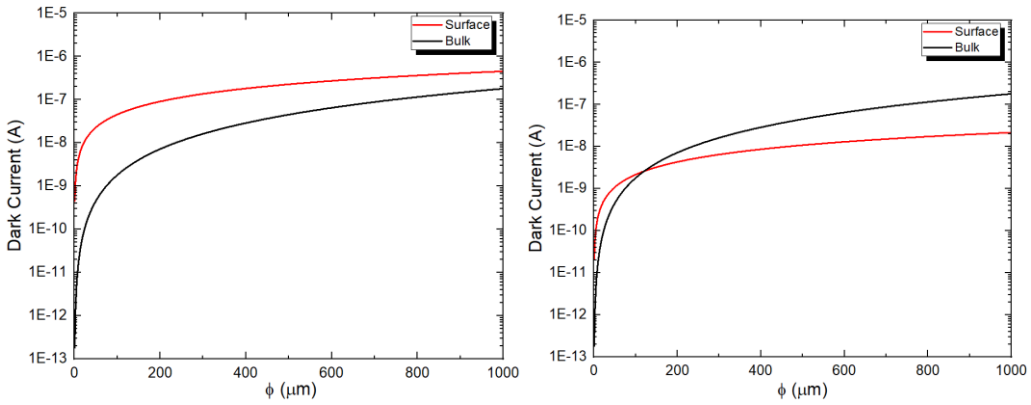

Figure 5.13. Left to right: before passivation and after optimized passivation recipe

Temperature-dependent I-V measurements were conducted on mesa-type diodes with a diameter Φ= 1000 μm, covering a temperature range from 288 K to 373 K with 5 K increments. It was observed that the tail in relatively higher bias voltages (>300 mV) begins to diminish as the temperature increases. This suggests that the diffusion current becomes increasingly dominant with rising temperature, as depicted in Figure 5.14.

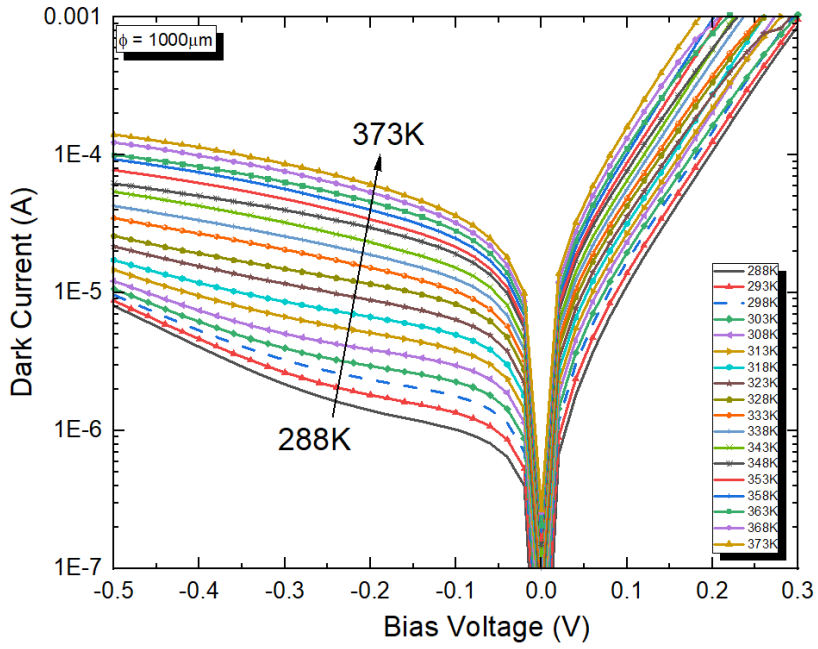

Figure 5.14. The temperature dependent I-V graph of diode with 1020 μm active area

The activation energy was also investigated using IV-T data collected at different temperatures and bias voltages (refer to Figure 5.15). Energy barriers hinder charge carriers from freely moving, thereby limiting their contribution to current flow, particularly in dark conditions. The results highlight the impact of tunneling current, particularly at higher temperatures.

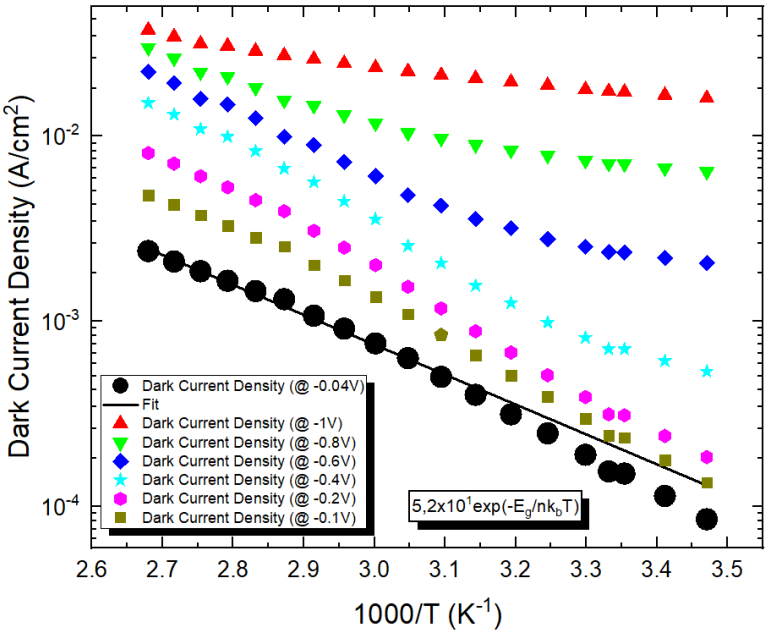

Figure 5.15. The calculated activation energy from IV-T data

Figure 5.16 (a) illustrates the variation of the R_0.A product as a function of temperature. The calculated activation energy is 42 meV, indicating that the G-R current predominantly influences the dark current, particularly at or near zero bias. In Figure 5.16 (b), the change in the effective G-R lifetime with temperature is presented, determined through dark current analysis at different temperatures. This suggests that the primary trap level is approximately 42 meV, closely located to the valence band. The carrier lifetime at 320 K can be estimated to be approximately 10 microseconds.

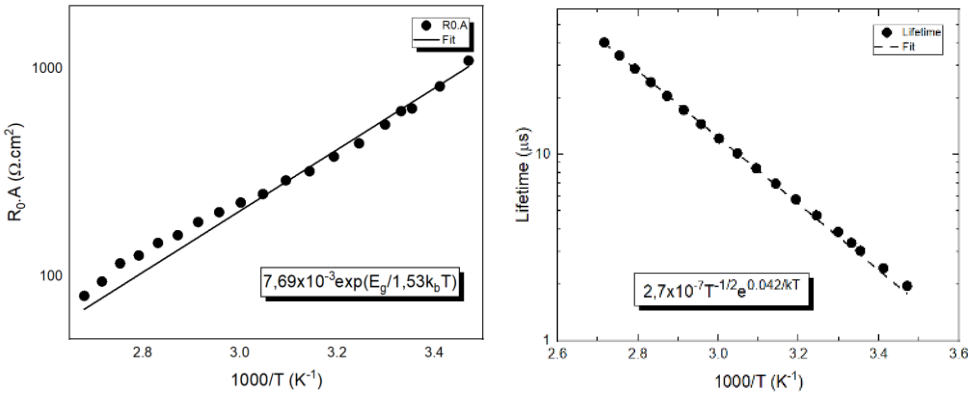

Figure 5.16. (a) the left graph the variation of R_0.A as a function of T, (b) the right graph Tau lifetime vs. 1000/T

The dark current I-V data at 300 K were utilized for modeling to analyze the components of dark current, including G-R, diffusion, TAT, BTB, and shunt. This sequential analysis is depicted in Figure 5.17.

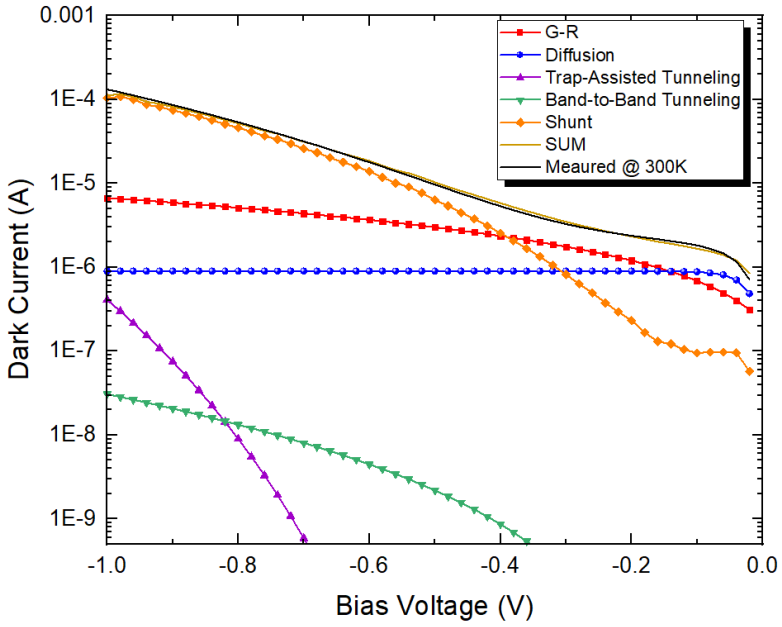

Figure 5.17. Total dark current mechanism results from optimized recipe R_H 20

The performance of a product-level photodiode is characterized by its reliability and stability throughout its operating lifetime. To assess stability in dark current, measurements were conducted at a constant voltage (-0.1 V) for nearly one hour.

Notably, no change in dark current was observed over time, as demonstrated in Figure 5.18. This result underscores the robustness of the product-level photodiode.

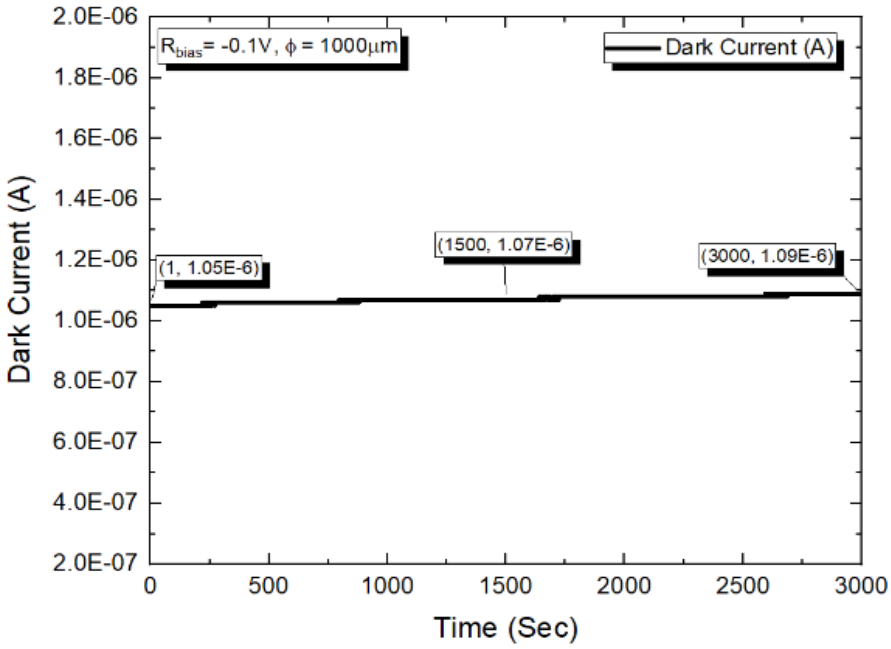

Figure 5.18. Time dependent lifetime (I-V) measurement

The recipes aimed to address dark current issues arising from surface-related issues in e-SWIR PD structures. Throughout the study, the effects of increasing H concentration on film stress, refractive index, and dangling bonds were thoroughly investigated. Consequently, variations in N-H bond density, as well as changes in stress and refractive index associated with ICPCVD SiN_x:H film, were observed depending on the H concentration. By analyzing the behavior of Si dangling bonds and K- trap centers, revealed their influence on dark current.

The correlation between the amount of K- trap centers and H content on dark current was observed, indicating that trap centers in the thin film are filled more with increased H, resulting in a reduction of Si dangling bonds and, consequently, a reduction in the influence of dangling bonds on dark current. Dark current measurements showed that recipe 5 (R_H=20) yielded the lowest stress and consequently the lowest fixed charge, resulting in the lowest dark current.

Furthermore, comparing un-passivated and passivated samples in terms of surface and bulk components of dark current revealed that the un-passivated sample exhibited surface dominance in all mesa diameters, while the passivated sample exhibited bulk dominance after a 200 μm active diameter size. Additionally, the activation energy analysis indicated that tunneling current was dominant at high temperatures, suggesting that trap levels in the epitaxial structure became activated with temperature, transforming into donor levels. Thus, all components of the dark current were examined, revealing the dominance of G-R current at low bias voltage regimes.

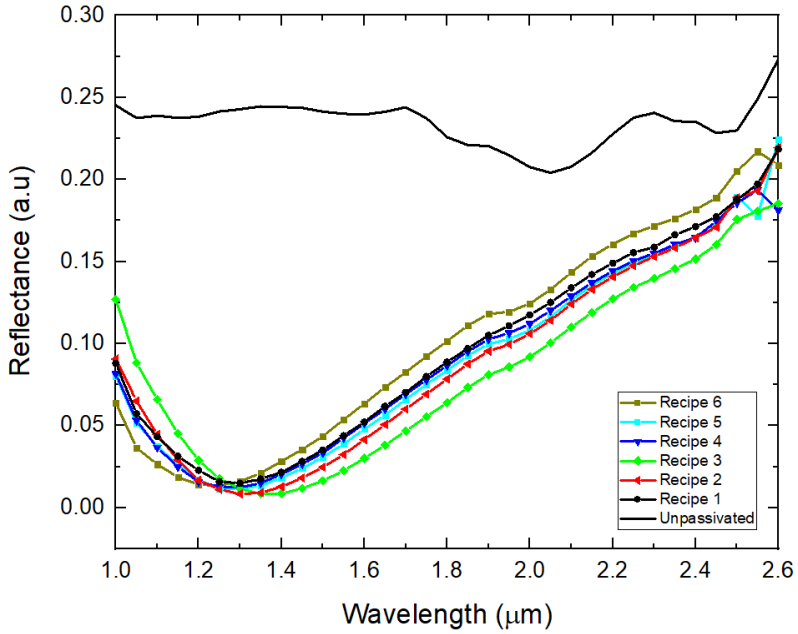

Figure 5.19. Reflectance values of a diode vary with different passivation ratios

Figure 5.19 depicts the reflectance spectrum between 1 um - 2.6 μm for six different SiN_x:H recipes, alongside an un-passivated surface. All the SiN_x:H recipes were sequentially deposited on the unprocessed surfaces of the same epitaxial design. Reflectance values improved for all SiN_x:H recipes compared to the un-passivated surface. The reflectance of the double layer structure can be calculated as:

$$R=\left|\frac{n_1 \cos\theta_i - n_2 \cos\theta_t}{n_1 \cos\theta_i + n_2 \cos\theta_t}\right|^2 \quad (5.7)$$

Where n_1 is the refractive index of the top layer of the epitaxy and n_2 is the refractive index of the passivation layer, θ_i angle of incident and θ_t angle of transmitted light. According to this formula, the calculated reflectance for InAsP/SiO_2 is nearly 50% higher compared to InAsP/SiN_x:H. The SiN_x:H films on InAsP layer with superior optical properties, making them more suitable for passivating PDs compared to SiO_2.

5.4 Passivation Opening Fabrication

Creating a dense and low-stress passivation layer on the surface requires more chemical etching than physical etching. Therefore, removing the passivation on the surface without damaging the active area is crucial. The dry etching method is applied using an ICP-RIE system, with the RF power kept low to minimize the attack on atoms on the surface. Additionally, increasing RF power reduces the protection of step coverage, so keeping this problem to a minimum involves accelerating particles with minimal velocity to start etching.

The passivation opening process is designed to create openings for metal contacts on the active surface area of the diodes. The importance of this process depends on the etching gases, conditions, and etching thickness related to the photoresist thickness. In this thesis, SF_6/O_2 and AR gases are selected as the etching gases. SF_6 is chosen over CHF_3-based chemical mixtures due to the need for more chemical etching. The O_2 flow is reduced to a minimum level to limit temperature increases on the surface and to prevent chemical transformation of the photoresist into carbon-based materials, which would require plasma cleaning and could have uncontrolled effects on the surface. Additionally, the Ar flow is kept as low as possible to minimize the reduction in thickness of the photoresist during the process time range.

5.5 Backside Reflector Fabrication

After the backside reflector coating, the responsivity measurements are conducted once again, and the results are compared with the previous (before thinning) measurements, and according to that the comparative results are discussed. The first factor to consider is the change in dark current. As shown in Figure 5.20, backside thinning significantly reduces dark current due to stress relaxation. Reducing the thickness of the InP substrate to 134 µm eliminates unwanted G-R current, resulting in a decrease in dark current, even though the reduction is not significant.

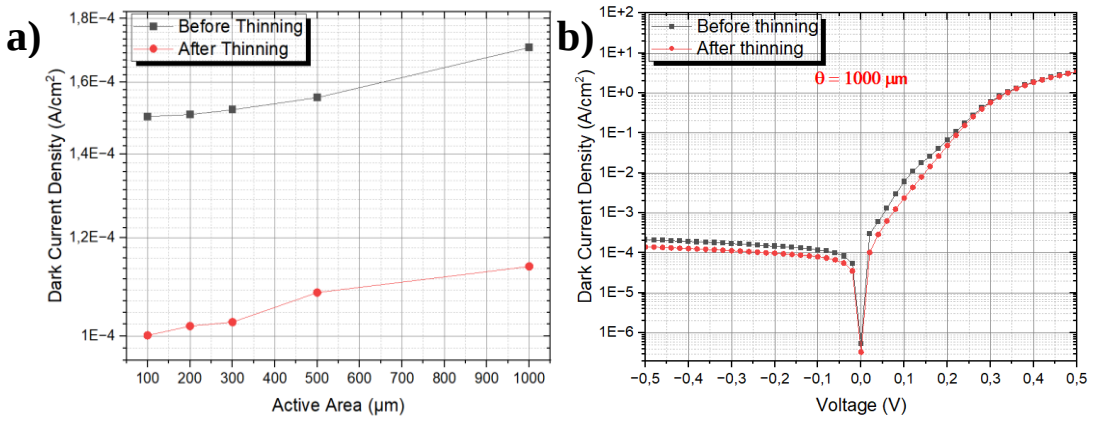

Figure 5.20. (a) Before and after thinning the substrate dark current density values at varying active area (b) Dark current density of 1000 µm photodiode

As shown in the Figure 5.20 (a), the dark current density values change with the size of the active area diodes. This variation is largely attributed to defects associated with the diode size. Ideally, the expected dark current values should remain constant, regardless of changes in the active diode area. However, the presence of defects can influence this variation. Changes in the active area may have differing effects on the dark current and its density, highlighting the impact of defect distribution.

The second important factor is the change in photocurrent. As shown in Table 5.4, the reflective surface at the back of the detector acts as a mirror, enhancing absorption. Before adding the backside reflector layer, smaller active area photodiodes exhibited higher responsivity compared to larger active area diodes.

This difference was primarily due to the impact of dark current, which affected larger diodes more significantly than smaller ones. However, after introducing the backside reflector layer, the responsivity of the larger diodes increased, matching the values observed in the smaller diodes.

Table 5.4. Comparative analysis of the impact of the backside reflector process on photodiode performance

Active Area (μm)	Responsivity (1800 nm)	
	Before Thinning	After Thinning
100	0,98	1,04
200	0,92	1,01
300	0,88	1,02
500	0,58	1,08
1000	0,49	0,99

This improvement is further complemented by enhanced uniformity, ensuring more consistent performance across the device. The increased uniformity plays a critical role in optimizing the overall efficiency and reliability of the system, particularly in applications where precise and stable operation is essential. As shown in Table 5.4 the responsivity of detectors with active areas of 1000 μm and 500 μm has improved to match the levels of detectors with smaller active areas of 100 μm, 200 μm, and 300 μm. These results demonstrate improved uniformity within the device, even in regions with higher defect concentrations. Additionally, the device's active area size is no longer a limiting factor for this type of detectors.

The final evaluation of the detector's performance focuses on responsivity as given in Figure 5.21 and external quantum efficiency (EQE) as shown in Figure 5.22. Measurements were conducted using 200 μm active area diodes at a wavelength of 1800 nm. The responsivity values indicate a noticeable improvement in quantum efficiency across all measured wavelengths. This observation, derived from the responsivity graph, clearly demonstrates that the detector operates significantly more

efficiently. The enhanced performance suggests that the detector's design and fabrication processes have successfully optimized its ability to convert incident light into an electrical signal, ensuring better functionality across a broad spectrum of wavelengths.

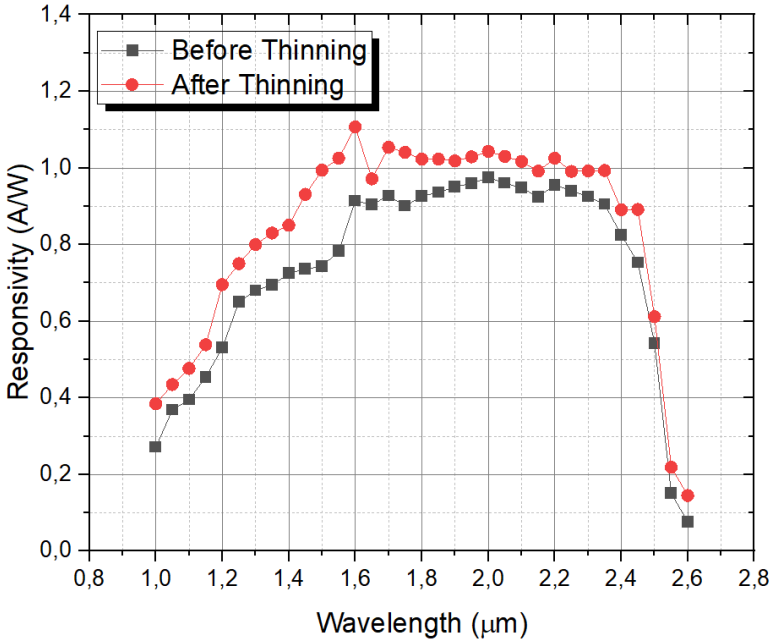

Figure 5.21 Spectral response of 200 µm active area detector

A significant increase in responsivity was observed between the 1 µm and 1.6 µm wavelength range after thinning the substrate in Figure 5.22. The peak responsivity occurred at 1.6 µm instead of the expected 2 µm, which is typically the designed peak for this detector type. This shift is attributed to the antireflection coating parameters, which were not optimized for a 2 µm peak but rather designed to span both the SWIR and e-SWIR ranges within the same detector structure. While SWIR detectors typically exhibit peak responsivity at 1.55 µm, this structure demonstrated its peak at 1.6 µm and also showed a measurable response beyond 1.8 µm something not commonly observed in standard SWIR detectors.

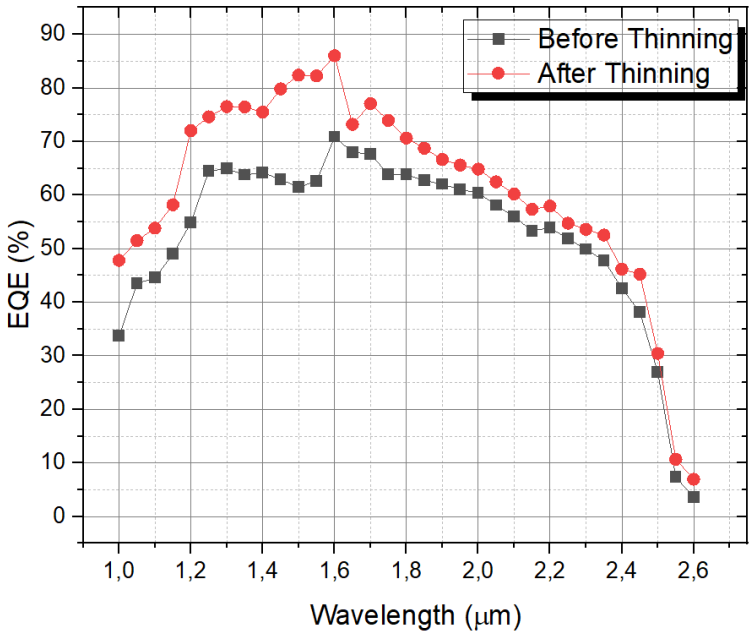

Figure 5.22 Calculated external quantum efficiency

In summary, the backside reflector mirror has a significant impact on detector performance, particularly when defects from the growth process are present. These defects cause scattering of photons before they reach the absorber layer, reducing the detector's efficiency. Thinning the substrate is crucial as it helps mitigate light damping in the InP layer. After the thinning process, the addition of the mirror layer resulted in a notable improvement in the detector's performance, enhancing its overall efficiency.

CHAPTER 6

CONCLUSION

This thesis provides comprehensive details on the design, fabrication, and innovative characterization of Extended SWIR photodiodes. It encompasses the epitaxial design and growth conditions, inlight the significance of each epi-layer, and details the fabrication of mesa-type detectors with layout design considerations. Additionally, it explores novel characterization features of the detector, including the diverse mesa etch process and its effects, ohmic contact properties, the importance of passivation layers through dark current modeling results, and finally, the influence of the backside reflector on the detector.

After evaluating various mesa etch trials over a single epitaxial design, a combination of dry and wet etching was determined to be the most suitable. Dry etching offers higher repeatability, but it often results in damage to the etched wall surfaces. To mitigate the impact of dangling bonds on the walls and minimize the increase in dark current, wet etching was chosen. This approach resulted in an optimal etching procedure for extended-range detectors.

The 6-different recipes with varying gas ratios with R_H were developed using ICPCVD method to reveal the effect of passivation layer on device performance in terms of dark current. The recipes aimed to treat the dark current arising from surface-related issues in e-SWIR PD structures. Throughout the study, the effects of increasing H concentration on film stress, refractive index, and dangling bonds have been thoroughly examined. Consequently, variations in the N-H bond density, as well as changes in stress and refractive index associated with ICPCVD SiN_x:H film, were observed depending on the H concentration. By analyzing the behavior of Si dangling bonds and K^- trap centers, we revealed their influence on dark current. The effect of correlation between the amount of K^- trap centers and H content on dark

current was observed such that the trap centers in the thin film are filled more through increased H, resulting in a reduction of Si dangling bonds. Thus, the influence of dangling bonds on dark current is reduced. Dark current measurements revealed that the recipe 5 (R_H=20) yielded the lowest stress and consequently the lowest fixed charge, resulting in the lowest dark current.

Accordingly, from the comparison of un-passivated and samples passivated with optimized recipe in terms of surface and bulk components of dark current, the un-passivated sample exhibited surface dominance in all mesa diameters while the passivated sample exhibited bulk dominance after a 200 μm active diameter size. Furthermore, activation energy showed the tunneling current was dominant at high temperatures. The primary reason for trap levels in the epitaxial structure became activated with temperature, turning into donor levels. Thus, all components of the dark current were examined and revealed dominance of G-R current at low bias voltage regimes.

One of the major challenges faced by extended-range detectors is the elevated levels of dark current, which hinder the attainment of higher responsivity values. To address this issue, a novel approach has been devised to enhance responsivity values without altering the dark current for extended SWIR detectors. This approach involves thinning the detector to approximately 130 nm, followed by the application of an Au reflective coating on the backside of the detector. The reflective material enhances the likelihood of absorption occurring in the absorption layer. Photons with higher wavelengths are readily absorbed by the absorption layer, whereas those with lower wavelengths have a lower probability of absorption. In this thesis, these photons that would otherwise be transmitted without absorption are collected from the backside of the detector, thereby resulting in an increased detector responsivity.

In conclusion, a high-performance Extended SWIR photodetector with various sizes (100, 200, 300, 500, and 1000 μm) has been successfully fabricated. The results and methodologies employed in this thesis are novel and have not been previously tested in the literature. From this perspective, the performance of market-available

detectors can be significantly enhanced, potentially leading to a rapid increase in demand for extended detectors.

Future research will prioritize improvements in growth conditions to achieve lower dark current levels. Additionally, efforts will be made to enhance fabrication techniques to further increase the absorption of backside-reflected photons.

REFERENCES

[1] J. Bastie, P. Blaser, A. Corrons, G. Dezsi, D. Förste, and C. Gentile, "THE MEASUREMENT OF ABSOLUTE LUMINOUS INTENSITY DISTRIBUTIONS".

[2] "Thermography," in *Van Nostrand's Scientific Encyclopedia*, Wiley, 2006. doi: 10.1002/0471743984.vse7010.pub2.

[3] C. Corsi, "New frontiers for infrared," *Opto-Electronics Review*, vol. 23, no. 1, Jan. 2015, doi: 10.1515/oere-2015-0015.

[4] R. W. M. Hoogeveen, R. J. van der A, and A. P. H. Goede, "Extended wavelength InGaAs infrared (1.0–2.4 μm) detector arrays on SCIAMACHY for space-based spectrometry of the Earth atmosphere," *Infrared Phys Technol*, vol. 42, no. 1, pp. 1–16, Feb. 2001, doi: 10.1016/S1350-4495(00)00061-X.

[5] A. Rogalski, J. Antoszewski, and L. Faraone, "Third-generation infrared photodetector arrays," *J Appl Phys*, vol. 105, no. 9, May 2009, doi: 10.1063/1.3099572.

[6] R. D. M. Scafutto, H. van der Werff, W. H. Bakker, F. van der Meer, and C. R. de Souza Filho, "An evaluation of airborne SWIR imaging spectrometers for CH4 mapping: Implications of band positioning, spectral sampling and noise," *International Journal of Applied Earth Observation and Geoinformation*, vol. 94, p. 102233, Feb. 2021, doi: 10.1016/j.jag.2020.102233.

[7] M. MacDougal, J. Geske, C. Wang, S. Liao, J. Getty, and A. Holmes, "Low dark current InGaAs detector arrays for night vision and astronomy," May 2009, p. 72983F. doi: 10.1117/12.820377.

[8] T. W. Case, “Notes on the Change of Resistance of Certain Substances in Light,” *Physical Review*, vol. 9, no. 4, pp. 305–310, Apr. 1917, doi: 10.1103/PhysRev.9.305.

[9] S. Adachi, *Physical Properties of III-V Semiconductor Compounds*. Wiley, 1992. doi: 10.1002/352760281X.

[10] A. K. Sood *et al.*, “Development of SiGe arrays for visible-near IR applications,” E. L. Dereniak, J. P. Hartke, P. D. LeVan, A. K. Sood, R. E. Longshore, and M. Razeghi, Eds., Aug. 2010, p. 77800F. doi: 10.1117/12.866362.

[11] H. A. E. Keitz, *Light Calculations and Measurements*. London: Macmillan Education UK, 1971. doi: 10.1007/978-1-349-00012-8.

[12] H. A. MacLeod and H. A. Macleod, *Thin-Film Optical Filters*. CRC Press, 2010. doi: 10.1201/9781420073034.

[13] J. A. Duffie (Deceased), W. A. Beckman, and N. Blair, *Solar Engineering of Thermal Processes, Photovoltaics and Wind*. Wiley, 2020. doi: 10.1002/9781119540328.

[14] B. Hussain, A. Ebong, and I. Ferguson, “Zinc oxide and silicon based heterojunction solar cell model,” in *2015 IEEE 42nd Photovoltaic Specialist Conference (PVSC)*, IEEE, Jun. 2015, pp. 1–4. doi: 10.1109/PVSC.2015.7356242.

[15] T.W.J., “Infrared system engineering,” *J Mol Struct*, vol. 9, no. 1–2, p. 214, Jul. 1971, doi: 10.1016/0022-2860(71)85028-7.

[16] M. Atef and H. Zimmermann, “Optoelectronic Circuits in Nanometer CMOS Technology,” 2016, pp. 217–240. doi: 10.1007/978-3-319-27338-9_10.

[17] W. Shockley and W. T. Read, “Statistics of the Recombinations of Holes and Electrons,” *Physical Review*, vol. 87, no. 5, pp. 835–842, Sep. 1952, doi: 10.1103/PhysRev.87.835.

[18] L. Wiley *et al.*, “Target discrimination in the extended SWIR (eSWIR) band (2-2.5μm) compared to Vis, NIR, and SWIR in degraded visual environments,” in *Infrared Imaging Systems: Design, Analysis, Modeling, and Testing XXXIII*, G. C. Holst and D. P. Haefner, Eds., SPIE, May 2022, p. 5. doi: 10.1117/12.2618566.

[19] R. G. Driggers, V. Hodgkin, and R. Vollmerhausen, “What good is SWIR? Passive day comparison of VIS, NIR, and SWIR,” G. C. Holst and K. A. Krapels, Eds., Jun. 2013, p. 87060L. doi: 10.1117/12.2016467.

[20] R. W. M. Hoogeveen, R. J. van der A, and A. P. H. Goede, “Extended wavelength InGaAs infrared (1.0–2.4 μm) detector arrays on SCIAMACHY for space-based spectrometry of the Earth atmosphere,” *Infrared Phys Technol*, vol. 42, no. 1, pp. 1–16, Feb. 2001, doi: 10.1016/S1350-4495(00)00061-X.

[21] Y.-G. Zhang, Y. Gu, K. Wang, A. Li, and C. Li, “Properties of gas source molecular beam epitaxy grown wavelength extended InGaAs photodetector structures on a linear graded InAlAs buffer,” *Semicond Sci Technol*, vol. 23, no. 12, p. 125029, Dec. 2008, doi: 10.1088/0268-1242/23/12/125029.

[22] R. Sur *et al.*, “TDLAS-based sensors for in situ measurement of syngas composition in a pressurized, oxygen-blown, entrained flow coal gasifier,” *Applied Physics B*, vol. 116, no. 1, pp. 33–42, Jul. 2014, doi: 10.1007/s00340-013-5644-6.

[23] M. P. Hansen and D. S. Malchow, “Overview of SWIR detectors, cameras, and applications,” V. P. Vavilov and D. D. Burleigh, Eds., Mar. 2008, p. 69390I. doi: 10.1117/12.777776.

[24] A. Dehzangi, A. Haddadi, R. Chevallier, Y. Zhang, and M. Razeghi, “nBn extended short-wavelength infrared focal plane array,” *Opt Lett*, vol. 43, no. 3, p. 591, Feb. 2018, doi: 10.1364/OL.43.000591.

[25] J. F. Klem, J. K. Kim, M. J. Cich, S. D. Hawkins, T. R. Fortune, and J. L. Rienstra, “Comparison of nBn and nBp mid-wave barrier infrared photodetectors,” M. Razeghi, R. Sudharsanan, and G. J. Brown, Eds., Jan. 2010, p. 76081P. doi: 10.1117/12.842772.

[26] J. Jiang *et al.*, “High-performance extended short-wavelength infrared PBn photodetectors based on InAs/GaSb/AlSb superlattices,” *Chinese Physics B*, vol. 32, no. 3, p. 038503, Mar. 2023, doi: 10.1088/1674-1056/acaa2e.

[27] P. Demeester, M. D’Hondt, I. Moerman, and P. Van Daele, “Influence of buffer layer and processing on the dark current of 2.5 μm-wavelength 2%-mismatched InGaAs photodetectors,” *IEE Proceedings - Optoelectronics*, vol. 144, no. 5, pp. 277–282, Oct. 1997, doi: 10.1049/ip-opt:19971412.

[28] *History of Semiconductor Engineering*. Berlin, Heidelberg: Springer Berlin Heidelberg, 2007. doi: 10.1007/978-3-540-34258-8.

[29] M. Arai *et al.*, “Uncooled (25–85°C) 10 Gbit/s operation of 1.3 [micro sign]m-range metamorphic Fabry-Perot laser on GaAs substrate,” *Electron Lett*, vol. 45, no. 7, p. 359, 2009, doi: 10.1049/el.2009.0263.

[30] K. Yuan, K. Radhakrishnan, H. Q. Zheng, Q. D. Zhuang, and G. I. Ing, “Characterization of linearly graded metamorphic InGaP buffer layers on GaAs using high-resolution X-ray diffraction,” *Thin Solid*

Films, vol. 391, no. 1, pp. 36–41, Jul. 2001, doi: 10.1016/S0040-6090(01)00966-X.

[31] A. Sacedón *et al.*, “Design of InGaAs linear graded buffer structures,” *Appl Phys Lett*, vol. 66, no. 24, pp. 3334–3336, Jun. 1995, doi: 10.1063/1.113748.

[32] M. K. Hudait, Y. Lin, and S. A. Ringel, “Strain relaxation properties of InAsyP1−y metamorphic materials grown on InP substrates,” *J Appl Phys*, vol. 105, no. 6, Mar. 2009, doi: 10.1063/1.3098232.

[33] J. Kirch *et al.*, “InAsyP1−y metamorphic buffer layers on InP substrates for mid-IR diode lasers,” *J Cryst Growth*, vol. 312, no. 8, pp. 1165–1169, Apr. 2010, doi: 10.1016/j.jcrysgro.2009.12.057.

[34] M. K. Hudait *et al.*, “Relaxed InAsP layers grown on step graded InAsP buffers by solid source MBE,” *MRS Proceedings*, vol. 722, p. K10.2, Feb. 2002, doi: 10.1557/PROC-722-K10.2.

[35] L. Ji *et al.*, “0.6-eV bandgap $In_{0.69}Ga_{0.31}As$ thermophotovoltaic devices with compositionally undulating step-graded $InAsyP_{1-y}$ buffers,” *Chinese Physics B*, vol. 22, no. 2, p. 026802, Feb. 2013, doi: 10.1088/1674-1056/22/2/026802.

[36] G. B. Galiev *et al.*, “Study of the influence of strained superlattices introduced into a metamorphic buffer on the electrophysical properties and the atomic structure of InAlAs/InGaAs MHEMT heterostructures,” *Semiconductors*, vol. 47, no. 4, pp. 532–537, Apr. 2013, doi: 10.1134/S1063782613040076.

[37] M. Haupt, K. Köhler, P. Ganser, S. Müller, and W. Rothemund, “Molecular beam epitaxy of heterostructures on metamorphic AlxGayIn1 − x − yAs buffer layers,” *J Cryst Growth*, vol. 175–176, pp. 1028–1032, May 1997, doi: 10.1016/S0022-0248(96)01013-5.

[38] R. Kumar *et al.*, “Comparison of different pathways in metamorphic graded buffers on GaAs substrate: Indium incorporation with surface roughness,” *Appl Surf Sci*, vol. 324, pp. 304–309, Jan. 2015, doi: 10.1016/j.apsusc.2014.10.155.

[39] S. Saha, D. T. Cassidy, and D. A. Thompson, “Comparison of different grading approaches in metamorphic buffers grown on a GaAs substrate,” *J Cryst Growth*, vol. 386, pp. 183–189, Jan. 2014, doi: 10.1016/j.jcrysgro.2013.10.015.

[40] M. Behet, K. van der Zanden, G. Borghs, and A. Behres, “Metamorphic InGaAs/InAlAs quantum well structures grown on GaAs substrates for high electron mobility transistor applications,” *Appl Phys Lett*, vol. 73, no. 19, pp. 2760–2762, Nov. 1998, doi: 10.1063/1.122582.

[41] M. Beaudoin *et al.*, “Band Offsets of $InAs_xP_{1-X}$/InP Strained Layer Quantum Wells Grown by Lp-Movpe Using TBAs,” *MRS Proceedings*, vol. 358, p. 1005, Feb. 1994, doi: 10.1557/PROC-358-1005.

[42] M. K. Hudait, Y. Lin, M. N. Palmisiano, C. Tivarus, J. P. Pelz, and S. A. Ringel, “Comparison of mixed anion, InAsyP1−y and mixed cation, InxAl1−xAs metamorphic buffers grown by molecular beam epitaxy on (100) InP substrates,” *J Appl Phys*, vol. 95, no. 8, pp. 3952–3960, Apr. 2004, doi: 10.1063/1.1667006.

[43] M. K. Hudait *et al.*, “High-quality InAsyP1−y step-graded buffer by molecular-beam epitaxy,” *Appl Phys Lett*, vol. 82, no. 19, pp. 3212–3214, May 2003, doi: 10.1063/1.1572476.

[44] S. Park, Y. Kim, P. D. Nguyen, J. Jeon, B. S. Chun, and S. J. Lee, “Toward Ga-Free Wavelength Extended 2.6 μm InAsP

Photodetectors with High Performance," *Adv Funct Mater*, vol. 34, no. 9, Feb. 2024, doi: 10.1002/adfm.202309897.

[45] C. B. Vartuli, J. D. MacKenzie, J. W. Lee, C. R. Abernathy, S. J. Pearton, and R. J. Shul, "Cl2/Ar and CH4/H2/Ar dry etching of III–V nitrides," *J Appl Phys*, vol. 80, no. 7, pp. 3705–3709, Oct. 1996, doi: 10.1063/1.363320.

[46] M. Heinbach, J. Kaindl, and G. Franz, "Lattice damage in III/V compound semiconductors caused by dry etching," *Appl Phys Lett*, vol. 67, no. 14, pp. 2034–2036, Oct. 1995, doi: 10.1063/1.115069.

[47] S. J. Pearton, C. R. Abernathy, P. W. Wisk, and F. Ren, "Ion implantation and dry etching characteristics of InGaAsP (λ=1.3 μm)," *J Appl Phys*, vol. 74, no. 3, pp. 1610–1615, Aug. 1993, doi: 10.1063/1.354809.

[48] H. Ohmi, J. Sato, Y. Shirasu, T. Hirano, H. Kakiuchi, and K. Yasutake, "Significant Improvement of Copper Dry Etching Property of a High-Pressure Hydrogen-Based Plasma by Nitrogen Gas Addition," *ACS Omega*, vol. 4, no. 2, pp. 4360–4366, Feb. 2019, doi: 10.1021/acsomega.8b03163.

[49] M. Tong, K. Nummila, A. A. Ketterson, I. Adesida, L. Aina, and M. Mattingly, "Selective Wet Etching Characteristics of Lattice-Matched InGaAs / InAlAs / InP," *J Electrochem Soc*, vol. 139, no. 10, pp. L91–L93, Oct. 1992, doi: 10.1149/1.2069023.

[50] K. Srinivasan, P. E. Barclay, O. Painter, J. Chen, and A. Y. Cho, "Fabrication of high-quality-factor photonic crystal microcavities in InAsP/InGaAsP membranes," *Journal of Vacuum Science & Technology B: Microelectronics and Nanometer Structures Processing, Measurement, and Phenomena*, vol. 22, no. 3, pp. 875–879, May 2004, doi: 10.1116/1.1701848.

[51] A. G. Aberle and R. Hezel, “Progress in Low-temperature Surface Passivation of Silicon Solar Cells using Remote-plasma Silicon Nitride,” *Progress in Photovoltaics: Research and Applications*, vol. 5, no. 1, pp. 29–50, Jan. 1997, doi: 10.1002/(SICI)1099-159X(199701/02)5:1<29::AID-PIP149>3.0.CO;2-M.

[52] E. Y. Chang, G. T. Cibuzar, and K. P. Pande, “Passivation of GaAs FET’s with PECVD silicon nitride films of different stress states,” *IEEE Trans Electron Devices*, vol. 35, no. 9, pp. 1412–1418, Sep. 1988, doi: 10.1109/16.2573.

[53] J. Yota, J. Hander, and A. A. Saleh, “A comparative study on inductively-coupled plasma high-density plasma, plasma-enhanced, and low pressure chemical vapor deposition silicon nitride films,” *Journal of Vacuum Science & Technology A: Vacuum, Surfaces, and Films*, vol. 18, no. 2, pp. 372–376, Mar. 2000, doi: 10.1116/1.582195.

[54] X. Huang *et al.*, “The 1/ f noise characteristics of In 0.83 Ga 0.17 As photodiodes with SiN x passivation films fabricated by two different techniques,” *Infrared Phys Technol*, vol. 67, pp. 596–599, Nov. 2014, doi: 10.1016/j.infrared.2014.10.008.

[55] M. Shi *et al.*, “Inductively coupled plasma chemical vapor deposition silicon nitride for passivation of In 0.83 Ga 0.17 As photodiodes,” *Infrared Phys Technol*, vol. 67, pp. 197–201, Nov. 2014, doi: 10.1016/j.infrared.2014.06.003.

[56] Y. Zhang *et al.*, “Effect of hydrogen content on dielectric strength of the silicon nitride film deposited by ICP-CVD*,” *Chinese Physics B*, vol. 30, no. 4, p. 048103, Apr. 2021, doi: 10.1088/1674-1056/abea82.

[57] Z. Yin and F. W. Smith, “Optical dielectric function and infrared absorption of hydrogenated amorphous silicon nitride films: Experimental results and effective-medium-approximation analysis,”

Phys Rev B, vol. 42, no. 6, pp. 3666–3675, Aug. 1990, doi: 10.1103/PhysRevB.42.3666.

[58] R. Breiter *et al.*, "Extended SWIR imaging for targeting and reconnaissance," in *Infrared Technology and Applications XLIV*, G. F. Fulop, C. M. Hanson, P. R. Norton, B. F. Andresen, and J. L. Miller, Eds., SPIE, May 2018, p. 2. doi: 10.1117/12.2304924.

[59] A. Dehzangi, A. Haddadi, R. Chevallier, Y. Zhang, and M. Razeghi, "Fabrication of 12 μ m pixel-pitch 1280 × 1024 extended short wavelength infrared focal plane array using heterojunction type-II superlattice-based photodetectors," *Semicond Sci Technol*, vol. 34, no. 3, p. 03LT01, Mar. 2019, doi: 10.1088/1361-6641/aaf770.

[60] S.-Y. Ko *et al.*, "Comparison of InGaAs and type-II superlattice based extended SWIR detectors," in *Infrared Technology and Applications XLVIII*, G. F. Fulop, M. Kimata, L. Zheng, B. F. Andresen, J. L. Miller, and Y.-H. Kim, Eds., SPIE, May 2022, p. 1. doi: 10.1117/12.2607834.

[61] "Index for Volume 1," in *Handbook of Advanced Electronic and Photonic Materials and Devices*, Elsevier, 2001, pp. 313–316. doi: 10.1016/B978-012513745-4/50087-1.

[62] A. R. Clawson, "Guide to references on III–V semiconductor chemical etching," *Materials Science and Engineering: R: Reports*, vol. 31, no. 1–6, pp. 1–438, Jan. 2001, doi: 10.1016/S0927-796X(00)00027-9.

[63] C.-C. Lee, H.-L. Chen, J.-C. Hsu, and C.-L. Tien, "Interference coatings based on synthesized silicon nitride," *Appl Opt*, vol. 38, no. 10, p. 2078, Apr. 1999, doi: 10.1364/AO.38.002078.

[64] H.-P. Ma *et al.*, "Measurements of Microstructural, Chemical, Optical, and Electrical Properties of Silicon-Oxygen-Nitrogen Films

Prepared by Plasma-Enhanced Atomic Layer Deposition," *Nanomaterials*, vol. 8, no. 12, p. 1008, Dec. 2018, doi: 10.3390/nano8121008.

[65] T. Li, S. Deng, X. Li, X. Shao, H. Tang, and H. Gong, "Responsivity performance of extended wavelength InGaAs shortwave infrared detector arrays," N. K. Dhar and A. K. Dutta, Eds., May 2014, p. 91000U. doi: 10.1117/12.2050242.

[66] S. Hasegawa, Y. Amano, T. Inokuma, and Y. Kurata, "Effects of active hydrogen on the stress relaxation of amorphous SiN *x* :H films," *J Appl Phys*, vol. 75, no. 3, pp. 1493–1500, Feb. 1994, doi: 10.1063/1.356384.

[67] W. A. Lanford and M. J. Rand, "The hydrogen content of plasma-deposited silicon nitride," *J Appl Phys*, vol. 49, no. 4, pp. 2473–2477, Apr. 1978, doi: 10.1063/1.325095.

[68] Z. Yin and F. W. Smith, "Optical dielectric function and infrared absorption of hydrogenated amorphous silicon nitride films: Experimental results and effective-medium-approximation analysis," *Phys Rev B*, vol. 42, no. 6, pp. 3666–3675, Aug. 1990, doi: 10.1103/PhysRevB.42.3666.

[69] D. Jousse and J. Kanicki, "Investigation of the light-induced effects in nitrogen-rich silicon nitride films," *Appl Phys Lett*, vol. 55, no. 11, pp. 1112–1114, Sep. 1989, doi: 10.1063/1.101673.

[70] V. A. Gritsenko, S. S. Nekrashevich, V. V. Vasilev, and A. V. Shaposhnikov, "Electronic structure of memory traps in silicon nitride," *Microelectron Eng*, vol. 86, no. 7–9, pp. 1866–1869, Jul. 2009, doi: 10.1016/j.mee.2009.03.093.

[71] W. L. Warren, J. Kanicki, J. Robertson, E. H. Poindexter, and P. J. McWhorter, "Electron paramagnetic resonance investigation of

charge trapping centers in amorphous silicon nitride films," *J Appl Phys*, vol. 74, no. 6, pp. 4034–4046, Sep. 1993, doi: 10.1063/1.355315.

[72] B. Macco *et al.*, "Correlating the silicon surface passivation to the nanostructure of low-temperature a-Si:H after rapid thermal annealing," *J Appl Phys*, vol. 122, no. 3, Jul. 2017, doi: 10.1063/1.4994795.